Uncertainty management in parameter identification

Liqi Sui

Par **Liqi SUI**

Uncertainty management in parameter identification

Thèse présentée
pour l'obtention du grade
de Docteur de l'UTC

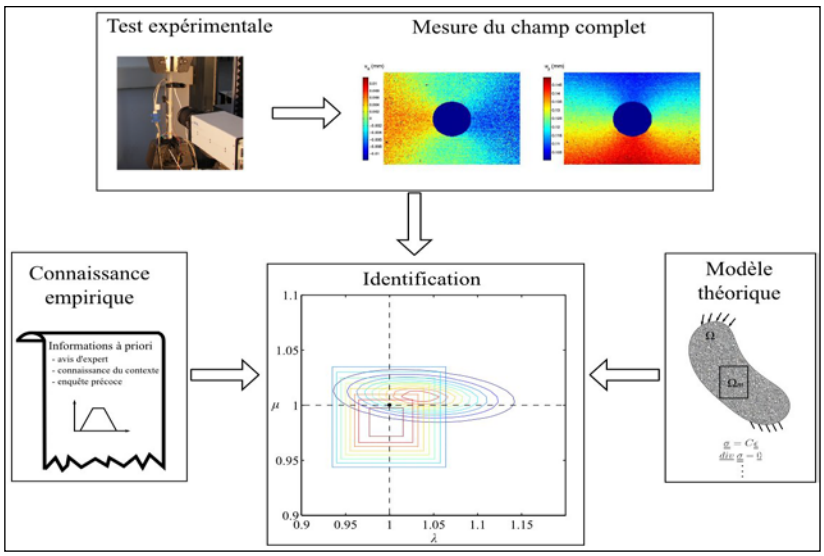

Soutenue le 23 janvier 2017
Spécialité : Advanced Mechanics

D2330

By Liqi SUI

Uncertainty management in parameter identification

Thesis presented

to obtain the degree of Doctor of the UTC

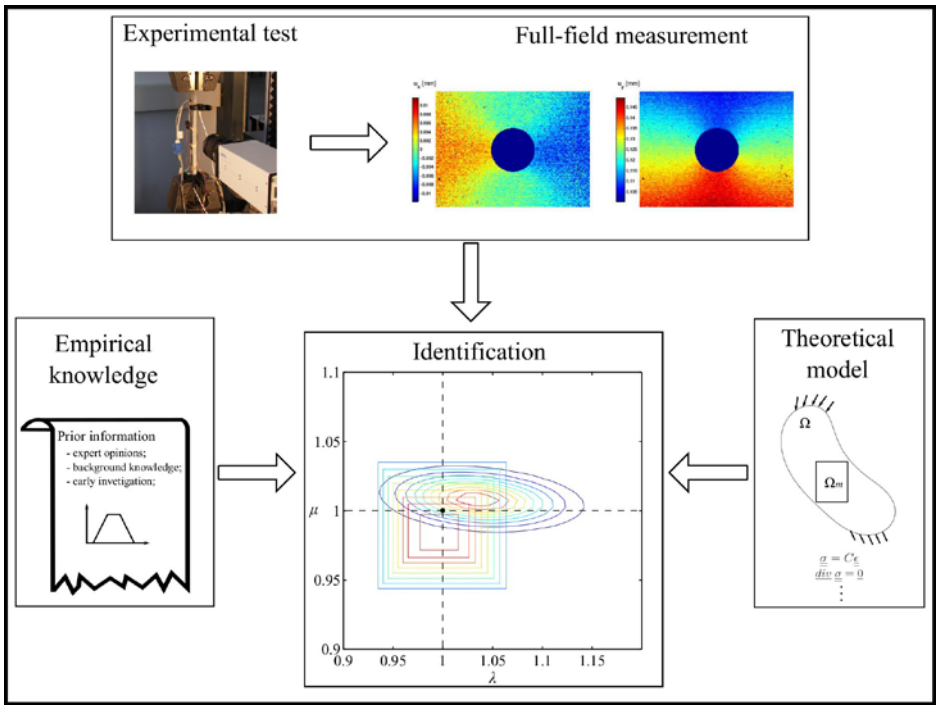

Defended on : 23 January 2017

Speciality : Advanced Mechanics

Uncertainty management in parameter identification

Liqi SUI

Defended on : 23 January 2017

Speciality: Advanced Mechanics

The members of the jury :

Reviewers :

Guillaume PUEL	David MERCIER
Professeur des Universités	Maitre de Conférences (HDR)
CentraleSupélec	Université d'Artois
	IUT de Béthune

Examiners :

Thierry TISON	Sébastien DESTERCKE
Professeur des Universités	Chargé de Recherche au CNRS
Université de Valenciennes	Université de Technologie
	de Compiègne

Supervisors :

Thierry DENŒUX	Pierre FEISSEL
Professeur des Universités	Maitre de Conférences (HDR)
Université de Technologie	Université de Technologie
de Compiègne	de Compiègne

Laboratoire Roberval UMR CNRS 7337

Labex MS2T

Université de Technologie de Compiègne

Sorbonne Universités

Acknowledgements

Firstly, I would like to express my sincere gratitude to my supervisors Ass. Prof. Pierre FEISSEL and Prof. Thierry DENŒUX for the continuous support of my Ph.D study and related research, for their patience, motivation, and immense knowledge. Their guidance helped me in all the time of research and writing of this thesis.

Besides my supervisors, I would like to thank the members of the jury Prof. Guillaume PUEL, Ass. Prof. David MERCIER, Prof. Thierry TISON, and CNRS Researcher Sébastien DESTERCKE, for their insightful comments and encouragement, but also for the hard questions which incented me to widen my research from various perspectives.

I thank my colleagues from Roberval in Compiègne with whom I spent a huge amount of time during office hours and beyond. Thanks to all of you for the moments we shared.

I wish to thank the unconditional support of my parents despite the long distance. Without your support, nothing would have been possible.

I would like to gratefully acknowledge the support provided for this work under the framework of the Labex MS2T. Last but not least, I would also like to thank the Chinese Scholarship Council for supporting my study in France.

Abstract

In order to obtain more predictive and accurate simulations of mechanical behaviour in the practical environment, more and more complex material models have been developed. Nowadays, the characterization of material properties remains a top-priority objective. It requires dedicated identification methods and tests in conditions as close as possible to the real ones.

This thesis aims at developing an effective identification methodology to find the material property parameters, taking advantages of all available information. The information used for the identification is theoretical, experimental, and empirical: the theoretical information is linked to the mechanical models whose uncertainty is epistemic; the experimental information consists in the full-field measurement whose uncertainty is aleatory; the empirical information is related to the prior information with epistemic uncertainty as well. The main difficulty is that the available information is not always reliable and its corresponding uncertainty is heterogeneous. This difficulty is overcome by the introduction of the theory of belief functions. By offering a general framework to represent and quantify the heterogeneous uncertainties, the performance of the identification is improved.

The strategy based on the belief function theory is proposed to identify macro and micro elastic properties of multi-structure materials. In this strategy, model and measurement uncertainties are analysed and quantified. This strategy is subsequently developed to take prior information into consideration and quantify its corresponding uncertainty.

Key words : *identification, full-field measurement, prior information, model uncertainty, aleatory uncertainty, epistemic uncertainty, theory of belief functions.*

Résumé

Afin d'obtenir des simulations plus prédictives et plus précises du comportement mécanique des structures, des modèles matériau de plus en plus complexes ont été développés. Aujourd'hui, la caractérisation des propriétés des matériaux est donc un objectif prioritaire. Elle exige des méthodes et des tests d'identification dédiés dans des conditions les plus proches possible des cas de service.

Cette thèse vise à développer une méthodologie d'identification efficace pour trouver les paramètres des propriétés matériau, en tenant compte de toutes les informations disponibles. L'information utilisée pour l'identification est à la fois théorique, expérimentale et empirique: l'information théorique est liée aux modèles mécaniques dont l'incertitude est épistémique; l'information expérimentale provient ici de la mesure de champs cinématiques obtenues pendant l'essai et dont l'incertitude est aléatoire; l'information empirique est liée à l'information à priori associée à une incertitude épistémique ainsi. La difficulté principale est que l'information disponible n'est pas toujours fiable et que les incertitudes correspondantes sont hétérogènes. Cette difficulté est surmontée par l'utilisation de la théorie des fonctions de croyance. En offrant un cadre général pour représenter et quantifier les incertitudes hétérogènes, la performance de l'identification est améliorée.

Une stratégie basée sur la théorie des fonctions de croyance est proposée pour identifier les propriétés élastiques macro et micro des matériaux multi-structures. Dans cette stratégie, les incertitudes liées aux modèles et aux mesures sont analysées et quantifiées. Cette stratégie est ensuite étendue pour prendre en compte l'information à priori et quantifier l'incertitude associée.

Mots clés : *identification, mesure en champ complet, information à priori, incertitude modèle, incertitude aléatoire, incertitude épistémique, théorie des fonctions de croyance.*

Table of contents

List of figures

List of tables

Chapter 1

Introduction

1.1 Background and motivation

Material characterizations are invaluable to engineers to find the best structures that offer the required performance. More complex material models can provide more predictive results and better performance in complicated and large-scale simulations. However, we must carry out the identifications based on tests in which the experimental conditions should be as close as possible to the real working conditions. This requires more complex specimens and loading, and dedicated identification methods need to be developed. Efficient and effective identification methodologies are increasingly required to find the parameters describing mechanical properties from available information.

The available information used in identification comes from three sources: theoretical, experimental, and empirical information. Identification methods should handle all the information to extract the model parameters. The main difficulty is that information and the corresponding uncertainty have different natures.

- Theoretical information is referred to the mechanical models which provide the mathematical point of view to understand the real world. Theoretical information is tainted with model uncertainty which comes from insufficient information or approximation of the real model.

- Experimental information is related to the data measured during the experimental tests. The measurement uncertainty is unavoidable due to the limitation of measurement devices.

- Empirical information can be explained as the prior information which should be considered when it is available. Prior information usually comes from expert opinions which accompany with subjective imprecision.

The identification methods for heterogeneous tests are regarded as inverse methods which couple experiments and calculations. Ill-posedness (the solution may be non-existent, non-unique, or discontinuous) is a typical feature for identification problems. It is important to take prior information into consideration to overcome the ill-posed characters. Meanwhile, quantification of uncertainty is significant for the identification methods because it offers the knowledge of uncertainty on materials. One challenge of this study is to propose a methodology that can handle the different natures of uncertainty.

Uncertainty can be divided into two types [Helton and Oberkampf, 2004]: aleatory uncertainty arising because systems are potentially various, such as geometry, material property, and measurement uncertainty; epistemic uncertainty arising from lack of knowledge or incomplete information, such as subjective uncertainty on a new material properties due to poor understanding, model uncertainty due to physics simplification.

Historically, both aleatory and epistemic uncertainty can be represented by a mathematical structure provided by probability theory [Aprostolakis, 1990] [Parry and Winter, 1981]. However, the discussion on the alternative representations of epistemic uncertainty never stops. Moreover, many non-probabilistic methods have been proposed as alternatives to probabilistic approaches when information is incomplete and insufficient [Baudrit and Dubois, 2006] [Aven, 2011] [Zio and Pedroni, 2013], including p-box, fuzzy set, random sets, possibility theory and theory of belief functions (evidence theory), etc. The uncertainty treated in this thesis is diverse in sources and types. Measurement and model uncertainties, which are treated in Chapter 5, correspond, respectively, to aleatory and epistemic uncertainty. The uncertainty on prior information, which is considered in Chapter 6, is interpreted as epistemic uncertainty. Thus, multiple uncertainty representation methods are applied to encode the heterogeneous uncertainties. A general framework should be developed to integrate, propagate and quantify the uncertainty represented by the different methods. During this process, computational efficiency should be paid special attention.

The context in which this work engages is the identification of elastic properties from the full-field measurements. The full-field measurement technologies have been developed for 20 years. They can provide very rich measurement data to execute the identification from heterogeneous tests. Digital Image Correlation (DIC) is an inherently contactless and non-intrusive measurement technique that uses the images

acquired at different stages of tests. It can measure kinematic fields of surfaces (or in volumes) of loaded specimens and structures. Thus, DIC has been chosen to obtain the full-field measurements in this thesis, due to its efficiency and high tolerance to aggressive conditions.

In this work, we consider two applications, identification of mono-structure and multi-structure materials. The mono-structure materials are related to traditional materials and they have been widely used in engineering. The multi-structure materials (e.g composite materials, polycrystalline metals, porous materials, etc.) are becoming a key research point due to their increasing applications. The characterization of the two types of materials is very useful in practice.

1.2 Structure

This thesis is presented according to the following organisation:

- The first chapter presents the background of the study.
- In the second chapter, the full-field measurement techniques and deterministic identification methods are presented and compared.
- In the third chapter, the uncertainty representation approaches, including probabilistic and non-probabilistic approaches, are introduced and compared to illustrate the reasons for selecting belief function theory. The non-deterministic identification methods are discussed in this chapter.
- In the fourth chapter, the mechanical models used in this study are introduced. The different natures of uncertainty in identification are analysed to choose suitable uncertainty representation approaches. A general framework based on likelihood-based belief functions is proposed.
- An identification strategy which can quantify both measurement and model uncertainties are proposed in the fifth chapter. The presentation of this strategy is explained in detail in the context of multi-structure materials. Illustrating examples of identifying macro and micro properties of multi-structure materials are provided to show the effectiveness and robustness of the proposed strategy.
- The sixth chapter introduces how to take prior information into account and quantify its uncertainty in identification. Cooperating with the strategy in the fifth chapter, prior information, model, and measurement uncertainties

are all quantified within the same framework. Several numerical applications in identifying the mono-structure and multi-structure materials properties are illustrated in this chapter.

- Some conclusions are given in the seventh chapter.

Chapter 2

Identification of mechanical models

The study of this thesis is based on full-field measurements. The measurement technologies and deterministic identification methods, which have been developed significantly, will be introduced in this chapter. The non-deterministic identification approaches from the full-field measurements have been paid very little attention until now. A non-deterministic strategy from the full-field measurements will be proposed from Chapter 4.

2.1 Full-field measurement technologies

The improvement of optical and image processing techniques makes non-contact measurement more and more popular in material characterizations. The full-field measurement techniques, which measure global quantities (a field record of displacement, strain, temperature), offer a large amount of experimental data to be explored. Compared with traditional measurement techniques, the rich experimental information obtained from full-field measurements allows identifying the materials under heterogeneous conditions (e.g., complex specimen geometry, non-uniform loading, heterogeneous material). In [Grédiac, 2004], full-field measurement techniques are classified into two main categories: non-interferometric and interferometric methods. Non-interferometric methods extract the spatial variation information of light intensity, including speckle photography [Archbold et al., 1970], grid method [Parks, 1982], image correlation [Peters and Ranson, 1982]; the interferometric methods extract the phase variation information of signals, including speckle interferometry [Jones and Wykes, 1989], Moiré interferometry [Asundi et al., 1989].

Digital Image correlation (DIC) is a vision-based measurement technique proposed by [Peters and Ranson, 1982]. DIC requires no special light or surface preparation

in many cases, as a result images can be obtained from a wide variety of sources, including Conventional Charge-coupled Device (CCD) [Ackermann, 1984] [Nguyen et al., 2016], high-speed video [Kirugulige et al., 2007], Scanning Electron Microscope (SEM) [Sutton et al., 2006] [Jin et al., 2008] and Atomic Force Microscope (AFM) [Cho et al., 2005] [Xu et al., 2008], Computed Tomography (CT) image [Verhulp et al., 2004], X-ray tomography [Bay et al., 1999], etc. During two decades of development, a lot of studies have been done to improve the accuracy in DIC. [Chen et al., 1993] applied fast-Fourier transform to study crack-tip deformation fields. [Feissel et al., 2013] used the diffuse approximation method to filter measurement error and reconstruct strain fields. [Hassan et al., 2016] focused on the selection of subset size in DIC. [Réthoré et al., 2008] combined extended finite element method (X-FEM) with digital image correlation. The enrichment functions made it possible to describe the discontinuities in displacement fields even when the mesh was coarse. In [Leclerc et al., 2009], DIC was coupled with the finite element model (FEM) to enhance accuracy and robustness of the identification. Multicamera systems make it possible to construct a three-dimensional deformation field of a surface [Helm et al., 2001] [Verhulp et al., 2004]. The digital volume correlation can be seen as an extension of digital image correlation. It can reconstruct the interior kinematic fields in specimens [Bay et al., 1999].

In short, DIC has the following advantages:

- it is a non-contact measurement. It minimises the influence on the specimens in a test;
- it is easy to use. It requires no special light and surface preparation in many cases;
- it has high efficiency. The images can obtain simultaneously during the tests.

These advantages make DIC more and more popular. In the following section, the principles of DIC will be introduced.

2.2 Measurement from digital image correlation

DIC relies on matching a reference image and deformed image obtained before and after loading in a test. Here we take the two-dimensional DIC as an example to briefly introduce its basic concepts. Considering two configurations respectively recorded before and after a test, the first one is called "reference image", denoted f, and the second one is "deformed image", denoted g. The configurations are stored as positive

integers, which are the gray intensity of pixels. The selection of subsets is a necessary step in DIC. Not only should the subset be large enough to have good intensity variation, but also it needs to be small enough to follow the first-order displacement function approximation used by DIC. DIC reconstructs a deformation field by matching the subsets of the two images. The correlation coefficient is:

$$R = \sum_{i=-M}^{M} \sum_{j=-M}^{M} \frac{\left(f(x_i, y_j) - \bar{f}\right)\left(g(x_i^{'}, y_j^{'}) - \bar{g}\right)}{\sqrt{\sum_{i=-M}^{M} \sum_{j=-M}^{M} \left(f(x_i, y_j) - \bar{f}\right)^2 \sum_{i=-M}^{M} \sum_{j=-M}^{M} \left(g(x_i^{'}, y_j^{'}) - \bar{g}\right)^2}}, \tag{2.1}$$

where $f()$ and $g()$ represent the gray intensity of a pixel in the reference and deformed image, M is the number of subsets in horizontal and vertical directions. The relationship between (x_i, y_j) in the reference image and $(x_i^{'}, y_j^{'})$ in the deformed image is characterized by mechanical transformation functions which are usually approximated by polynomial expressions [Bornert et al., 2009]. Here we make use of the linear assumption to link (x_i, y_j) with the corresponding position $(x_i^{'}, y_j^{'})$:

$$\begin{aligned} x^{'} - x &= u + \frac{\partial u}{\partial x}\mathrm{d}x + \frac{\partial u}{\partial y}\mathrm{d}y, \\ y^{'} - y &= v + \frac{\partial v}{\partial x}\mathrm{d}x + \frac{\partial v}{\partial y}\mathrm{d}y, \end{aligned} \tag{2.2}$$

where u and v are the displacement components at the center of the subset in x and y direction. In the 2D case, the correlation coefficient R is a function of six independent variables denoted by the vector:

$$\boldsymbol{u} = (u, v, \frac{\partial u}{\partial x}, \frac{\partial u}{\partial y}, \frac{\partial v}{\partial x}, \frac{\partial v}{\partial y})^T.$$

The displacement field is obtained by maximising the correlation coefficient R with respect to the six variables. For the 3D case, the correlation coefficient R depends on 12 variables. More detail of DIC can be found in [Michel et al., 2012] [Hassan et al., 2016].

Measurement accuracy using DIC depends on image noise caused by camera sensors, employed transformation functions, structure of the speckle patterns, subset size [Gao et al., 2016] [Bornert et al., 2009] etc. In the literature, a number of algorithms [Bruck et al., 1989] [Luu et al., 2011] [Pan, 2013] have been proposed to increase the measurement accuracy. However measurement uncertainty is inevitable, and it is often described by statistical properties of random error (e.g., Root-mean-square-error [Bornert et al., 2009] [Luu et al., 2011], mean and standard deviation error [Pan, 2013]).

The measurement data acquired from DIC are rich, have a high quality, and their accuracy can be assessed. These features are helpful for improving the performance of identification. Especially, the assessable accuracy is very significant to uncertainty quantification in identification. Therefore, the full-field measurement from DIC is selected as the experimental information.

2.3 Identification methods

Identification problems are a kind of inverse problems based on models characterised by parameters. Forward problems focus on calculating the response given the excitation and model parameters, while inverse problems focus on inferring and reconstructing the excitation or model parameters based on the known or partially known measurement of response. Consider a forward problem described by:

$$\text{find } \boldsymbol{u} = \boldsymbol{u}(\boldsymbol{\theta}) \text{ such that } \boldsymbol{g}(\boldsymbol{\theta}, \boldsymbol{u}) = \mathbf{0}, \text{ with } \boldsymbol{\theta} \text{ given }, \tag{2.3}$$

where $\boldsymbol{u}$ is the response (displacement in this thesis), $\boldsymbol{\theta}$ is referred to the model parameters. The identification formulation can be written as follows:

$$\text{find } \boldsymbol{\theta} \in \boldsymbol{\Theta} \text{ such that } \boldsymbol{g}(\widetilde{\boldsymbol{u}}, \boldsymbol{\theta}) = \mathbf{0}, \tag{2.4}$$

where $\widetilde{\boldsymbol{u}}$ is the measurement (observation) of $\boldsymbol{u}$ (or a part of $\boldsymbol{u}$), and $\boldsymbol{\Theta}$ denotes the parameter space in which $\boldsymbol{\theta}$ is sought. The formulation in Eq. (2.4) is often ill-posed because it violates at least one of the Hadamard well-posedness conditions [Hadamard, 1902]: (1) a solution exists; (2) the solution is unique; (3) the solution's behaviour changes continuously with the data. The measurement and model uncertainties will sharpen the non-existence or instability of Eq. (2.4). To solve an ill-posed problem, a well-posed problem must be formulated. Several approaches are possible, including relaxing some equations, reformulating a minimisation problem, adding prior information, and reducing the size of the parameter space.

Full-field measurement techniques offer rich measurement information which is helpful to overcome ill-posedness of identification. The rich data can reduce the size of parameter space and sensibility to measurement uncertainty, which will make the solution unique and stable. Recently, a lot of approaches focus on the exploitation of full-field measurements to identify model parameters, including the Finite Element Model Updating (FEMU) method [Kajberg and Lindkvist, 2004] [Azzouna et al., 2013] [He et al., 2016], Constitutive Relation Error Method (CREM) [Latourte et al., 2008]

[Florentin and Lubineau, 2010], Modified Constitutive Relation Error Method (M-CREM) [Azzouna et al., 2015] [Huang et al., 2016], Equilibrium Gap Method (EGM) [Claire et al., 2004] [Réthoré et al., 2009] [Périé et al., 2009]. The methods above reformulate an identification problem as a minimization problem targeting to solve the nonexistence problem. The Virtual Fields Method (VFM) [Grédiac, 1989] [Chalal et al., 2006] relies on the principle of virtual work (PVW). It is a method based on the weak form of equilibrium to induce an identification of the sought parameters. Tikhonov regularization [Tikhonov and Arsenin, 1977] [Tikhonov, 1995] and Bayesian inference [Tarantola, 2005] [Zhang et al., 2012] regularize identification problems by adding prior information to solve the uniqueness and continuous problem. The approaches above, except for Bayesian inference, belong to the deterministic strategy. The deterministic approaches will be introduced in this chapter, while the Bayesian inference, as a non-deterministic method, will be presented in Chapter 3.

2.3.1 Finite element model updating method

The Finite Element Model Updating (FEMU) method [Kajberg and Lindkvist, 2004] [Azzouna et al., 2013] [He et al., 2016] is based on the Finite Element Model (FEM). The FEMU minimises an objective function defined as the discrepancy between a measured data and its prediction. There are two main ways to formulate objective function. Firstly, the objective functions can be based on force data [Kavanagh and Clough, 1971] [Pagnacco et al., 2007], corresponding to the "force balance method". Secondly, the objective function is defined on displacement data [Collins et al., 1974] [Farhat and Hemez, 1993], corresponding to the "displacement method". Moreover in [Hoc et al., 2003] [Giton, 2006] [Guery et al., 2016], the objective functions of the force balance and displacement methods are combined to form a mixed misfit function. The minimisation problems of objective functions are solved by iterative procedures.

The FEUM can work for both point-wise and full-field measurements. Many investigations focus on the application of the FEMU to parameter identifications. [Fang et al., 2008] identified the damage in a tested reinforced concrete frame using the measurements from piezoelectric accelerometers. [Sun et al., 2015] proposed to identify the temperature-dependent properties of a thermo-elastic structure using the frequency measurement in an unsteady temperature environment. [Kajberg and Lindkvist, 2004] focused on the identification of material subjected to large strains using the displacement field measurement from Digital Speckle Photography (DSP) technology. In [Azzouna et al., 2013], heterogeneous elastic properties were identified based on the filtered full-field data using diffuse approximation algorithm. [He et al., 2016] applied

the FEMU to determine constitutive properties of composite materials using the strain fields measured by DIC.

2.3.2 Constitutive relation error method

The Constitutive Relation Error Method (CREM) was proposed in [Ladeveze and Leguillon, 1983] [Ladevèze et al., 1999] for error estimation in the FEM. Then it was widely used in model updating [Ladevèze et al., 1999] [Barthe et al., 2004] [Bouclier et al., 2013]. The CREM assumes that the constitutive relation equation could be inaccurate, which leads to the constitutive relation error, and therefore, has to be relaxed. Then, a stress field, a displacement field and a set of material parameters are sought as a trade-off of all the available data, enforcing the reliable data and relaxing the non-reliable one. In the elastic case, this leads to the definition of the function:

$$J(\boldsymbol{u},\boldsymbol{\sigma},\boldsymbol{\theta}) = \frac{1}{2}\int_{\Omega}\big(\boldsymbol{\sigma}-\boldsymbol{C}(\boldsymbol{\theta})\boldsymbol{\varepsilon}(\boldsymbol{u})\big):\boldsymbol{C}^{-1}(\boldsymbol{\theta}):\big(\boldsymbol{\sigma}-\boldsymbol{C}(\boldsymbol{\theta})\boldsymbol{\varepsilon}(\boldsymbol{u})\big)\mathrm{d}\Omega, \tag{2.5}$$

where $\boldsymbol{C}$ is the elasticity tensor, $\boldsymbol{u}$ is the displacement field, $\boldsymbol{\varepsilon}(\boldsymbol{u})$ is the strain tensor associated with $\boldsymbol{u}$, and $\boldsymbol{\sigma}$ is the Cauchy stress tensor. The reliable equations define the admissible spaces for both the displacement field and the stress field. Hence, $\boldsymbol{u}$ is in kinematically admissible space, noted $\mathcal{U}_{Ad}$, and $\boldsymbol{\sigma}$ is in a space called statically admissible space, noted $\mathcal{S}_{Ad}$. $\mathcal{U}_{Ad}$ and $\mathcal{S}_{Ad}$ are defined by:

$$\begin{cases} \mathcal{U}_{Ad} = & \{\boldsymbol{u}\in H_1(\Omega)|\boldsymbol{u}=\widetilde{\boldsymbol{u}} \text{ on } \Omega_m, \boldsymbol{u}=\overline{\boldsymbol{u}} \text{ on } \partial_{\mathrm{u}}\Omega\}, \\ \mathcal{S}_{Ad} = & \{\boldsymbol{\sigma}\in H_{div}(\Omega)|\mathrm{div}\boldsymbol{\sigma}=\boldsymbol{0} \text{ on } \Omega,\ \boldsymbol{\sigma}.\boldsymbol{n}=\overline{\boldsymbol{f}} \text{ on } \partial_f\Omega\}, \end{cases} \tag{2.6}$$

where $\widetilde{\boldsymbol{u}}$ is the measurement on Ω_m, Ω_m denotes the measurement domain. Dirichlet boundary condition is defined on $\partial_u\Omega$, Neumann boundary condition is defined on $\partial_f\Omega$. CREM measures the energy discrepancy between the stress field and another stress field evaluated from displacement field [Bonnet, 2012]. The minimisation of Eq. (2.5) under the conditions of Eq. (2.6) can be solved by the alternate direction method:

$$(\widehat{\boldsymbol{u}},\widehat{\boldsymbol{\sigma}},\widehat{\boldsymbol{\theta}}) = \min_{\boldsymbol{\theta}}\min_{\boldsymbol{\sigma},\boldsymbol{u}} J(\boldsymbol{u},\boldsymbol{\sigma},\boldsymbol{\theta}). \tag{2.7}$$

The CREM has been used for the identification of elastic properties [Constantinescu, 1995] and nonlinear constitutive models [Latourte et al., 2008]. Recently the CREM has been extended to a large number of applications. In [Deraemaeker et al., 2002], the CREM was used with a reduction model to the updating of industrial structures

with many degrees of freedom. [Faverjon and Sinou, 2008] applied the CREM to detect the number of cracks in a beam. Moreover, both the crack positions and sizes were estimated with satisfactory precision. [Florentin and Lubineau, 2010] presented a variant of the CREM in which the construction of statically admissible fields was optimised. This method was shown to be effective for the identification of heterogeneous isotropic elastic properties. [Bouclier et al., 2013] proposed a real-time validation of mechanical model based on the CREM and Proper Generalized Decomposition (PGD), which was used to run a validation process quickly.

The Modified Constitutive Relation Error Method (M-CREM) [Ladeveze, 1993] [Calloch et al., 2002] is a variant form of the CREM. The idea is to redefine the sets of reliable and less reliable equations. In particular, the measurements of either load or displacement should be considered as less reliable and the corresponding equations should be relaxed. The function is therefore modified by introducing a penalty term:

$$J(\boldsymbol{u},\boldsymbol{\sigma},\boldsymbol{\theta}) = \frac{1}{2}\int_{\Omega}\left(\boldsymbol{\sigma}-\boldsymbol{C}(\boldsymbol{\theta})\boldsymbol{\varepsilon}(\boldsymbol{u}) : \boldsymbol{C}^{-1}(\boldsymbol{\theta}) : \left(\boldsymbol{\sigma}-\boldsymbol{C}(\boldsymbol{\theta})\boldsymbol{\varepsilon}(\boldsymbol{u})\mathrm{d}\Omega + \alpha\cdot\frac{1}{2}\int_{\Omega_m}||\boldsymbol{u}-\widetilde{\boldsymbol{u}}||^2\mathrm{d}\Omega,\right.\right. \tag{2.8}$$

where α is a positive weighting coefficient. It can be defined by L-curve [Calvetti et al., 2000] or Morozov's discrepancy principle [Anzengruber et al., 2014]. The M-CREM was firstly used in dynamics [Ladeveze et al., 2006a] and transient dynamics [Allix et al., 2003] [Feissel and Allix, 2007]. [Huang et al., 2016] focused on the identification of elastic properties from DIC data in statics and the dealing of various kinds of boundary conditions (unknown or known) was especially discussed.

2.3.3 Equilibrium gap method

The CREM derives from unreliable constitutive equation, while the Equilibrium Gap Method (EGM) is based on relaxing the equilibrium equation:

$$\mathrm{div}\boldsymbol{\sigma}(\boldsymbol{u},\boldsymbol{\theta}) + \boldsymbol{f} = \boldsymbol{0}. \tag{2.9}$$

This method was proposed for identifying the elastic properties taking the form of a scalar field $C(\boldsymbol{x})$, i.e.

$$\boldsymbol{C}(\boldsymbol{x}) = C(\boldsymbol{x})\boldsymbol{C}_0, \tag{2.10}$$

where $\boldsymbol{C}_0$ is a reference medium [Avril et al., 2008a]. It can identify the distribution of elastic properties and its evolution during the test from measured displacement [Claire

et al., 2002]. The objective function can be written as follows:

$$J(\boldsymbol{C}) = \alpha V(\Omega) \int_{\Omega} ||\mathrm{div}\boldsymbol{\sigma}(\boldsymbol{u}, \boldsymbol{C}) + \boldsymbol{f}||^2 \mathrm{d}\Omega + \beta S(\partial\Omega) \int_{\partial\Omega} ||\boldsymbol{C} : \nabla \boldsymbol{u} \cdot \boldsymbol{n} - \boldsymbol{t}||^2 \mathrm{d}\partial\Omega, \quad (2.11)$$

where V is the domain volume and S is the area of the boundary $\partial\Omega$, α and β are the weight coefficients to be chosen, $\boldsymbol{u}$ is the displacement field, and $\boldsymbol{u} = \widetilde{\boldsymbol{u}}$ in the measured domain Ω_m. The second term of the right hand of the Eq. (2.11) corresponds to information on the loading imposed by Neumann boundary condition.

In [Claire et al., 2004], the EGM was applied to identify the spatial distribution of the damage variable $D(\boldsymbol{x})$. The elastic tensors $\boldsymbol{C}(\boldsymbol{x})$ were represented by $D(\boldsymbol{x})$:

$$\boldsymbol{C}(\boldsymbol{x}) = (1 - D(\boldsymbol{x}))\boldsymbol{C}_0, \quad (2.12)$$

where $0 \leq D(\boldsymbol{x}) \leq 1$. In [Réthoré et al., 2009], the EGM was applied as a mechanical filter to reduce the uncertainty of measurement field from DIC. The correlation algorithm was penalized by a minimisation of the equilibrium gap condition. In [Crouzeix et al., 2009] an orthotropic variant of the the EGM was applied to identify the anisotropic damage law of the composite material under a biaxial loading.

2.3.4 Virtual field method

The Virtual Field Method (VFM) is an approach based on auxiliary fields proposed by [Grédiac, 1989]. This method is suitable for the case where the strain field $\boldsymbol{\varepsilon}$ is experimentally known (possibly via differentiation of a measurement displacement field $\widetilde{\boldsymbol{u}}$), and the loading conditions are assumed to be known [Avril et al., 2008a]. The basic idea of VFM relies on the principle of virtual work (PVW), taking the form:

$$-\int_{\Omega} \boldsymbol{\sigma} : \nabla \boldsymbol{u}^* \mathrm{d}\Omega + \int_{\partial\Omega} \boldsymbol{t} \cdot \boldsymbol{u}^* \mathrm{d}\partial\Omega = \int_{\Omega} \rho \ddot{\boldsymbol{u}} \cdot \boldsymbol{u}^* \mathrm{d}\Omega, \quad (2.13)$$

where $\boldsymbol{u}^*$ is a virtual displacement field. Based on constitutive model with parameter $\boldsymbol{\theta}$ to be identified, the stress field $\boldsymbol{\sigma}$ is expressed from the known strain $\boldsymbol{\varepsilon}$, ρ is the density, $\ddot{\boldsymbol{u}}$ is the acceleration field. Then, particular virtual fields have to be chosen in order to obtain as many equations as unknown material parameters. The virtual fields can be construct by means of polynomial functions [Grédiac and Pierron, 1998], special linear equations [Grédiac et al., 2002] over the whole specimen, piecewise polynomial functions [Toussaint et al., 2006], or finite elements fields [Avril and Pierron, 2007].

The VFM has been used in a large scope of applications, such as identifying linear elastic parameters [Grédiac and Pierron, 1998] [Grédiac et al., 2002], visco-elastic parameters [Giraudeau and Pierron, 2003], elastic-plastic parameters [Avril et al., 2008b]. [Pierron et al., 2000] identified the four through-thickness parameters of thick laminated composites based on four independent virtual fields. The solutions can be directly obtained for the linear cases, and iteratively obtained for the non-linear cases.

2.3.5 Tikhonov regularization

Non-uniqueness and discontinuity are two frequent obstacles in parameter identification problems. To solve this problem, it is a good choice to formulate and exploit available prior information in addition to measurement information. Tikhonov regularization technique [Tikhonov and Arsenin, 1977] [Tikhonov, 1995] takes prior information into account by adding a stabilizing function to original the objective function:

$$\mathcal{J}(\boldsymbol{\theta}) = J(\boldsymbol{\theta}) + \alpha\mathcal{R}(\boldsymbol{\theta}), \tag{2.14}$$

where $J(\cdot)$ defines the discrepancy between the measurements and their predictions:

$$J(\boldsymbol{\theta}) = ||\boldsymbol{u}(\boldsymbol{\theta}) - \widetilde{\boldsymbol{u}}||^2. \tag{2.15}$$

The coefficient α is the regularization parameter, and $\mathcal{R}(\cdot)$ is the stabilizing function. There are several choices of $\mathcal{R}(\cdot)$. One choice can be written as follows:

$$\mathcal{R}(\boldsymbol{\theta}) = ||\boldsymbol{\theta} - \boldsymbol{\theta}_0||^2, \tag{2.16}$$

where $\boldsymbol{\theta}$ will be close to the prior value $\boldsymbol{\theta}_0$.

The choice of the coefficient α in Eq. (2.14) is a crucial point for Tikhonov regularization. The rules of choice depend on three categories [Anzengruber, 2011]:

- only the noise level of measurements, e.g., the most common choice is $\alpha = c \cdot \delta^r$, where δ is the noise level, c and r are parameters to be chosen;
- only the measurement, e.g., L-curve method [Calvetti et al., 2000];
- both the measurement and its noise level, e.g., Morozov's discrepancy principle [Bonesky, 2008].

2.4 Conclusion

In this chapter, we introduced some popular full-field measurement techniques and parameter identification methods dedicated to this type of data. The identification methods presented above are part of deterministic strategies. They focus on finding the parameters that coincide best with the measurements. In this group, FEMU, CREM, M-CREM, VFM, and EGM can hardly consider prior information, and most cannot quantify the uncertainty of information. They can be coupled to Tikhonov regularization techniques which consider prior information but fail to quantify uncertainty. However, uncertainty is inevitable in identification problems, and it needs to be managed. To quantify the uncertainty, it is necessary to research the uncertainty nature, representation, and propagation. In the next chapter, we will discuss the uncertainty in mechanical models, the representation approaches and the non-deterministic identifications.

Chapter 3

Uncertainty representation approaches

3.1 Uncertainty in mechanical models: Aleatory vs. Epistemic Uncertainty

Even though it is often ignored, uncertainty is unavoidable in identification. On the one hand, measurement uncertainty always accompanies the measurement processes. On the other hand, information on features of the studied systems, such as geometry, constitutive materials and boundary conditions, is usually partially unknown for identification problems. In engineering practice, we usually construct some models with simplified boundary conditions, loads or material properties. Under the simplification, we can calculate plenty of mechanical problems. But the researchers should pay attention to the confidence we have in our mechanical models and their ability to simulate the real situations. All the mechanical models are based on the knowledge we have. The unknown areas are so huge that we cannot ignore them. Therefore, there has been an increasing interest in modelling uncertainty. Considering the different natures and sources, uncertainty can be separated into two types: aleatory uncertainty and epistemic uncertainty.

Aleatory uncertainty is underlying and intrinsic variability of physical quantities. For example, measurement noise can be seen as aleatory uncertainty. It is the inherent property of measurement devices. We normally see the aleatory uncertainty as objective and irreducible. Aleatory uncertainty is often quantified by random variables or probability distributions when sufficient information is available to establish the probability distributions.

In contrast with aleatory uncertainty, epistemic uncertainty results from the lack of knowledge or incomplete information, e.g., lack of sufficient data in the statistical process, fuzzy empirical opinion and limited understanding of the complex physical phenomenon. Due to its subjective nature, epistemic uncertainty may be reduced with additional information, e.g., more observations, better models, and more precise knowledge.

In conclusion, aleatory uncertainty is due to variability, it is irreducible and objective; in contrast, epistemic uncertainty is due to ignorance, it is reducible and subjective [Zhang, 2005]. Considering the different natures of the two types of uncertainty, many uncertainty representation methods have been proposed recently. In general, they are separated into probabilistic approaches and non-probabilistic approaches.

3.2 Probabilistic approaches

Research on probability started in the 17th century. In general, probability is a measure of the chance of an event. We have three choices to relate a real event to probability [Pinsky and Karlin, 2010]: (1) equally likely property (2) long run frequency of appearance (3) quantitative subjectivity. Next, we will talk about probability theory in uncertainty representation and propagation.

3.2.1 Uncertainty representation in probability theory

Let Ω be the sample space of a random phenomenon, which contains all possible outcomes. A real random variable X is a measurable mapping:

$$X : \Omega \mapsto A \subseteq \mathbb{R}.$$

When A is continuous, the random variable is said continuous, otherwise it is said discrete. A real random vector $\boldsymbol{X}$ is a measurable mapping:

$$\boldsymbol{X} : \Omega \mapsto \boldsymbol{A} \subseteq \mathbb{R}^d,$$

where $d \geq 2$. The real random vector can be considered as a vector whose components are random variables. A random field $H(\boldsymbol{x}, \omega)$ is a set of random variables indexed by a continuous parameter $\boldsymbol{x} \in \mathbb{R}^d$, where $\omega \in \Omega$, and $\boldsymbol{x}$ describes the geometry of a system [Sudret and Der Kiureghian, 2000]. Random fields are non-numerable infinite and computationally intractable. Thus, several discretization methods for

random fields have been developed in the literature including the midpoint method [Der Kiureghian and Ke, 1988], the shape function method [Liu et al., 1986], the spatial average approach [Vanmarcke and Grigoriu, 1983], the Karhunen-Loève Expansion [Loeve, 1978], the expansion optimal linear estimation method [Li and Der Kiureghian, 1993], the orthogonal series expansion [Zhang and Ellingwood, 1994].

Plenty of probabilistic approaches for propagating uncertainty through mechanical models have been developed targeting various interests. [Liu et al., 1986] obtained the mean and variance of displacements and stresses for a non-linear dynamic structure. The first-order reliability method was used in [Der Kiureghian and Ke, 1988] for reliability analysis of structures with stochastically varying properties and subjected to random loads. [Ghanem and Spanos, 1991] presented the spectral stochastic finite element method to predict the whole Probability Density Function (PDF) of response with high efficiency. In [Papadrakakis and Papadopoulos, 1996], the weighted integral method and Monte Carlo simulation were used together to produce robust and efficient solutions for the stochastic finite element analysis of space frames. The variability of the displacement response and eigenvalues of structures with multiple uncertain materials and geometric properties were studied using variability response functions in [Graham and Deodatis, 2001].

3.2.2 Identification based on Bayesian Inference

The identification based on Bayesian inference is the most general non-deterministic method using probability theory. Compared with the deterministic methods which provide a single value, Bayesian identification provides a joint probability distribution to represent the possible values of identified parameters. In identification, there is always a discrepancy between the measurement and the predicted model (e.g. FEM) because of measurement and model uncertainties:

$$\widetilde{\boldsymbol{u}} = \boldsymbol{u}(\boldsymbol{\theta}) + \boldsymbol{e}_{meas} + \boldsymbol{e}_{model}, \tag{3.1}$$

where $\widetilde{\boldsymbol{u}}$ is the measurement field, $\boldsymbol{u}(\boldsymbol{\theta})$ is the predicted model, $\boldsymbol{e}_{meas}$ is the measurement error, $\boldsymbol{e}_{model}$ is the model error.

Measurement error, which is represented by a probability distribution, arises from the finite accuracy of measurement devices. The model error comes from the simplification or incomplete knowledge on the real system. In the Bayesian formulation, the model error is encoded by a probability distribution as well. An advantage of Bayesian inference is that prior information on material properties can be accounted using

a prior probability distribution. There are several principles to choose the prior distribution [Zhang, 2010]:

- engineering judgement;
- maximum entropy principle;
- uniform distribution if there is no useful information.

The joint probability distribution of model parameters $\boldsymbol{\theta}$ given the measurement displacement fields $\widetilde{\boldsymbol{u}}$ can be written by Bayes' formula:

$$p(\boldsymbol{\theta}|\widetilde{\boldsymbol{u}}) = \frac{p(\widetilde{\boldsymbol{u}}|\boldsymbol{\theta})p(\boldsymbol{\theta})}{\int p(\widetilde{\boldsymbol{u}}|\boldsymbol{\theta})p(\boldsymbol{\theta})\mathrm{d}\boldsymbol{\theta}}, \tag{3.2}$$

where $p(\boldsymbol{\theta})$ is the prior probability distribution which represents the prior information, $p(\widetilde{\boldsymbol{u}}|\boldsymbol{\theta})$ is the likelihood which accounts for measurement information, $p(\boldsymbol{\theta}|\widetilde{\boldsymbol{u}})$ is the posterior probability distribution which combines the prior information and the measurement.

Several operations can be applied to the posterior distribution [Zhang, 2010]:

- normalization $c = \int p(\widetilde{\boldsymbol{u}}|\boldsymbol{\theta})p(\boldsymbol{\theta})\mathrm{d}\boldsymbol{\theta}$;
- marginalization $p(\theta_i|\widetilde{\boldsymbol{u}}) = \int p(\boldsymbol{\theta}|\widetilde{\boldsymbol{u}})\mathrm{d}\theta_1 ... \mathrm{d}\theta_{i-1}\mathrm{d}\theta_{i+1} ...$;
- expectation of posterior distribution $E(\boldsymbol{\theta}|\widetilde{\boldsymbol{u}}) = \int \boldsymbol{\theta} p(\boldsymbol{\theta}|\widetilde{\boldsymbol{u}})\mathrm{d}\boldsymbol{\theta}$;
- optimization of posterior distribution $\widehat{\boldsymbol{\theta}} = \arg\max_{\boldsymbol{\theta}} p(\boldsymbol{\theta}|\widetilde{\boldsymbol{u}})$.

Bayesian identification has been used in several applications. [Gogu et al., 2010] compared the least-square method with Bayesian inference for identifications based on tests. They proved that Bayesian approach led to more accurate results for two examples: identifying the elastic parameters of a three-bar truss from point-wise strain measurements and identifying the elastic parameters of a composite plate from natural frequency measurements. In [Chazot et al., 2012], poroelastic parameters were characterised from point-wise pressure measurements based on Bayesian inference. The literature addressing identification from the full-field measurement is rather rare. In [Gogu et al., 2013], Bayesian inference was applied to identify elastic properties of a multi-directional laminated plate using the full-field displacement measurements from Moiré interferometry. Proper Orthogonal Decomposition (POD) was used to improve computational efficiency. Finally, both properties and their uncertainty structures

(e.g., mean values, standard deviations, correlation) were obtained. Compared with the deterministic strategies, the Bayesian inference can identify the probability density function of the parameters. The uncertainty quantification in Bayesian inference is important for reliability-based designs.

As discussed in Chapter 1, one of the most commonly recognised distinctions in uncertainty types is between aleatory and epistemic uncertainty. The most widely used representation method for aleatory uncertainty is probability theory. However, epistemic uncertainty derives from ignorance and incomplete information of the systems. Scholars have debated a lot about using probability theory to represent uncertainty in the presence of limited knowledge [Klir, 1989] [Ferson and Ginzburg, 1996] [Helton and Oberkampf, 2004] [Oberkampf et al., 2004]. Thus, some alternative non-probabilistic approaches have been proposed to represent epistemic uncertainty.

3.3 Non-Probabilistic approaches

3.3.1 Interval theory

An interval expresses the knowledge that the variable is comprised between two values. Interval uncertainty can be characterised by characteristic function (membership function) $\chi_I : \mathbb{R} \to \{0, 1\}$,

$$\chi_I(x) = \begin{cases} 1 & \underline{I} \leq x \leq \overline{I}, \\ 0 & \text{otherwise.} \end{cases} \tag{3.3}$$

$\underline{I}$ and $\overline{I}$ are, respectively, the upper and lower limit of interval $[I]$. The binary operators $* \in \{+, -, \times, \div, \max, \min\}$ between two intervals are defined as follows:

$$[I] * [J] = \{x * y | x \in [I], y \in [J]\}. \tag{3.4}$$

If at least one of the matrix elements is an interval, then this matrix is an interval matrix, noted as $[\boldsymbol{A}]$. An $n \times 1$ interval matrix is an interval vector $[\boldsymbol{b}]$ which is also referred to as a box (2 dimensions), cube (3 dimensions) or hyper-cube (3 or more dimensions). A linear interval equation with an $n \times n$ interval matrix $[\boldsymbol{A}]$ and an $n \times 1$ interval vector $[\boldsymbol{b}]$ can be defined as follows:

$$Ax = b \quad (A \in [\boldsymbol{A}], b \in [\boldsymbol{b}]). \tag{3.5}$$

In general, the solution set of Eq. (3.5) has a very complicated shape and is expensive to compute. In practice, we want to find a set containing the solution set while still small enough to be practically useful. The commonly used methods for linear interval equations include the vertex method, the perturbation method, optimisation, and Monte Carlo sampling.

3.3.1.1 Vertex method

The vertex method [Akpan et al., 2001] is also called the combinational method. Considering the linear interval equations (3.5), the vertex points or extreme points of the interval elements are denoted as:

$$\begin{aligned} \hat{a}_{ij}^m &= \{\underline{a}_{ij} \text{ or } \overline{a}_{ij}\}, \quad m = 1, \cdots, 2^{n\times n}, \\ \hat{b}_i^q &= \{\underline{b}_i^q \text{ or } \overline{b}_i^q\}, \quad q = 1, \cdots, 2^n, \end{aligned} \tag{3.6}$$

where $\hat{a}_{ij}^m$ is the element of the vertex matrix $\boldsymbol{A}^m$ and $\hat{b}_i^q$ is the element of the vertex vector $\boldsymbol{b}^q$. The range of x can be determined by considering all possible combinations of the bounds of the interval elements:

$$\hat{\boldsymbol{A}}^m \hat{\boldsymbol{x}}^{mq} = \hat{\boldsymbol{b}}^q, \quad m = 1, \cdots, 2^{n\times n}, \quad q = 1, \cdots, 2^n, \tag{3.7}$$

$$[\underline{x}_i, \overline{x}_i] = [\min_{m,q}(x_i^{mq}), \max_{m,q}(x_i^{mq})], \tag{3.8}$$

where x_i^{mq} is the element of the vector $\boldsymbol{x}^{mq}$. The vertex solution can be used for monotonic systems. The computational effort increases exponentially with the number of matrix interval elements.

3.3.1.2 Perturbation method

The perturbation method [Chen et al., 2002] [Chen and Yang, 2000] is based on the first-order approximation of the output about the middle points of interval space. Because of the first derivative information, the computational effort is smaller than that of vertex solution. This method assumes that the uncertainty is small around the middle points. For a linear equation:

$$\boldsymbol{A}_0 \boldsymbol{x}_0 = \boldsymbol{b}_0, \tag{3.9}$$

where $\boldsymbol{A}_0$ is an $n \times n$ matrix, $\boldsymbol{b}_0$ is an $n \times 1$ vector, the perturbed system can be written as follows:

$$(\boldsymbol{A}_0 + \Delta\boldsymbol{A})(\boldsymbol{x}_0 + \Delta\boldsymbol{x}) = \boldsymbol{b}_0 + \Delta\boldsymbol{b}. \tag{3.10}$$

Expanding the perturbed system and neglecting the higher order part, we have:

$$\Delta\boldsymbol{x} \approx \boldsymbol{A}_0^{-1}(\Delta\boldsymbol{b} - \Delta\boldsymbol{A}\boldsymbol{x}_0), \tag{3.11}$$

where $\Delta\boldsymbol{A}$ and $\Delta\boldsymbol{b}$ can be expressed as a first-order Taylor series:

$$\Delta\boldsymbol{A} = \sum_{i=1}^{m}(\alpha_i - \alpha_{0i})\frac{\partial\boldsymbol{A}}{\partial\alpha_i}\Big|_{\alpha_i=\alpha_{0i}}, \tag{3.12}$$

$$\Delta\boldsymbol{b} = \sum_{i=1}^{m}(\alpha_i - \alpha_{0i})\frac{\partial\boldsymbol{b}}{\partial\alpha_i}\Big|_{\alpha_i=\alpha_{0i}}, \tag{3.13}$$

where α_i is the i-th uncertain parameter and α_{0i} is its middle value. Substituting Eqs. (3.12) and (3.13) into Eq. (3.11), we have:

$$\Delta\boldsymbol{x} \approx \sum_{i=1}^{m}\boldsymbol{d}^i(\alpha_i - \alpha_{0i}), \tag{3.14}$$

where $\boldsymbol{d}^i$ is a vector such that:

$$\boldsymbol{d}^i = \boldsymbol{A}_0^{-1}(\frac{\partial\boldsymbol{b}}{\partial\alpha_i}\Big|_{\alpha_i=\alpha_{0i}} - \frac{\partial\boldsymbol{A}}{\partial\alpha_i}\Big|_{\alpha_i=\alpha_{0i}}\boldsymbol{x}_0). \tag{3.15}$$

The upper and lower bounds for Δx_j (the j-th element of $\Delta\boldsymbol{x}$) can be written as:

$$\overline{\Delta x_j} \approx \sum_{i=1}^{m} d_j^i(\alpha_i - \alpha_{0i}),\ \text{if } d_j^i \geq 0, \alpha_i = \overline{\alpha_i},\ \text{else } \alpha_i = \underline{\alpha_i}, \tag{3.16}$$

$$\underline{\Delta x_j} \approx \sum_{i=1}^{m} d_j^i(\alpha_i - \alpha_{0i}),\ \text{if } d_j^i \geq 0, \alpha_i = \underline{\alpha_i},\ \text{else } \alpha_i = \overline{\alpha_i}, \tag{3.17}$$

where d_j^i is the j-th element of $\boldsymbol{d}^i$. The interval $[\boldsymbol{x}]$ can be approximated by:

$$[\boldsymbol{x}] = \boldsymbol{x}_0 + [\Delta\boldsymbol{x}]. \tag{3.18}$$

Because it neglects higher order terms, the perturbation method cannot guarantee the result to enclose the exact response range. It works only under the assumption of

small perturbations. We can improve accuracy by keeping more terms in Eq. (3.11), for example, second-order perturbation. But this modification entails much more complex calculations. In [Gao et al., 2011] the perturbation and Monte Carlo methods were mixed to deal with the hybrid probabilistic interval problem in static reliability analysis. Because of coexistence of random variables and interval variables, the mean value and standard deviation of structural response are represented by intervals. In [Xia et al., 2013], a similar approach was used to analyse sound pressure in acoustic field in which the intervals of expectation and variance of the responses were calculated.

3.3.1.3 Optimization

When equations are not monotonic, optimisation and Monte Carlo sampling are general approaches for solving interval problems. The optimisation method finds the bounds of the responses by two optimisations to calculate the minimal and maximal responses under the condition that all variables are constrained to their corresponding intervals. The performance of optimisation method depends on two aspects [Moens and Hanss, 2011]:

- whether the actual bounds of the objective functions can be found;
- the computational efficiency to implement optimisation.

3.3.1.4 Monte Carlo sampling

The Monte Carlo sampling method takes samples from interval inputs and then obtains the corresponding deterministic responses. If the number of samplings is large enough, the responses will be close enough to the response boundaries. Since the interval inputs have no probability information, the distributions used to sample are arbitrary. In general, the uniform distribution is often chosen due to easier manipulation. If some unusual distributions are chosen, Monte Carlo Markov Chains (MCMC) can be used for drawing the values. The Monte Carlo sampling is easy to implement because all computations are deterministic. The accuracy is improved with increasing number of samplings. However, it is not computationally efficient. Moreover, the obtained boundaries are always inner bounds of the real response.

3.3.1.5 Interval finite element method

The Interval Finite Element Method (IFEM) aims at propagating interval inputs through a finite element model and obtaining the interval outputs. During assembling

the stiffness matrix in FEM, the dependence problem is significant in interval formulation. To overcome this problem, the Element-By-Element (EBE) method [Muhanna and Mullen, 2001] [Zhang, 2005] can be used for assembling the stiffness matrix. The basic idea of EBE is to detach the elements so that there are no connections between elements to avoid element coupling in the element assembly procedure [Zhang, 2005].

The interval methods presented above have been applied widely in the IFEM. In [Qiu et al., 2007], the vertex solution was extended to calculate the supremum and the infimum of displacement, stress, and strain distribution. In [Chen et al., 2002] [Chen and Yang, 2000], the perturbation method was used to obtain upper and lower bounds of static displacements. [Zhang et al., 2010] made use of iteration method to propagate interval inputs through a finite element model and obtain the interval displacements.

3.3.2 Lack-of-knowledge theory

The Lack-Of-Knowledge (LOK) theory [Puel, 2004] [Ladeveze et al., 2006b] [Louf et al., 2010] has been proposed for comparing the response of the numerical model with the real model. The LOK theory focuses on a quasi-identical structure Ω which is an assembly of substructures E ($E \in \Omega$). Let us take a static problem as an example and consider an equation defined on a substructure E:

$$\boldsymbol{K}_E \boldsymbol{U}_E = \boldsymbol{F}_E, \tag{3.19}$$

where $\boldsymbol{K}_E$ is the stiffness matrix, $\boldsymbol{F}_E$ is the force vector, $\boldsymbol{U}_E$ is the displacement vector. To illustrate the discrepancy between the numerical model and the real model, every substructure E is associated with a pair of scalar internal state variables (m_E^-, m_E^+), such that:

$$(1 - m_E^-(\boldsymbol{\theta}))\overline{\boldsymbol{K}}_E \leq \boldsymbol{K}_E(\boldsymbol{\theta}) \leq (1 + m_E^+(\boldsymbol{\theta}))\overline{\boldsymbol{K}}_E, \tag{3.20}$$

where $\boldsymbol{K}_E$ is the matrix of a real model, and $\overline{\boldsymbol{K}}_E$ is the matrix of the deterministic numerical model. The parameter $\boldsymbol{\theta}$ belongs to the space of random events. The pair of variables (m_E^-, m_E^+) which is positive is called the basic LOKs. The basic LOKs usually follow given probability distributions. The process of propagation of the basic LOKs is as follows:

- Define the basic LOKs of uncertainty inputs under given probability bounds;
- Propagate the basic LOKs throughout the numerical model;

- Obtain the effective LOKs of an output of interest $\alpha(\boldsymbol{\theta})$ under the same probability bounds as input basic LOKs:

$$\Delta\alpha^{-}(\boldsymbol{\theta}) \leq \alpha(\boldsymbol{\theta}) - \overline{\alpha} \leq \Delta\alpha^{+}(\boldsymbol{\theta}), \tag{3.21}$$

  where $\alpha(\boldsymbol{\theta})$ is the real outputs (e.g displacement, stress, or strain), and $\overline{\alpha}$ is the numerical outputs, the pair $(\Delta\alpha^{-}(\boldsymbol{\theta}), \alpha^{+}(\boldsymbol{\theta}))$ are the effective output LOKs.

3.3.3 Fuzzy set theory

Fuzzy set theory, which in some way extends interval theory, was proposed in [Zadeh, 1965]. The membership function of a fuzzy set associates each $x \in X$ with a real number in the interval $[0, 1]$:

$$\mu_A(x) : X \to [0, 1]. \tag{3.22}$$

The value of $\mu_A(x)$ is the degree of membership of x in fuzzy set A. The definition gives us a fuzzy logic: the nearer the value of $\mu_A(x)$ is to 1, the higher grade of membership of x in A is. In this case, we have a graded possibility from true (1) to false (0). [Couso and Sánchez, 2011] gave three interpretations of fuzzy sets:

- linguistic variables;
- ill-known or incomplete knowledge;
- conditional possibility measure.

In [Wehrle et al., 2011], different types of membership function of fuzzy sets have been studied, including single membership function, interval membership function, triangular membership function, trapezoidal membership function, and empirical membership function, etc. The empirical membership function can be created from histograms with the help of polynomial regression.

Fuzzy numerical operations can be performed using interval arithmetic operations applied to each ω-level cut. So the problems in interval analysis, for example, overestimation and computational difficulty, exist in fuzzy operations. The transformation method was introduced as a systemic discretization method for fuzzy uncertainty in [Hanss, 2002]. The transformation method has two forms: general transformation method and reduced transformation method. Based on the transformation method, an approach of inverse fuzzy arithmetic was introduced in [Hanss, 2003a] and [Haag and Hanss, 2012]. In [Chen and Rao, 1997], Taguchi's robust philosophy was used to reduce computation time in fuzzy operations.

The Fuzzy Finite Element Analysis (FFEA) focuses on propagating the fuzzy-valued inputs through finite element models to obtain the fuzzy-valued outputs. The steps of FFEA [Moens and Hanss, 2011] [Akpan et al., 2001] [Chen and Rao, 1997] are:

1. discretize fuzzy-valued inputs using ω-level cuts;
2. apply interval finite methods to propagates the interval inputs through the finite element model and obtain the interval outputs;
3. apply Zadeh's extension principle to assemble interval outputs to fuzzy-valued outputs.

Considering the complexity and monotonicity of finite element models, many strategies focus on the second steps, interval propagation. In [Akpan et al., 2001], the vertex method was used to implement interval propagation. In [Chen and Rao, 1997], a modified Taguchi-oriented approach was used to propagate fuzzy variables. In [Hanss, 2003b], the extended transformation method was proposed for the non-monotonic finite element models by adding more observation points to the search domain. Compared with the extended transformation method, the reduced transformation method [Moens and Hanss, 2011] [Hanss, 1999] is efficient to reduce computation for a monotonic finite element model. Within the fuzzy finite elements model, an interdependency index was introduced to quantify the interdependence between fuzzy-valued outputs [Giannini and Hanss, 2008].

3.3.4 Possibility theory

Possibility theory is relevant to represent imprecise knowledge [Dubois et al., 2000]. Possibility theory starts from possibility distributions which contain equivalent information with fuzzy sets. A possibility distribution is also a mapping π from some variables $x \in X$ to the unit interval:

$$\pi : X \to [0, 1]. \tag{3.23}$$

Similar to a fuzzy set, a possibility distribution describes the more or less plausible values of some uncertainty variables [Baudrit and Dubois, 2006]. The value $\pi(x) = 1$ means x is the most plausible value; the value $\pi(x) = 0$ means x is the least plausible value. If a possibility distribution π in $\mathbb{R}^m$ satisfies the relationship:

$$\max_{x_j \in \mathbb{R}, j \neq i} \pi(x_1, ..., x_j, ..., x_m) = \pi_i(x_i), \quad x_i \in \mathbb{R}, \quad i = 1, \cdots, m, \tag{3.24}$$

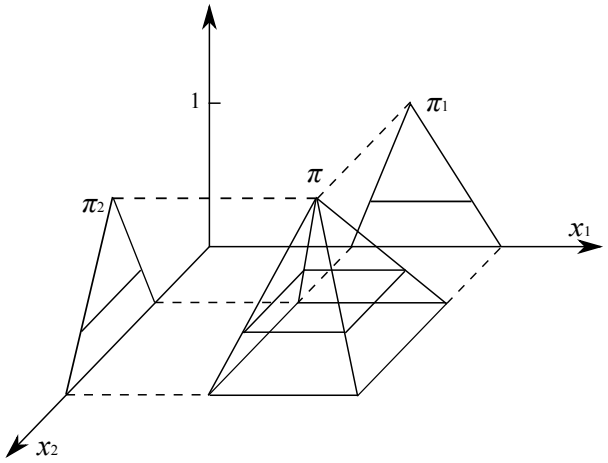

Fig. 3.1 Non-interactive possibility distribution

then π is a joint possibility and π_i is the i-th marginal possibility distribution of π. If a joint possibility distribution π satisfies:

$$\pi(x_1, ..., x_m) = \min\{\pi_1(x_1), ..., \pi_m(x_m)\}, \quad x_i \in \mathbb{R}, \quad i = 1, \cdots, m, \tag{3.25}$$

the marginal possibility distributions π_i are said to be non-interactive. Fig. 3.1 is a non-interactive joint possibility distribution in $\mathbb{R}^2$. In [Fullér and Majlender, 2004], the interaction of a joint possibility distribution was investigated, and a quantity to describe the degree of interaction was proposed.

Associated to a possibility distribution, there are two normalized functions, possibility Π and necessity N, such that:

$$\Pi(A) = \sup_{x \in A} \pi(x), \quad \forall A \subseteq X, \tag{3.26}$$

and

$$N(A) = 1 - \Pi(\overline{A}) = \inf_{x \notin A} (1 - \pi(x)), \quad \forall A \subseteq X. \tag{3.27}$$

The degree of possibility $\Pi(A)$ and the degree of necessity $N(A)$ jointly describe the uncertainty in the proposition that the value x lies within a certain subset A.

3.3.5 Probability box

Let $\mathcal{P}$ be a set of probability measures on some space Ω. The definition of upper and lower probability can be written respectively as follows [Baudrit and Dubois, 2006]:

$$\overline{P}(A) = \sup_{P \in \mathcal{P}} P(A), \quad \forall A \subseteq \Omega, \tag{3.28}$$

$$\underline{P}(A) = \inf_{P \in \mathcal{P}} P(A), \quad \forall A \subseteq \Omega. \tag{3.29}$$

A probability box or p-box [Ferson et al., 2003] can be induced from lower and upper probability, such that:

$$\underline{F}(x) = \underline{P}((-\infty, x]), \quad \forall x \in \mathbb{R}, \tag{3.30}$$

$$\overline{F}(x) = \overline{P}((-\infty, x]), \quad \forall x \in \mathbb{R}. \tag{3.31}$$

The interval $[\underline{F}, \overline{F}]$ is called a probability box. Both $\underline{F}$ and $\overline{F}$ are non-decreasing functions. A probability box $[\underline{F}, \overline{F}]$ provides the left and right bounds of a cumulative probability distribution, such that

$$\underline{F}(x) \leq F(x) \leq \overline{F}(x), \quad \forall x \in \mathbb{R}, \tag{3.32}$$

where F denotes a cumulative probability function. The gap between $\underline{F}$ and $\overline{F}$ reflects the incomplete nature of the knowledge. The probability box offers a useful tool to do risk analysis on the conditions that:

- the parameters (mean, variance) of probabilistic models are imprecise (e.g., lie in an interval);
- the probabilistic models rely on imprecise statistics (e.g., set-valued).

3.3.6 Random set theory

Random set theory serves for the random experiments with set-valued observations. It is an extension of probability theory to set-valued rather than point valued mappings. Consider a probability space $(\Omega, \sigma_\Omega, \mathcal{P})$ and let Θ be a finite set. A finite random set [Nguyen, 2006] with values in 2^Θ is a mapping: $X : \Omega \to 2^\Theta$ verifying some measurability conditions. The random set theory provides a mathematical model which can handle both aleatory and epistemic uncertainty.

Random set theory has been widely used in mechanical calculations. In [Nasekhian and Schweiger, 2011], random sets were propagated through a finite elements model

and the uncertainty of response was evaluated. In [Tonon, 2004], random set theory was used to analysis the steady-state magnification factor of a linear mass-spring-damper system considering imprecise and dissonant information. In [Zhang, 2012], random sets were induced from the discretization of several p-boxes to do the structural reliability assessment. In [Tonon et al., 1999] and [Tonon et al., 2006], random sets were directly constructed from expert opinions to analyse aircraft crash reasons and reliability bounds.

3.3.7 Theory of belief functions

The theory of belief functions is a general framework allowing us to treat imprecise information. It comes from evidence theory introduced by [Shafer, 1976] in which it was used to handle uncertainty from evidence.

3.3.7.1 Definition

Let Θ be a finite frame of discernment, a Basic Probability Assignment (BPA) can be defined as a mapping $m : 2^{\Theta} \rightarrow [0, 1]$ that must verify two conditions:

$$m(\emptyset) = 0, \tag{3.33}$$

$$\sum_{A \subseteq \Theta} m(A) = 1. \tag{3.34}$$

Any subset A of Θ such that $m(A) > 0$ is called a focal element of m. The value $m(A)$ represents the degree of belief (or confidence) attached exactly to the proposition $\theta \in A$. The belief and plausibility functions induced by m are defined as follows:

$$Bel(A) = \sum_{B \subseteq A} m(B), \quad \forall A \subseteq \Theta, \tag{3.35}$$

$$Pl(A) = \sum_{B \bigcap A \neq \emptyset} m(B), \quad \forall A \subseteq \Theta. \tag{3.36}$$

The quantity $Bel(A)$ is the degree that the evidence supports the proposition $\theta \in A$. $Pl(A)$ is the degree to which the evidence is not contradictory with the proposition $\theta \in A$. The difference between $Bel(A)$ and $Pl(A)$ corresponds the degree of ignorance. It is easy to show that:

$$Pl(A) \geq Bel(A), \tag{3.37}$$

$$Pl(A) = 1 - Bel(\overline{A}). \tag{3.38}$$

Specially, the restriction of the plausibility function to singletons is called the contour function:

$$pl(\theta) = Pl(\{\theta\}), \quad \theta \in \Theta. \tag{3.39}$$

In [Denœux, 2014], the contour function was used to infer the parameter uncertainty from observations based on likelihood-based belief functions.

3.3.7.2 Information merging

Information merging is a necessary step in uncertainty management and identification. Considering two sources which generate two BPA m_1 and m_2 in the set Θ, there exist several combination rules in the theory of belief functions. Here, three most common used combination rules are introduced.

Dempster's rule

If both sources are reliable and independent, then the induced mass functions m_1 and m_2 can be combined by Dempster's rule:

$$m_{12} = (m_1 \oplus m_2)(A) = \frac{1}{1-k} \sum_{B \bigcap C = A} m_1(B) m_2(C), \quad \forall A \subseteq \Theta, A \neq \emptyset, \tag{3.40}$$

where

$$k = \sum_{B \bigcap C = \emptyset} m_1(B) m_2(C)$$

is the degree of conflict between m_1 and m_2. The degree of conflict is an important by-product of Dempster's rule. It can be used to normalise the combined BPA and to assess the compatibility of two sources. In the real world, when combining two sources of information, we may have two kinds of effect. On the one hand, there is a potential benefit of using the right information to correct the wrong information. On the other hand, there is a risk of using wrong information to impact correct information. The degree of conflict makes it possible to indicate the risk of influence by wrong information. Two incompatible sources often imply that at least one source is not reliable.

Disjunctive rule

If we only know that at least one source contains some true information, we can use the disjunctive rule to do combination:

$$(m_1 \cup m_2)(A) = \sum_{B \cup C = A} m_1(B) m_2(C), \quad \forall A \subseteq \Theta, A \neq \emptyset. \tag{3.41}$$

This operation is commutative and associative. It never generates conflict so that no normalisation has to be performed. This rule can be used in case of heavy conflict between the different pieces of evidence.

Intermediate rule

There is an intermediate rule between disjunctive rule and Dempster's rule proposed by [Dubois and Prade, 1986]:

$$(m_1 * m_2)(A) = \sum_{B \cap C = A} m_1(B) m_2(C) + \sum_{B \cap C = \emptyset, B \cup C = A} m_1(B) m_2(C), \tag{3.42}$$

for any $A \subseteq \Theta, A \neq \emptyset$ and $(m_1 * m_2)(\emptyset) = 0$. We can also see that no normalization has to be performed with this rule.

3.3.8 Relation of the representation methods

The representation methods introduced in this section are the commonly used frameworks to treat the imprecise and random nature of information. There are some links among probability, fuzzy set theory, possibility theory, probability box, random set theory, and theory of belief functions.

The function μ_A in fuzzy set theory and the distribution π in possibility theory contains equivalent information. Thus, the two theories are considered as interchangeable. Moreover, a possibility distribution can be seen as a particular case of belief function theory where the focal elements are nested. In this case, $Pl = \Pi$ and $Bel = N$ [Baudrit and Dubois, 2006].

The functions Pl and Bel in belief function theory can be seen as upper and lower probabilities. They can induce a probability box $[\underline{F}, \overline{F}]$. A probability box can thus be regarded as a particular case of belief function.

The theory of belief functions and random set theory are mathematically equivalent [Nguyen, 1978] [Nguyen, 2006]. They only hold different interpretations: focal elements in the theory of belief functions are subsets induced by evidence, while the random

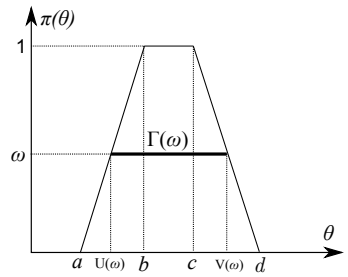

Fig. 3.2 Possibility distribution

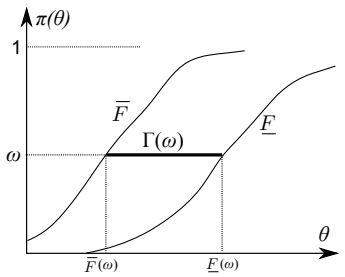

Fig. 3.3 p-box

sets are viewed as the outcomes of random experiments [Ben Abdallah et al., 2014]. Considering the strong relationship, in this thesis, we don't take apart between them.

The random sets can be induced from possibility distributions [Ben Abdallah et al., 2014] [Bellenfant et al., 2009], and p-boxes [Zhang, 2012] [Tonon, 2004] with the help of the ω-level cuts. Considering $\Omega = [0, 1]$ and a possibility distribution π as shown in Fig. 3.2, the ω-level cut to a possibility distribution can be written as:

$$\Gamma(\omega) = \{\theta \in \mathbb{R} | \pi(\theta) \geq \omega\}, \forall \omega \in \Omega. \tag{3.43}$$

The mapping Γ defined in Eq. (3.43) is the random set induced by the possibility distribution π. Similarly, Fig. 3.3 shows the random set induced by the p-box $(\underline{F}, \overline{F})$:

$$\Gamma(\omega) = \{\theta \in \mathbb{R} | \overline{F}(\theta) \geq \omega \text{ and } \underline{F}(\theta) \leq \omega\}, \forall \omega \in \Omega, \tag{3.44}$$

where $\Omega = [0, 1]$.

The theory of belief functions is an extension of probability theory. When all focal elements are singletons, the indicators Pl and Bel are both probability measures, and that is $Bel = P = Pl$.

3.4 Conclusion

In this chapter, probabilistic and non-probabilistic representations have been presented. Bayesian inference, a probabilistic approach, can identify material parameters and quantify their uncertainty. However, few studies address material identification problems based on non-probabilistic approaches. A more general framework should be proposed to quantify the heterogeneous uncertainties in identification problems. The theory of belief functions has clear advantages for handling uncertainty quantification. Firstly, it offers complete tools to encode all kind of available information. On the

one hand, the theory of belief functions allows us to represent subjective uncertainty and incomplete information; on the other hand, it can be seen as a generalisation of probability theory. Therefore, both aleatory and epistemic uncertainty can be represented in the belief functions framework. Secondly, it includes various information merging mechanisms which are suitable for practical scenarios. Thirdly, multiple representations, such as Bel, Pl, and pl can be used to quantify uncertain results. Therefore, we will apply belief function theory to manage uncertainty in identification problems in this thesis.

Chapter 4

Mechanical model and Identification framework

In this thesis, we focus on the identification of complex materials from full-field displacement measurement taking into account uncertainty. In Chapter 2, we have introduced several full-field measurement techniques, among which DIC is a widely used technique due to its relative simplicity and excellent adaptation for analysing the mechanical properties of complex materials. In this work, the full-field displacement measurement is assumed to be obtained using DIC from CCD camera images. The parameter identification is based on parametrized mechanical models. Thus, the mechanical models used in this study will be introduced in this chapter. Moreover, the general framework for the identification of parameters and quantification of heterogeneous uncertainties will be presented as well.

4.1 Mechanical model

In this section, we first introduce the equations of continuous mechanics that describe the experiments. Then, the Finite Element Method (FEM) is briefly introduced and the particular case of multi-scale modelling. The latter will be studied in terms of identification in Chapter 5.

4.1.1 Continuous equations describing the experiment

Solid mechanics defines the behaviour of solid materials, e.g., motion and deformation under external or internal loadings. Mechanical models normally contain the quantities characterizing mechanical systems (e.g., geometry, loadings, mechanical property

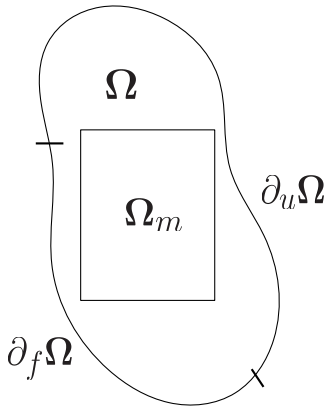

Fig. 4.1 Mechanical model for identification

including elasticity, elastoplasticity, viscoplasticity, damping, etc.) and their relations. In this thesis, we aim at the identification of elastic material properties. Thus, we only introduce the elastic mechanical model. Let us consider the solid structure as shown in Fig. 4.1, which is defined as a 2D domain Ω. The model equations that govern the behaviour of structures are particularised as follows:

- on Ω:

$$\text{Equilibrium:} \quad \text{div}\boldsymbol{\sigma} = \mathbf{0}, \tag{4.1}$$

$$\text{Kinematic compatibility:} \quad \boldsymbol{\varepsilon} = \frac{1}{2}(\nabla \boldsymbol{u} + \nabla^T \boldsymbol{u}), \tag{4.2}$$

$$\text{Constitutive equation:} \quad \boldsymbol{\sigma} = \boldsymbol{C}(\boldsymbol{\theta})\boldsymbol{\varepsilon}, \tag{4.3}$$

  where $\boldsymbol{u}$ is the displacement field, $\boldsymbol{\varepsilon}$ is the strain field, $\boldsymbol{\sigma}$ is the stress field, $\boldsymbol{C}(\boldsymbol{\theta})$ is the elastic tensor field which can be described thanks to the parameters $\boldsymbol{\theta}$ determining the elastic properties;

- on $\partial_u\Omega$: $\boldsymbol{u} = \boldsymbol{u}_d$, where $\boldsymbol{u}_d$ is a known Dirichlet boundary condition;

- on $\partial_f\Omega$: $\boldsymbol{\sigma} \cdot \boldsymbol{n} = \boldsymbol{f}_s$, where $\boldsymbol{f}_s$ is a known Neumann boundary condition, and we will assume in the following that $\partial_u\Omega \cup \partial_f\Omega = \partial\Omega$ and $\partial_u\Omega \cap \partial_f\Omega = \emptyset$;

- on Ω_m: $\boldsymbol{u} = \widetilde{\boldsymbol{u}}$, where $\widetilde{\boldsymbol{u}}$ is the displacement related to the DIC measurement on a sub-domain $\Omega_m \subset \Omega$.

From Eqs. (4.1) to (4.3) and the boundary conditions on $\partial_u\Omega$ and $\partial_f\Omega$, a well-posed direct problem can be defined. Its solution is denoted:

$$\boldsymbol{u} = \boldsymbol{u}(\boldsymbol{\theta}). \tag{4.4}$$

The comparison of $\boldsymbol{u}(\boldsymbol{\theta})$ with $\widetilde{\boldsymbol{u}}$ on Ω_m gives some information on $\boldsymbol{\theta}$ and will be used to perform the identification.

4.1.2 Finite Element Method

The Finite Element Method (FEM) is based on the discretization of Eq. (4.1). The weak form of Eq. (4.1) can be written as follows:

$$W_* = \int_\Omega \boldsymbol{u}_* \cdot div(\boldsymbol{\sigma}) \mathrm{d}\Omega = 0, \quad \forall \boldsymbol{u}_* \in H_0^1(\Omega), \tag{4.5}$$

where $\boldsymbol{u}_*$ denotes a virtual displacement field, $H_0^1(\Omega)$ is a Hilbert space, $\boldsymbol{\sigma}$ is the stress field which can be written in vector form (2D case):

$$\boldsymbol{\sigma} = (\sigma_{11}, \sigma_{22}, \sigma_{12})^T.$$

The strain field in the 2D case can be written as:

$$\boldsymbol{\varepsilon} = (\varepsilon_{11}, \varepsilon_{22}, \varepsilon_{12})^T.$$

Correspondingly, the elastic tensor $\boldsymbol{C}(\boldsymbol{\theta})$ in the 2D case is a 3×3 matrix. By applying the partial integral equation, we can transform it into the following form:

$$W_* = -\int_\Omega \boldsymbol{\varepsilon}_* \cdot \boldsymbol{\sigma} d\Omega + \int_{\partial_f \Omega} \boldsymbol{u}_* \cdot \boldsymbol{\sigma} \cdot \boldsymbol{n} \mathrm{d}S = 0, \quad \forall \boldsymbol{u}_* \in H_0^1(\Omega), \tag{4.6}$$

where $\boldsymbol{\varepsilon}_*$ is the virtual strain field associated with the virtual displacement field $\boldsymbol{u}_*$. Then Eqs. (4.2) and (4.3) are taken into account to have a weak form in terms of displacements. Considering $\boldsymbol{u}_*$ is null on $\partial_u \Omega$ and considering the Neumann boundary condition, the boundary terms is written as follows:

$$\int_{\partial\Omega} \boldsymbol{u}_* \cdot \boldsymbol{\sigma} \cdot \boldsymbol{n} \mathrm{d}S = \int_{\partial_f \Omega} \boldsymbol{u}_* \cdot \boldsymbol{f}_s \mathrm{d}S. \tag{4.7}$$

To discretize Eq. (4.6), the division of the domain (called meshing) into elementary polyhedrons (called finite elements) should be done firstly. Then the weak form can be discretized and appears as a sum of elementary terms

$$W_* = \sum_{e=1}^{nelt} \left(W_\Omega^e - W_{BC}^e \right) = 0, \tag{4.8}$$

with

$$W_{\Omega}^{e} = \int_{\Omega^e} \boldsymbol{\varepsilon}_* \cdot \boldsymbol{C}(\boldsymbol{\theta}) \cdot \boldsymbol{\varepsilon} \mathrm{d}\Omega, \tag{4.9}$$

$$W_{BC}^{e} = \int_{\partial\Omega^e} \boldsymbol{u}_* \cdot \boldsymbol{f}_s \mathrm{d}S, \tag{4.10}$$

where Ω is the integral domain, BC corresponds to the boundary conditions, Ω^e is the domain of finite element ($\Omega^e \subset \Omega$), $\partial\Omega^e$ is the boundary of Ω, if any, which locates on the considered finite element. The number $nelt$ is the number of finite elements making up the mesh. The displacement fields of each element are represented by the displacements in each node and corresponding approximation:

$$\boldsymbol{u}(\boldsymbol{x}) = \sum_{i=1}^{N_d} N_i(\boldsymbol{x}) u_i, \tag{4.11}$$

where u_i is the displacement of the node i, $N_i(\boldsymbol{x})$ is the shape function corresponding the node i. The shape functions depend only on the coordinates of the element nodes. Substituting Eq. (4.11) into Eq. (4.8), we can transform the weak form into the following discrete matrix form:

$$W_* = \mathop{\mathcal{A}}_{e=1}^{nelt} (\boldsymbol{U}_*^e)^T (\boldsymbol{K}^e \boldsymbol{U}^e - \boldsymbol{F}^e) = 0, \quad \forall \boldsymbol{U}_*^e, \tag{4.12}$$

where the symbol $\mathcal{A}$ is the operator that assembles the elementary matrices into a global matrix. The vector $\boldsymbol{U}_*^e$ collects the nodal components of the virtual displacement, $\boldsymbol{F}^e$ is the nodal force vector. The matrix $\boldsymbol{K}^e$ is the elementary matrix and can be written as follows (for T3 elements with linear shape functions):

$$\boldsymbol{K}^e = V^e \boldsymbol{B}^{eT} \boldsymbol{C}^e \boldsymbol{B}^e, \tag{4.13}$$

where V^e is the elementary surface (volume), $\boldsymbol{B}^e$ is the gradient matrix only associated with the nodal coordinates, $\boldsymbol{C}^e$ is the matrix associated the material properties. Because $\boldsymbol{u}_*$ is totally independent from actual displacements, we can write Eq. (4.12) as follows:

$$\mathop{\mathcal{A}}_{e=1}^{nelt} (\boldsymbol{K}^e \boldsymbol{U}^e - \boldsymbol{F}^e) = \boldsymbol{0}. \tag{4.14}$$

Assembling the elementary local matrices and vectors, we can obtain a global system matrix equation:

$$\boldsymbol{KU} = \boldsymbol{F}, \tag{4.15}$$

where $\boldsymbol{K}$ is the stiffness matrix with $2n \times 2n$ size, $\boldsymbol{U}$ is the vector of displacement with size $2n \times 1$ and $\boldsymbol{F}$ is the vector of outsides force with size $2n \times 1$. The value n is the number of nodes. Under the linear assumption, the nodal displacements can be solved by inverting the system in Eq. (4.15). If the linear assumption is not satisfied, such as in the elastoplastic or elastoviscoplastic problems, linearisation is necessary to approximate the responses.

4.1.3 Multi-structural model and homogenization scheme

In Section 4.1.2, we presented the general mechanical model and its numerical implementation methods. Composite materials, which belong to multi-structure materials need to be paid special attention because of their special properties. Therefore, multi-structural models [Ladevèze and Nouy, 2003] [Kanouté et al., 2009] were proposed to do high quality prediction and identification. For the multi-structural models, macro-scale constitutive behaviour strongly depends on the topology and properties of micro-structures. However, the micro-structures are usually geometrically complex and heterogeneous. Considering the computational effort, analysing large structures on a micro-structural level is an intractable problem. Therefore, the term Representative Volume Element (RVE), as shown in Fig. 4.2, was proposed to approximate multi-structural mechanics [Hill, 1963] [Hashin, 1983]. The micro-structures are normally heterogeneous, and a local analysis is needed to determine the effective or average elastic properties of the RVE. Then, the properties of the RVE are replaced by its effective properties. Considering the RVE's diversity, an idea for modelling RVE is

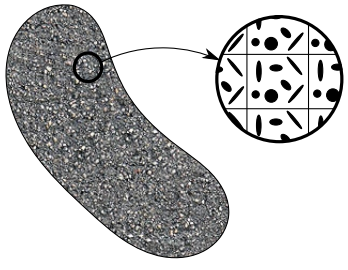

Fig. 4.2 Illustration of RVE

to describe the real micro-structures by several statistical factors. The statistical factors are exacted from experimental observations, such as Electron Back-scatter

Fig. 4.3 Statistical description of RVE

diffraction, X-ray and neutron diffraction method, and so on. In this thesis, we apply a synthetic micro-structure generator tool developed in [Tschopp et al., 2008] to generate synthetic RVEs. The computer-generated 2D dual-phase periodic micro-structure contains ellipsoidal particles characterised by three factors:

- the area fraction, $A_f = V_p/V$, with V_p the volume occupied by the ellipsoidal particles and V the total volume of the RVE;
- the aspect ratio, $A_r = a/b$, with a the semi-major axis and b the semi-minor axis;
- the degree of alignment: axes orientation is random, perfectly aligned, or semi-aligned, denoting D_a as the orientation degree of ellipsoid, random orientation: $D_a \sim \mathcal{U}([0°, 180°])$, perfect aligned orientation: $D_a = Constant$, semi-aligned orientation: $D_a \sim \mathcal{N}(\mu_{Da}, \sigma^2_{Da})$.

The configurations, as shown in Fig. 4.3, are a set of synthetic RVEs generated under $A_f = 45\%$, $A_r = 1.92$, and semi-aligned degree characterized by a Gaussian distribution $\mathcal{N}(0°, (10°)^2)$.

Considering the diversity of micro-structure types, there are many other selections of statistical characterization factors, such as mean edge length [Kumar and Kurtz, 1995], k-nearest neighbor distance [Holmes and Adams, 2002] and pore clustering [Bilger et al., 2005]. Some overviews have been given by [Ohser and Mücklich, 2000] [Fritzen, 2011] [Torquato, 2013] .

An RVE gives a model to describe the micro-structures. Homogenization provides an approach to approximate the multi-structural constitutive behaviour. In this thesis, we apply an energy-based homogenization approach, in which the effective elastic properties should make the strain energy of same size homogeneous material equal to that of its corresponding RVE. The standard homogenization approach is to analyse the RVE using either uniform traction or uniform displacement boundary conditions [Hollister and Kikuchi, 1992]. These boundary conditions are applied to the RVE so as to produce unit strains or stresses within the RVE as shown in Fig. 4.4. Taking unit

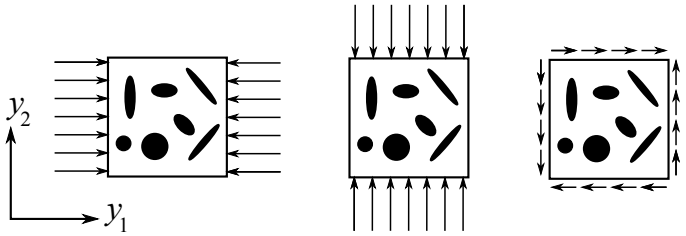

Fig. 4.4 Uniform boundary conditions applied to RVE

strains in the 2D case as an example, the average strains can be chosen as:

$$\boldsymbol{\varepsilon}^{11} = (1,0,0)^T, \quad \boldsymbol{\varepsilon}^{22} = (0,1,0)^T, \quad \boldsymbol{\varepsilon}^{12} = (0,0,1)^T. \tag{4.16}$$

The homogenized elastic tensor (determines the effective elastic properties of the RVE) is given as follows [Sigmund, 1994] [Xia and Breitkopf, 2015]:

$${}^hC_{ijkl} = \frac{1}{V}\int_\Omega C_{pqrs}\varepsilon_{pq}^{(ij)}\varepsilon_{rs}^{(kl)}\mathrm{d}\Omega, \tag{4.17}$$

where $\varepsilon_{pq}^{(ij)}$ (called the superimposed strain field) is the component of the strain tensor corresponding the test under average strain $\boldsymbol{\varepsilon}^{ij}$, Ω is the domain of the RVE, V is the volume of the RVE. Some more details about energy-based homogenization are introduced in [Hashin, 1983] [Sigmund, 1994] [Xia and Breitkopf, 2015].

Following the asymptotic homogenization, when the aspect ratio between the macro and micro scales is much smaller than 1, the dependence on local microscopic variables can be considered periodic for a fixed macroscopic point [Xia and Breitkopf, 2015]. In [Andreassen and Andreasen, 2014], the homogenization method applied periodic boundary conditions to an RVE when the aspect ratio was much smaller than 1. Under the assumption of periodicity, the displacement field of the RVE cell subjected to a given strain ε_{ij}^0 can be written as the sum of a microscopic displacement field and a periodic fluctuation field u_i^* [Michel et al., 1999]:

$$u_i = \varepsilon_{ij}^0 y_j + u_i^*. \tag{4.18}$$

Because of the unknown periodic fluctuation term u_i^*, Eq. (4.18) cannot be directly imposed on boundaries. It needs to be transformed into a certain number of explicit constraints between the corresponding pairs of nodes on the opposite surfaces of the

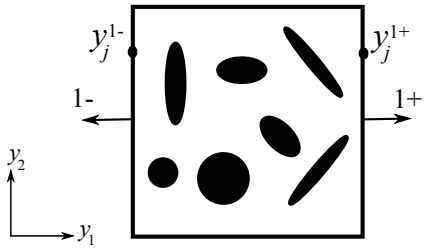

Fig. 4.5 Uniform boundary conditions applied to RVE

RVE [Xia et al., 2003]:

$$\begin{cases} u_i^{k+} = \varepsilon_{ij}^0 y_j^{k+} + u_i^*, \\ u_i^{k-} = \varepsilon_{ij}^0 y_j^{k-} + u_i^*. \end{cases} \tag{4.19}$$

The periodic u_i^* can be eliminated through the difference between the displacement:

$$u_i^{k+} - u_i^{k-} = \varepsilon_{ij}^0 (y_j^{k+} - y_j^{k-}) = w_i, \tag{4.20}$$

where superscripts "$k+$" and "$k-$" denote the pair of two opposite parallel boundary surfaces that are oriented perpendicular to the k-th direction ($k = 1, 2$ in the 2D case). Fig. 4.5 shows the 2D RVE case. The values y_j^{k+} and y_j^{k-} are the microscopic coordinates of corresponding pairs of nodes. When the RVE is a parallelepiped, the differences between y_j^{k+} and y_j^{k-} are constant.

In [Xia and Breitkopf, 2015], the finite element solution under periodic boundary conditions was presented. The displacement vector $\boldsymbol{U}$ is decomposed into four parts: $\overline{\boldsymbol{U}}_1$ denotes the given displacement; $\boldsymbol{U}_2$ denotes the displacement corresponding to the interior nodes; $\boldsymbol{U}_3$ and $\boldsymbol{U}_4$ denote the displacement corresponding to the opposite boundary nodes. They satisfy:

$$\boldsymbol{U}_4 = \boldsymbol{U}_3 + \boldsymbol{W}, \tag{4.21}$$

where $\boldsymbol{W}$ is obtained from Eq. (4.20). The equilibrium equation can be expanded to

$$\begin{bmatrix} \boldsymbol{K}_{11} & \boldsymbol{K}_{12} & \boldsymbol{K}_{13} & \boldsymbol{K}_{14} \\ \boldsymbol{K}_{21} & \boldsymbol{K}_{22} & \boldsymbol{K}_{23} & \boldsymbol{K}_{24} \\ \boldsymbol{K}_{31} & \boldsymbol{K}_{32} & \boldsymbol{K}_{33} & \boldsymbol{K}_{34} \\ \boldsymbol{K}_{41} & \boldsymbol{K}_{42} & \boldsymbol{K}_{43} & \boldsymbol{K}_{244} \end{bmatrix} \begin{bmatrix} \boldsymbol{U}_1 \\ \boldsymbol{U}_2 \\ \boldsymbol{U}_3 \\ \boldsymbol{U}_4 \end{bmatrix} = \begin{bmatrix} \boldsymbol{F}_1 \\ \boldsymbol{F}_2 \\ \boldsymbol{F}_3 \\ \boldsymbol{F}_4 \end{bmatrix}, \tag{4.22}$$

where $\boldsymbol{F}_2 = \mathbf{0}$, and $\boldsymbol{F}_3 + \boldsymbol{F}_4 = \mathbf{0}$ due to periodicity assumption. Then the equation above reduces to:

$$\begin{bmatrix} \boldsymbol{K}_{122} & \boldsymbol{K}_{23} + \boldsymbol{K}_{24} \\ sym. & \boldsymbol{K}_{33} + \boldsymbol{K}_{34} + \boldsymbol{K}_{43} + \boldsymbol{K}_{44} \end{bmatrix} \begin{bmatrix} \boldsymbol{U}_2 \\ \boldsymbol{U}_3 \end{bmatrix} = - \begin{bmatrix} \boldsymbol{K}_{21} \\ \boldsymbol{K}_{31} + \boldsymbol{K}_{41} \end{bmatrix} \overline{\boldsymbol{U}}_1 - \begin{bmatrix} \boldsymbol{K}_{24} \\ \boldsymbol{K}_{34} + \boldsymbol{K}_{44} \end{bmatrix} \boldsymbol{W}. \tag{4.23}$$

4.1.4 Multi-level Finite element method

The combination of homogenization and FEM yields the multilevel Finite Element Method (FE^2M) [Feyel and Chaboche, 2000] [Schmidt et al., 2015]. The FE^2M model can be separated into three steps:

1. localisation of RVE macroscopic strain state ε_M to obtain the microscopic stress field ε_m;

2. finite element computation of the RVE under periodic boundary conditions;

3. homogenisation of microscopic stress field σ_m to obtain RVE macroscopic stress state σ_M.

For non-linear models, the Newton-Raphson method can be used to implement the FE^2M scheme. For linear models, the homogenization step can be done firstly to get the effective elastic tensors at macroscopic nodes.

Both mono-structural and multi-structural model apply mathematical point of view to explain the real systems. During this process, simplification and approximation are necessary due to variety and complexity of the real world. For example, the complex micro-structure elastic properties are approximated by the simple homogenised elastic tensors in the multi-structure model presented above. In addition, with the development of computer technology, the majority of complex models are solved by numerical methods (e.g. FEM). Computational implementations inevitably induce numerical errors. Thus, there is always a discrepancy between predicted values and real responses. This kind of uncertainty is called model uncertainty. Similar to measurement uncertainty, the model uncertainty should also be considered and quantified for identification problems. However, model uncertainty mainly arises from incomplete information about the real world, and it is more epistemic than aleatory. Therefore, we need to develop specific identification approaches to model uncertainty representation and propagation.

4.2 Prior information and inference challenge

It is often beneficial to formulate and exploit available prior information in addition to experimental and theoretical information. Nevertheless, prior information is also uncertain. It may come from early experiment results and conclusion, conjecture from similar systems, or expert opinions. This information is often vague, non-specific and dissonant. Its uncertainty is complex, various and non-uniform due to its multiple sources. Similar to model uncertainty, prior information uncertainty is essentially epistemic. The non-probabilistic approaches introduced in Chapter 3 can be used to represent prior information uncertainty in different scenarios. Considering prior information uncertainty and its description methods, it is necessary to develop an integrated strategy to describe all uncertainties and then propagate them within a unified framework. Meanwhile, the framework should also be compatible with measurement and model uncertainties. In summary, we face the following four challenges:

- translation of available information (theoretical, experimental, empirical information) into a mathematical language;
- aggregation of information from multiple sources into a single framework (information merging);
- propagation (efficient enough with acceptable accuracy) of uncertain inputs through the models to compute the uncertain outputs;
- exploitation and interpretation of uncertain analysis results.

These challenges can be overcome by the introduction of the theory of belief functions, which constitutes a general framework to represent and quantify the heterogeneous uncertainties. In the next section, an identification framework using likelihood-based belief functions will be presented.

4.3 Identification framework using likelihood-based belief functions

4.3.1 General framework and identification key-points

Consider the solid structure as shown in Fig. 4.1, and its constitutive behaviour described by Eqs. from (4.1) to (4.3) with boundary conditions. As mentioned in

Section 4.1.1, a direct problem can be constructed for this set of equations and its solution is denoted:

$$\boldsymbol{u} = \boldsymbol{u}(\boldsymbol{\theta}). \tag{4.24}$$

The relation between measured values $\widetilde{\boldsymbol{u}}$ and predicted values $\boldsymbol{u}$ can be written as follows:

$$\widetilde{\boldsymbol{u}} = \boldsymbol{u} + \boldsymbol{e}_{meas} + \boldsymbol{e}_{model}, \tag{4.25}$$

where $\boldsymbol{e}_{meas}$ denotes the measurement error and $\boldsymbol{e}_{model}$ denotes the model error. The Bayesian inference is a reference approach to manage uncertainties, when identifying $\boldsymbol{\theta}$ from Eqs. (4.24) and (4.25). Its main assumption is that $\boldsymbol{e}_{meas}$ and $\boldsymbol{e}_{model}$ can be described with probabilities, for example $P_{\boldsymbol{e}}(\boldsymbol{e}_{meas} + \boldsymbol{e}_{model})$, if both errors are dealt with together. It allows us to define the likelihood function:

$$L(\boldsymbol{\theta}; \widetilde{\boldsymbol{u}}) = p(\widetilde{\boldsymbol{u}}|\boldsymbol{\theta}) = P_{\boldsymbol{e}}(\widetilde{\boldsymbol{u}} - \boldsymbol{u}(\boldsymbol{\theta})), \quad \boldsymbol{\theta} \in \boldsymbol{\Theta}, \tag{4.26}$$

where $\boldsymbol{\Theta}$ is the parameter space. Furthermore, any prior knowledge on $\boldsymbol{\theta}$ is described by a prior probability distribution: $p(\boldsymbol{\theta})$, $\boldsymbol{\theta} \in \boldsymbol{\Theta}$. Bayes' theorem is then applied to derive the posterior distribution of parameters $\boldsymbol{\theta}$ to quantify uncertainty and handle prior information. This posterior distribution is:

$$p(\boldsymbol{\theta}|\widetilde{\boldsymbol{u}}) = c \cdot p(\boldsymbol{\theta}) L(\boldsymbol{\theta}; \widetilde{\boldsymbol{u}}), \quad \boldsymbol{\theta} \in \boldsymbol{\Theta}, \tag{4.27}$$

where c is a normalizing constant. The posterior distribution is considered as the solution of the inverse problem and can be studied in terms of maximum *a posteriori*, marginal distributions of some parameters, covariance, etc. Yet, the assumption that all information can be described through probability distributions may be too strong. The measurement error $\boldsymbol{e}_{meas}$ is objective; it represents the intrinsic variability of measurement experiments. Hence, it is reasonable to use a probability distribution to represent $\boldsymbol{e}_{meas}$. In contrast, it is debatable to make the same assumption for $\boldsymbol{e}_{model}$. Model uncertainty may arise from approximation error, missing parameters or other situations due to incomplete information. Unfortunately, we often lack information to represent $\boldsymbol{e}_{model}$ by a probability distribution. For example, homogenization-induced model uncertainty is one kind of model uncertainty which cannot always be represented by probability approaches. We therefore aim at proposing a strategy similar to the Bayesian inference but in the more general framework of belief functions.

4.3.2 Likelihood-based belief functions

Firstly, we will focus on the way to build a likelihood function taking into account both measurement and model errors and their natures. It will be applied directly in Chapter 5. The likelihood-based belief functions give us a view to handle both measurement and model uncertainties without assuming the model uncertainty to be aleatory. It is an evidential likelihood-based approach, which was proposed by [Shafer, 1976] and justified by [Denœux, 2014]. If model uncertainty is neglected, the relation between displacement measurement $\widetilde{\boldsymbol{u}}$ and predicted values $\boldsymbol{u}(\boldsymbol{\theta})$ can be written as follows:

$$\widetilde{\boldsymbol{u}} = \boldsymbol{u}(\boldsymbol{\theta}) + \boldsymbol{e}_{meas}. \tag{4.28}$$

Then, the uncertainty about $\boldsymbol{\theta}$ given experimental measurement is represented as follows:

$$pl(\boldsymbol{\theta}; \widetilde{\boldsymbol{u}}) = \frac{L(\boldsymbol{\theta}; \widetilde{\boldsymbol{u}})}{\sup_{\boldsymbol{\theta}} L(\boldsymbol{\theta}; \widetilde{\boldsymbol{u}})}, \tag{4.29}$$

where $pl(\boldsymbol{\theta}; \widetilde{\boldsymbol{u}})$ is the contour function about $\boldsymbol{\theta}$. The paper [Denœux, 2014] has proved that Eq. (4.29) can be derived form three basic principles: the likelihood principle, compatibility with Bayes' rule when a prior probability distribution is available and the minimal commitment principle. Furthermore, the random set describing $\boldsymbol{\theta}$ is consonant, hence it is fully described by its contour function.

Model uncertainty normally comes from incomplete information. The interval approach makes use of the two extreme values to encode uncertainty. It does not make any assumption about the error distribution between the two extremes. Therefore, it is suitable to represent the uncertainty due to incomplete information. Model uncertainty can be written as:

$$\boldsymbol{e}_{model} \in [\boldsymbol{e}_{model}] = [\underline{\boldsymbol{e}}_{model}, \overline{\boldsymbol{e}}_{model}], \tag{4.30}$$

where $\underline{\boldsymbol{e}}_{model}$ and $\overline{\boldsymbol{e}}_{model}$ denote, respectively, the lower and upper bounds of the interval. Then the contour function of material parameters given the measurement $\widetilde{\boldsymbol{u}}$ can be written as:

$$pl(\boldsymbol{\theta}; \widetilde{\boldsymbol{u}}) = \frac{L'(\boldsymbol{\theta}; \widetilde{\boldsymbol{u}})}{\sup_{\boldsymbol{\theta}} L'(\boldsymbol{\theta}; \widetilde{\boldsymbol{u}})}, \tag{4.31}$$

where

$$L'(\boldsymbol{\theta}; \widetilde{\boldsymbol{u}}) = \int_{[\boldsymbol{e}_{model}]} L(\boldsymbol{\theta}; \widetilde{\boldsymbol{u}}) d\boldsymbol{e}_{model}. \tag{4.32}$$

4.3.3 Inference based on the theory of belief functions

We then have to adapt the Bayesian inference in order to merge prior and experimental information. The prior information is considered as incomplete information in this work. The uncertainty of prior information is epistemic; it can be represented by random sets in the theory of belief functions. Then information merging is a necessary step to combine all theoretical, experimental, and empirical information for the identification. There are three information merging methods presented in Section 3.3.7.2. Considering the purpose of the identification, we choose Dempster's rule [Shafer, 1976] to combine the information. Because Dempster's rule concentrates the information, it is suitable to let us find the optimum values. Chapter 6 is dedicated to this information merging.

4.4 Conclusion

In this chapter, we introduced background knowledge on material identification including the mono-structural model, the multi-structural model, and the numerical implementation methods FEM and FE^2M. The different natures of measurement uncertainty, model uncertainty, and prior information uncertainty have been introduced to choose the suitable uncertainty representation approaches. A general framework based on likelihood-based belief functions has been proposed to take prior information into consideration and quantify all uncertainties.

Chapter 5

Identification with measurement and model uncertainties

5.1 Background and motivation

In recent years, composite materials, a kind of multi-structure materials, have been increasingly studied for their excellent performance in strength-to-weight ratio. To provide accurate and predictive simulations of composite material behaviour, many powerful tools have been proposed such as multi-structure model, homogenization model, and FE^2M as discussed in section 4.1. One prerequisite for applying these tools is to offer effective and accurate characterizations of material properties. However, unavoidable uncertainty is always an obstacle for identifying composite material properties. Besides measurement uncertainty, model uncertainty arising from simplification and approximation of real composite materials brings in some discrepancy between predicted values and actual responses in most situations as well. Considering the complexity of the composite materials, dedicated identification methods are required to quantify the unavoidable uncertainty.

In industrial practice, engineers often face two identification cases. In the first case, composite materials are tested at the micro-scale (RVE scale). A specimen is then only a sub-part of the composite material and cannot describe properly its variability between RVEs. However, the homogeneous parameters of the whole material are the targets of interest to be identified. The discrepancy between heterogeneous micro-scale (sub-part) properties and homogeneous macro-scale (whole material) properties induce model uncertainty to this identification problem. Partially unknown micro-structures increase the model uncertainty. This case can be summarised into the case in which tests and measurements are at micro-scale and property identifications are at macro-

scale. In the second case, composite materials are suitable for an experimental test, and only macro-structure displacement fields can be measured due to limitations of measurement devices. However, heterogeneous parameters of the micro-structures are the targets of interest to be identified. Similar to the first case, micro-structures are often partially unknown as well. This case can be summarised into the case in which tests and measurements are at macro-scale and property identifications are at micro-scale. Both cases suffer from measurement and model uncertainties. In this chapter, we will discuss how to handle these uncertainties in the identification problem. The method presented is applied to the identification of composite material properties accounting for measurement and model uncertainties. And, it has a potential to be extended and applied to other identification cases suffering from uncertainty.

5.2 Identification strategy

As discussed in Section 4.3.2, measurement uncertainty is aleatory and typically represented by probabilistic approaches, while the model uncertainty is epistemic and represented by interval approaches. Likelihood-based belief function is applied to handle both uncertainties. In order to numerically implement the identification scheme, the FEM is needed to discretize the continuous mechanical model. Eq. (4.31) can be rewritten as follows:

$$pl(\boldsymbol{\theta};\widetilde{\boldsymbol{U}}) = \frac{L'(\boldsymbol{\theta};\widetilde{\boldsymbol{U}})}{\sup_{\boldsymbol{\theta}} L'(\boldsymbol{\theta};\widetilde{\boldsymbol{U}})}, \tag{5.1}$$

where $\widetilde{\boldsymbol{U}}$ is the vector of discrete measurement field data. The integrated likelihood function in Eq. (4.32) can be rewritten as:

$$L'(\boldsymbol{\theta};\widetilde{\boldsymbol{U}}) = \int_{[\boldsymbol{E}_{model}]} L(\boldsymbol{\theta};\widetilde{\boldsymbol{U}})\mathrm{d}\boldsymbol{E}_{model}, \tag{5.2}$$

where

$$\widetilde{\boldsymbol{U}} = \boldsymbol{U}(\boldsymbol{\theta}) + \boldsymbol{E}_{meas} + \boldsymbol{E}_{model}.$$

The displacement field $\boldsymbol{u}$ is replaced by the corresponding vector $\boldsymbol{U}$ whose components are the FEM predicted values projected from the FE mesh to the measurement grid. Besides $\boldsymbol{U}$, the random field $\boldsymbol{e}_{meas}$ is replaced by the random vector $\boldsymbol{E}_{meas}$; the interval $[\boldsymbol{e}_{model}]$ is replaced by the interval vector $[\boldsymbol{E}_{model}]$. Considering that the measurement

error $\boldsymbol{E}_{meas}$ follows a probability distribution f_e, Eq. (5.2) can be written as follows:

$$L'(\boldsymbol{\theta};\widetilde{\boldsymbol{U}}) = \int_{[\boldsymbol{E}_{model}]} f_e(\widetilde{\boldsymbol{U}} - \boldsymbol{U}(\boldsymbol{\theta}) - \boldsymbol{E}_{model})\mathrm{d}\boldsymbol{E}_{model}. \tag{5.3}$$

5.2.1 Interval fields

A conservative problem arises from the independence of vector components when interval vectors are used to represented model uncertainty. In order to clearly illustrate this problem, let us consider a beam under loading as shown in Fig. 5.1. The properties of the beam are deterministic, while the uncertain load f is represented by an interval $[\underline{f}, \overline{f}]$. The shaded area corresponds to the displacement vectors between the superior

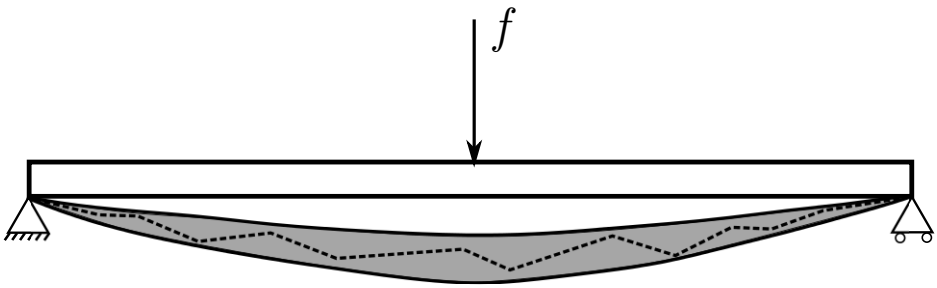

Fig. 5.1 Conservatism arising from independent components

and inferior boundaries of the beam deformation which can be described by an interval vector. The dashed line corresponds to a curve located inside the interval vector, however, it is not a possible response. Therefore, the interval vector contains some impossible solutions.

5.2.1.1 Definition of interval field

In order to solve the problem presented above, we introduce a concept named interval field, proposed by [Moens et al., 2011] and [Verhaeghe et al., 2013], to represent the model uncertainty. An interval field is denoted as:

$$[\boldsymbol{U}] = \boldsymbol{\Phi}[\boldsymbol{\eta}], \tag{5.4}$$

where $[\boldsymbol{U}]$ is an interval vector including n components, $\boldsymbol{\Phi}$ is a matrix including n_b basis vectors:

$$\boldsymbol{\Phi} = (\boldsymbol{\phi}_1, \cdots, \boldsymbol{\phi}_{n_b}).$$

The interval vector $[\boldsymbol{\eta}]$ contains n_b independent interval components:

$$[\boldsymbol{\eta}] = ([\underline{\eta}_1, \overline{\eta}_1], \cdots, [\underline{\eta}_{n_b}, \overline{\eta}_{n_b}])^T.$$

When the components of $[\boldsymbol{U}]$ are dependent, the number n_b can be reduced to much smaller value than n without missing information. The dependence among the components of $[\boldsymbol{U}]$ is expressed by matrix $\boldsymbol{\Phi}$. Since the model uncertainty comes from incomplete information, the subjective knowledge may dominate representation of model uncertainty. The freedom in choosing the basis vectors is ideal to reflect this subjective knowledge. By introducing the interval field to express the model uncertainty, Eq. (5.3) can be rewritten as follows:

$$L'(\boldsymbol{\theta}; \widetilde{\boldsymbol{U}}) = \int_{[\boldsymbol{\eta}]} f_e(\widetilde{\boldsymbol{U}} - \boldsymbol{U}(\boldsymbol{\theta}) - \boldsymbol{\Phi}\boldsymbol{\eta}) \mathrm{d}\boldsymbol{\eta}, \tag{5.5}$$

where f_e is the probability distribution representing the measurement errors.

5.2.1.2 Likelihood for Gaussian distributions

Gaussian distributions are very common continuous probability distributions to represented measurement error. When the measurement error follows a Gaussian distribution $\boldsymbol{E}_{meas} \sim \mathcal{N}(\boldsymbol{0}, \boldsymbol{D})$, the likelihood can be written as:

$$L'(\boldsymbol{\theta}) = A_0 \int_{[\boldsymbol{\eta}]} \exp\big(-\frac{1}{2}\big(\widetilde{\boldsymbol{U}} - \boldsymbol{U}(\boldsymbol{\theta}) - \boldsymbol{\Phi}\boldsymbol{\eta}\big)^T \boldsymbol{D}^{-1} \big(\widetilde{\boldsymbol{U}} - \boldsymbol{U}(\boldsymbol{\theta}) - \boldsymbol{\Phi}\boldsymbol{\eta}\big)\big) \mathrm{d}\boldsymbol{\eta}. \tag{5.6}$$

where $\boldsymbol{D}$ is the covariance matrix, A_0 is a value only depending on $\boldsymbol{D}$. After some simple algebraic operations, we have:

$$\begin{aligned} L'(\boldsymbol{\theta}) \;=\; & A_0 \int_{[\boldsymbol{\eta}]} \exp\big(-\frac{1}{2}\big(\widetilde{\boldsymbol{U}} - \boldsymbol{U}(\boldsymbol{\theta})\big)^T \boldsymbol{D}^{-1} \big(\widetilde{\boldsymbol{U}} - \boldsymbol{U}(\boldsymbol{\theta})\big) + \\ & \big(\widetilde{\boldsymbol{U}} - \boldsymbol{U}(\boldsymbol{\theta})\big)^T \boldsymbol{D}^{-1} \boldsymbol{\Phi}\boldsymbol{\eta} - \frac{1}{2}\boldsymbol{\eta}^T \boldsymbol{\Phi}^T \boldsymbol{D}^{-1} \boldsymbol{\Phi}\boldsymbol{\eta}\big) \mathrm{d}\boldsymbol{\eta}. \end{aligned} \tag{5.7}$$

Let us note $\boldsymbol{S}$ such that:

$$\boldsymbol{S} = \boldsymbol{\Phi}^T \boldsymbol{D}^{-1} \boldsymbol{\Phi}. \tag{5.8}$$

The eigenvalue decomposition of $\boldsymbol{S}$ can be written as follows:

$$\boldsymbol{\Psi}^T \boldsymbol{S} \boldsymbol{\Psi} = \boldsymbol{\Upsilon}, \tag{5.9}$$

where $\boldsymbol{\Psi}$ is an orthogonal matrix and $\boldsymbol{\Upsilon}$ is a diagonal matrix with γ_i the i-th diagonal term. Let us construct the vector $\boldsymbol{x}$ such that:

$$\boldsymbol{x} = \boldsymbol{\Psi}^{-1}\boldsymbol{\eta} = \boldsymbol{\Psi}^{T}\boldsymbol{\eta}. \tag{5.10}$$

Then the likelihood can be written as:

$$\begin{aligned} L'(\boldsymbol{\theta}) \;=\; & A_0 \int_{[\boldsymbol{x}]} \exp\big(-\frac{1}{2}\big(\widetilde{\boldsymbol{U}} - \boldsymbol{U}(\boldsymbol{\theta})\big)^T \boldsymbol{D}^{-1}\big(\widetilde{\boldsymbol{U}} - \boldsymbol{U}(\boldsymbol{\theta})\big) + \\ & \big(\widetilde{\boldsymbol{U}} - \boldsymbol{U}(\boldsymbol{\theta})\big)^T \boldsymbol{D}^{-1}\boldsymbol{\Phi}\boldsymbol{\Psi}\boldsymbol{x} - \frac{1}{2}\boldsymbol{x}^T\boldsymbol{\Upsilon}\boldsymbol{x}\big)|\boldsymbol{\Psi}|\mathrm{d}\boldsymbol{x}. \end{aligned} \tag{5.11}$$

Let us denote:

$$\begin{aligned} a_i &= \sqrt{\gamma_i}, \\ (b_1, \cdots, b_{n_b}) &= \big(\widetilde{\boldsymbol{U}} - \boldsymbol{U}(\boldsymbol{\theta})\big)^T \boldsymbol{D}^{-1}\boldsymbol{\Phi}\boldsymbol{\Psi}, \\ \delta u^2 &= \big(\widetilde{\boldsymbol{U}} - \boldsymbol{U}(\boldsymbol{\theta})\big)^T \boldsymbol{D}^{-1}\big(\widetilde{\boldsymbol{U}} - \boldsymbol{U}(\boldsymbol{\theta})\big). \end{aligned}$$

Finally the likelihood can be written as follows:

$$L'(\boldsymbol{\theta}) = A_0 \exp(-\frac{\delta u^2}{2})\Big(\prod_i^{n_b} \exp(\frac{b_i^2}{2a_i^2})\Big)\Big(\prod_i^{n_b} \int_{[x_i]} \exp(-\frac{1}{2}(a_i x_i - \frac{b_i}{a_i})^2)\mathrm{d}x_i\Big). \tag{5.12}$$

The third term in the right hand term of Eq. (5.12) can be obtained using error function [Andrews, 1997]:

$$\mathrm{erf}(x) = \frac{2}{\sqrt{\pi}} \int_0^x e^{-t^2}\mathrm{d}t. \tag{5.13}$$

In the case of Gaussian noise, the calculation of integration of likelihood can be significantly reduced with the help of interval fields and the error function.

5.2.2 Identification of multi-structure materials

As presented in Section 5.1, we engage in two identification cases of multi-structure materials: (1) test and measure at micro-scale and identify macro-scale properties (2) test and measure at macro-scale and identify micro-scale properties. In this section, we will present the identification processes in detail for the two cases.

5.2.2.1 Identifying macro-scale properties by micro-scale tests

In the first case, we assume that we can only do a tensile test to a material at micro-scale, while its macro-scale properties need to be identified. The materials at

the micro-scale are heterogeneous, but, their macro-scale properties can be considered as homogeneous. The discrepancy between micro and macro scale induces model uncertainty, which is represented by interval fields. Moreover, their micro-structures are partially unknown. That means we only know the three statistical factors (A_f, A_r, and D_a introduced in Section 4.1.3), and their exact material distributions are unknown. Besides model uncertainty, measurement uncertainty should be accounted for as well. In this thesis, we assume that the measurement uncertainty follows a Gaussian distribution.

Construction of the basis vectors used to define the interval field (Eq. (5.4)) plays an important role in model uncertainty representation using interval fields. As mentioned above, the choice of the basis vectors Φ reflect subjective opinions about the model uncertainty. Furthermore, the choice of Φ should depend on practical situations. In this chapter, model uncertainty is mainly induced by homogenising and partially unknown micro-structures. Therefore, the basic vectors are chosen considering the homogenization process and statistical descriptions of micro-structures. With the statistical factors, it is possible to sample a group of micro-structures and extract the basis vectors Φ by Proper Orthogonal Decomposition (POD). POD, also known as Karhunen-Loève decomposition (KLD) or Principle component analysis (PCA) [Jolliffe, 2002], is capable of reducing a large number of interdependent variables to a much smaller number of uncorrelated variables. Some introductions about POD are presented in [Berkooz et al., 1993] [Newman, 1996] and [Liang et al., 2002]. We make use of its variable reduction ability to extract the basis vectors of interval fields.

Assuming a set of statistical factors (A_f, A_r, D_a), a group of dual-phase materials can be generated using the computational algorithms proposed in [Tschopp et al., 2008]. We assume that the component material properties of the dual-phase materials are known. For every micro-structure, the actual displacement denoted as an $m \times 1$ vector $\boldsymbol{U}^j$ under the given boundary conditions corresponding to the experiment can be calculated using the FEM. The effective elastic parameters ${}^h\boldsymbol{\theta}^j$ can be obtained by the homogenization scheme presented in Section 4.1.3, where $j = 1, \cdots, n$ corresponds to the j-th micro-structure and superscript h means homogenised values. Then the discrepancy between the displacements from heterogeneous materials $\boldsymbol{U}^j$ and those from homogenised materials $\boldsymbol{U}({}^h\boldsymbol{\theta}^j)$ with the same loading can be written as follows:

$$\mathrm{d}\boldsymbol{U}^j = \boldsymbol{U}^j - \boldsymbol{U}({}^h\boldsymbol{\theta}^j). \tag{5.14}$$

In [Kerschen et al., 2005], several means of computing the POD were presented. Here we carry it out using singularvalue decomposition (SVD). Noting an $m \times n$ matrix:

$$\mathrm{d}\boldsymbol{U}_{dev} = (\mathrm{d}\boldsymbol{U}_1 - \mathrm{d}\overline{\boldsymbol{U}}, \mathrm{d}\boldsymbol{U}_2 - \mathrm{d}\overline{\boldsymbol{U}}, \cdots, \mathrm{d}\boldsymbol{U}_n - \mathrm{d}\overline{\boldsymbol{U}}), \tag{5.15}$$

where

$$\mathrm{d}\overline{\boldsymbol{U}} = \frac{1}{n}\sum_{j=1}^{n} \mathrm{d}\boldsymbol{U}^j \tag{5.16}$$

is the average of $\mathrm{d}\boldsymbol{U}^j$, $j = 1, \cdots, n$. The SVD of $\mathrm{d}\boldsymbol{U}_{dev}$ can be written as follows:

$$\mathrm{d}\boldsymbol{U}_{dev} = \boldsymbol{W}\boldsymbol{S}\boldsymbol{V}^T, \tag{5.17}$$

where $\boldsymbol{W}$ is an $m \times m$ orthogonal matrix containing left singular vectors, $\boldsymbol{S}$ is an $m \times n$ pseudo-diagonal matrix with diagonal entries containing singular values ϱ_i, $i = 1, \cdots, n$, and $\boldsymbol{V}$ is an $n \times n$ orthogonal matrix containing right singular vectors. A given number of columns of matrix $\boldsymbol{W}$ can be used as basis vectors in $\boldsymbol{\Phi} = (\boldsymbol{\phi}_1, \cdots, \boldsymbol{\phi}_{n_b})$. The choice of the truncation number n_b depends on the relative magnitudes of the singular values ϱ_i, $i = 1, \cdots, n$, and usually $n_b \ll n$. If $\mathrm{d}\boldsymbol{U}^j$, $j = 1, \cdots, n$, are correlated, the first several singular values are much bigger than the others. In this case, we can say that the first several basis vectors correspond to the majority of the energy. With the help of the basis vectors, approximation of the discrepancy $\mathrm{d}\boldsymbol{U}^j$ can be obtained as follows:

$$\mathrm{d}\boldsymbol{U}^j \approx \mathrm{d}\overline{\boldsymbol{U}} + \sum_{i=1}^{n_b} \boldsymbol{\phi}_i \eta_{ij}, \tag{5.18}$$

where

$$\eta_{ij} = (\mathrm{d}\boldsymbol{U}_j - \mathrm{d}\overline{\boldsymbol{U}})^T \boldsymbol{\phi}_i. \tag{5.19}$$

The values η_{ij} can be used to estimate the interval vectors $[\boldsymbol{\eta}]$:

$$[\underline{\eta}_i, \overline{\eta}_i] = [\min_j(\eta_{ij}), \max_j(\eta_{ij})], \tag{5.20}$$

where $i = 1, \cdots, n_b$ and $j = 1, \cdots, n$. The interval field describing the model uncertainty can be written as follows:

$$[\mathrm{d}\boldsymbol{U}] = \mathrm{d}\overline{\boldsymbol{U}} + \boldsymbol{\Phi}[\boldsymbol{\eta}], \tag{5.21}$$

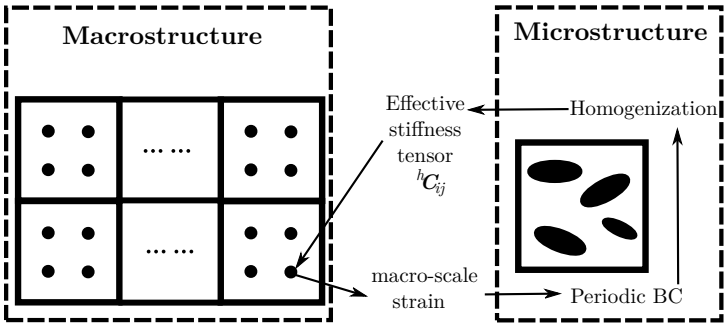

Fig. 5.2 FE^{2}M scheme

where $[\boldsymbol{\eta}] = ([\underline{\eta}_1, \overline{\eta}_1], \cdots, [\underline{\eta}_{n_b}, \overline{\eta}_{n_b}])^T$. Finally, the integrated likelihood function in Eq. (5.5) can be written as follows:

$$L'(\boldsymbol{\theta}; \widetilde{\boldsymbol{U}}) = \int_{[\boldsymbol{\eta}]} f_e(\widetilde{\boldsymbol{U}} - \boldsymbol{U}(\boldsymbol{\theta}) - \mathrm{d}\overline{\boldsymbol{U}} - \boldsymbol{\Phi}\boldsymbol{\eta})\mathrm{d}\boldsymbol{\eta}, \tag{5.22}$$

where f_e is the probability distribution representing the measurement errors. Finally, we can substitute Eq. (5.22) into Eq. (5.1) to construct the contour function.

The discussion above presents how to choose the basis vectors $\boldsymbol{\Phi}$ and the interval vectors $[\boldsymbol{\eta}]$ based on the statistical factors and the homogenization method. When there is not enough experimental data to estimate these factors, subjective prior opinions can be used to directly choose the basis vectors.

5.2.2.2 Identifying micro-scale properties by macro-scale tests

In the second case, we assume that we can perform tensile tests to multi-structural materials at their macro-scale, while the micro-scale properties are needed to be identified. In this case, multi-structure mechanical simulations are implemented using FE^{2}M, whose implementation scheme is shown in Fig. 5.2. We can see that the properties of macro-structures are obtained from homogenization of micro-structures. The partial unknown micro-structures will induce model uncertainty.

Similar to the first case, model uncertainty is also represented by interval fields. Considering the model uncertainty arising from partial unknown micro-structures, we propose a process based on a POD on the elastic tensor and perturbation method to construct interval fields. With a set of statistical factors (A_f, A_r, D_a), a group of micro-structures can be drawn using the computational algorithms proposed in [Tschopp et al., 2008]. For each micro-structure, the effective elastic tensors, denoted as $^h\boldsymbol{C}_j$, can be calculated with preliminary micro-scale $\boldsymbol{\theta}^0$ using the homogenization method

introduced in Section 4.1.3, where $j = 1, \cdots, n$, corresponding the j-th micro-structure and superscript h denotes that the values are obtained using the homogenization method. In order to perform POD, each ${}^h\boldsymbol{C}_j$ is restored in a vector ${}^h\boldsymbol{c}_j$ of length 6. Noting $\boldsymbol{C}_{dev} = ({}^h\boldsymbol{c}_1 - {}^h\,\overline{\boldsymbol{c}}, {}^h\,\boldsymbol{c}_2 - {}^h\,\overline{\boldsymbol{c}}, \cdots, {}^h\,\boldsymbol{c}_n - {}^h\,\overline{\boldsymbol{c}})$, its SVD can be written as follows:

$$\boldsymbol{C}_{dev} = \boldsymbol{W}\boldsymbol{S}\boldsymbol{V}^T, \tag{5.23}$$

where ${}^h\overline{\boldsymbol{c}} = \dfrac{1}{n}(\sum_{j=1}^{n} {}^h\boldsymbol{c}_j)$ is the average of ${}^h\boldsymbol{c}_j$, $j = 1, \cdots, n$. The basis vectors $\boldsymbol{\chi} = (\chi_1, \cdots, \chi_{n_b})$ are chosen from the columns of the vector $\boldsymbol{W}$. Similar to the first case, the choice of truncation number n_b depends on the relative magnitudes of the singular values ϱ_i, $i = 1, \cdots, n$. With the help of the basis vectors, approximation of ${}^h\boldsymbol{c}_j$ is obtained as follows:

$${}^h\boldsymbol{c}_j \approx {}^h\,\overline{\boldsymbol{c}} + \sum_{i=1}^{n_b} \boldsymbol{\chi}_i \alpha_{ij}, \tag{5.24}$$

where

$$\alpha_{ij} = ({}^h\boldsymbol{c}_j - {}^h\,\overline{\boldsymbol{c}})^T \boldsymbol{\chi}_i. \tag{5.25}$$

The values α_{ij} can be used to estimate the interval vector $[\alpha_i]$:

$$[\underline{\alpha}_i, \overline{\alpha}_i] = [\min_j(\alpha_{ij}), \max_j(\alpha_{ij})], \tag{5.26}$$

where $i = 1, \cdots, n_b$ and $j = 1, \cdots, n$. The effective elastic tensor interval can be written as follows:

$$[\boldsymbol{c}] = {}^h\,\overline{\boldsymbol{c}} + [\Delta\boldsymbol{c}] = {}^h\,\overline{\boldsymbol{c}} + \boldsymbol{\chi}[\boldsymbol{\alpha}], \tag{5.27}$$

where $\boldsymbol{\chi} = (\boldsymbol{\chi}_1, \cdots, \boldsymbol{\chi}_{n_b})$ and $[\boldsymbol{\alpha}] = ([\underline{\alpha}_1, \overline{\alpha}_1], \cdots, [\underline{\alpha}_{n_b}, \overline{\alpha}_{n_b}])^T$.

The perturbation method proposed in [McWilliam, 2001] is employed to propagate interval elastic tensors to interval displacement fields. Let us consider a matrix equation that arises in static finite element analysis:

$$\boldsymbol{K}_0\boldsymbol{U}_0 = \boldsymbol{F}_0, \tag{5.28}$$

where $\boldsymbol{K}_0$, $\boldsymbol{U}_0$ and $\boldsymbol{F}_0$ are the nominal matrix and vectors associated with the nominal values (middle value) $\boldsymbol{c}_0$ of interval $[\boldsymbol{c}]$:

$$\boldsymbol{c}_0 = {}^h\,\overline{\boldsymbol{c}} + \sum_{i=1}^{n_b} \boldsymbol{\chi}_i \alpha_{0i}. \tag{5.29}$$

The scalar value α_{0i} is the nominal value of interval $[\underline{\alpha}_i, \overline{\alpha}_i]$:

$$\alpha_{0i} = \frac{\overline{\alpha}_i - \underline{\alpha}_i}{2}, \ i = 1, \cdots, n_b. \tag{5.30}$$

Under the assumption of small perturbation, the displacement of a perturbed system can be approximated by [Chen et al., 2002]:

$$\boldsymbol{U} = \boldsymbol{U}_0 + \Delta\boldsymbol{U} \approx \boldsymbol{U}_0 + \boldsymbol{K}_0^{-1}(\Delta\boldsymbol{F} - \Delta\boldsymbol{K}\boldsymbol{U}_0), \tag{5.31}$$

where $\Delta\boldsymbol{K}$ and $\Delta\boldsymbol{F}$ are respectively the small perturbations of the stiffness matrix $\boldsymbol{K}$ and the load vector $\boldsymbol{F}$. In this work, there is no perturbation in $\boldsymbol{F}$ and then $\Delta\boldsymbol{K}$ is expressed as follows:

$$\Delta\boldsymbol{K} = \sum_{i=1}^{n_b}(\alpha_i - \alpha_{0i})\frac{\partial\boldsymbol{K}}{\partial\alpha_i}|_{\alpha_i=\alpha_{0i}}, \tag{5.32}$$

where α_i is one of the uncertain variables, $i = 1, \cdots, n_b$. Considering the linear assembling relationship between $\boldsymbol{K}$ and ${}^h\boldsymbol{c}$:

$$\boldsymbol{K}({}^h\boldsymbol{c}) = \boldsymbol{K}({}^h\overline{\boldsymbol{c}}) + \sum_{i=1}^{n_b}\alpha_i\boldsymbol{K}(\boldsymbol{\chi}_i), \tag{5.33}$$

it is easy to obtain:

$$\Delta\boldsymbol{K} = \sum_{i=1}^{n_b}(\alpha_i - \alpha_{0i})\boldsymbol{K}(\boldsymbol{\chi}_i). \tag{5.34}$$

Substituting Eq. (5.34) into (5.31), the perturbation of displacement can be written as follows:

$$\Delta\boldsymbol{U} = -\sum_{i=1}^{n_b}(\alpha_i - \alpha_{0i})\boldsymbol{K}_0^{-1}\boldsymbol{K}(\boldsymbol{\chi}_i)\boldsymbol{U}_0. \tag{5.35}$$

Let us denote

$$\boldsymbol{\Phi} = (\boldsymbol{K}_0^{-1}\boldsymbol{K}(\boldsymbol{\chi}_1)\boldsymbol{U}_0, \cdots, \boldsymbol{K}_0^{-1}\boldsymbol{K}(\boldsymbol{\chi}_{n_b})\boldsymbol{U}_0),$$

$$[\boldsymbol{\eta}] = \boldsymbol{\alpha}_0 - [\boldsymbol{\alpha}],$$

where $\boldsymbol{\alpha}_0 = (\alpha_{01}, \cdots, \alpha_{0n_b})^T$. It should be noticed that the $[\boldsymbol{\alpha}]$ are constructed based on the centralized matrix $\boldsymbol{C}_{dev}$. Hence, the nominal vector $\boldsymbol{\alpha}_0$ is often very close to zero, which allows us to perturb the system at original points. In this case, we have $\boldsymbol{c}_0 = {}^h\ \overline{\boldsymbol{c}}$ and $[\boldsymbol{\eta}] = -[\boldsymbol{\alpha}]$.

The interval vector of displacement can be written as follows:

$$[\boldsymbol{U}] = \boldsymbol{U}_0 + [\Delta \boldsymbol{U}] = \boldsymbol{U}_0 + \boldsymbol{\Phi}[\boldsymbol{\eta}]. \tag{5.36}$$

Then the integrated likelihood function in Eq. (5.5) is:

$$L'(\boldsymbol{\theta}; \widetilde{\boldsymbol{U}}) = \int_{[\boldsymbol{\eta}]} f_e(\widetilde{\boldsymbol{U}} - \boldsymbol{U}_0(\boldsymbol{\theta}) - \boldsymbol{\Phi}\boldsymbol{\eta}) \mathrm{d}\boldsymbol{\eta}, \tag{5.37}$$

where f_e is the probability distribution representing the measurement errors. Finally, we can substitute Eq. (5.37) into Eq. (5.1) to construct the contour function. The scheme to calculate the contour function based on an integrated likelihood is shown in Fig. 5.3.

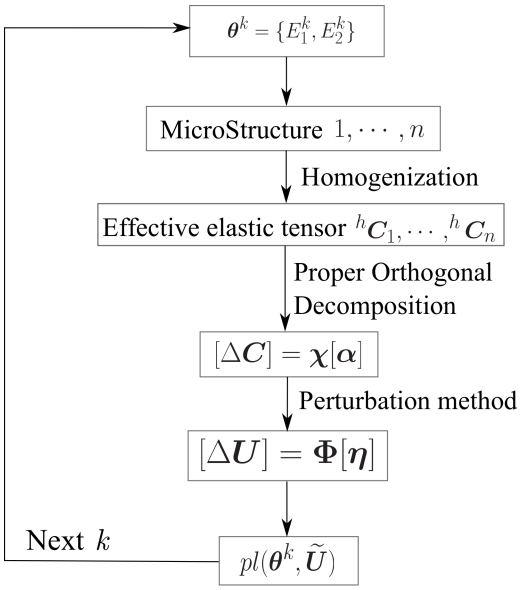

Fig. 5.3 Algorithm for constructing contour functions

5.2.3 Exploitation of the contour function

We can calculate contour functions based on integrated likelihood functions. The contour functions are capable of quantifying the uncertainty of parameters to be identified. Four methods to exploit the contour functions are considered:

- Maximisation of the contour functions. We can search the arguments at which the contour functions values are maximum. The maximisation of the contour functions can serve for deterministic identification.

- Cut of the contour functions at ω-level. This exploitation can provide set-valued results, which can serve for non-deterministic identification.
- Marginalization of the contour functions. It is a good tool to visualise the uncertainty when the number of parameters is larger than 2.
- Combination with other sources of information. The contours functions can be combined with prior information to improve its precision as proposed in Chapter 6.

5.3 Numerical Application

In this section, we present two numerical applications to study the effectiveness and efficiency of our method. The applications are limited to the 2D plate model and the displacement measurement fields are simulated by the FEM or FE^{2}M. Gaussian white noise is added to the displacement fields to synthesise measurement noise.

5.3.1 Identifying macro-scale properties from micro-scale tests

5.3.1.1 Measurement and basis vectors

In this section, we choose a case of identifying the macro elastic properties of a dual-phase 2D plate as shown in Fig. 5.4. The plate is loaded on the right by a force

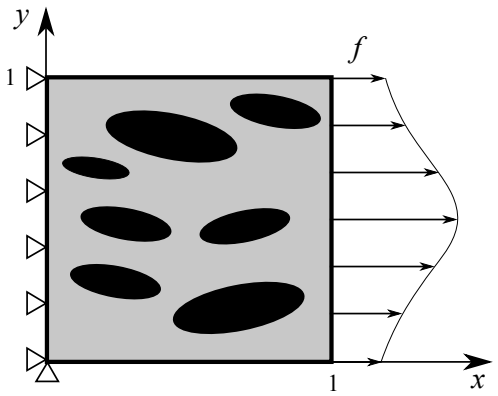

Fig. 5.4 Physical model of tests at micro-scale

$\boldsymbol{f}$ whose horizontal projection is $\boldsymbol{f}_x = f_0 y(1-y)$ and vertical projection is null. The matrix phase (grey region) is denoted as material 1 and the reinforce phase (black region) is denoted as material 2. We assume its statistical factors are known: $A_f = 45\%$,

$A_r = 1.92$, and orientation degree D_a follows $\mathcal{N}(0°, (10°)^2)$. The elastic tensor in the 2D isotropic case can be written as:

$$\boldsymbol{C} = \begin{bmatrix} C_{11} & C_{12} & 0 \\ C_{12} & C_{22} & 0 \\ 0 & 0 & C_{33} \end{bmatrix} = \begin{bmatrix} \lambda + 2\mu & \lambda & 0 \\ \lambda & \lambda + 2\mu & 0 \\ 0 & 0 & \mu \end{bmatrix}. \tag{5.38}$$

The parameters $\boldsymbol{\theta} = \{\lambda, \mu\}$ are the two Lamé parameters determining the elastic properties. Considering the plate as a dual-phase material, the heterogeneous parameters are denoted by $\boldsymbol{\theta} = \{\lambda_1, \mu_1, \lambda_2, \mu_2\}$. The measurement is the displacement field on the whole plate. It is created based on a reference finite element calculation with reference values $\boldsymbol{\theta}_0 = \{1, 1, 2, 2\}$. The displacement field is measured on the heterogeneous plate, meanwhile the material model used for the identification is based on a homogeneous isotropic plate in order to find the macro parameters. Therefore, model uncertainty is mainly caused by simplification from a heterogeneous model to a homogeneous one. We choose the effective elastic parameters based on the numerical homogenization algorithm presented in Section 4.1.3 as the reference values. After homogenization, the constitutive behaviour may no longer be isotropic. That means Eq. (5.38) is not established. The identification frame still approximate the homogenised material to be isotropic. Therefore, we calculate ${}^h\boldsymbol{\theta} = \{{}^h\lambda, {}^h\mu\}$ via minimising a Frobenius norm $||{}^h\boldsymbol{C} - \boldsymbol{C}(\lambda, \mu)||_F$ as follows:

$${}^h\boldsymbol{\theta} = \arg\min_{\lambda,\mu} \sum_p \sum_q \left({}^hC_{pq} - C_{pq}(\lambda, \mu)\right)^2, \tag{5.39}$$

where p and q are subscripts of components in a matrix, and $C_{pq}(\lambda, \mu)$ is defined in Eq. (5.38).

As mentioned in Section 5.2.2.1, POD is applied to construct basis vectors $\boldsymbol{\Phi}$ and interval vectors $[\boldsymbol{\eta}]$. In this example, $N = 50$ micro-structures are generated priorly. Then the corresponding homogenised values $\{{}^h\lambda^j, {}^h\mu^j\}$ and actual displacement vectors $\boldsymbol{U}^j$, $j = 1, \cdots, N$, are calculated based on homogenization scheme and the FEM. After performing a POD to d$\boldsymbol{U}^j$, we can obtain the basis vectors $\boldsymbol{\Phi}$ and their corresponding eigenvalues $\boldsymbol{\varrho} = \{\varrho_1, \cdots, \varrho_N\}$. In order to determine the truncation number n_b, the energy proportion of a basis vector $\boldsymbol{\phi}_i$ is defined as follows:

$$Ep_i = \varrho_i / \sum_{i=1}^{N} \varrho_i. \tag{5.40}$$

The first six Ep values are shown in Fig. 5.5. We can see that the first three singular values correspond to the majority of the energy (75.75%). Therefore, it seems reasonable to use the first three basis vectors to represent the interval fields, because the original vectors are strongly correlated.

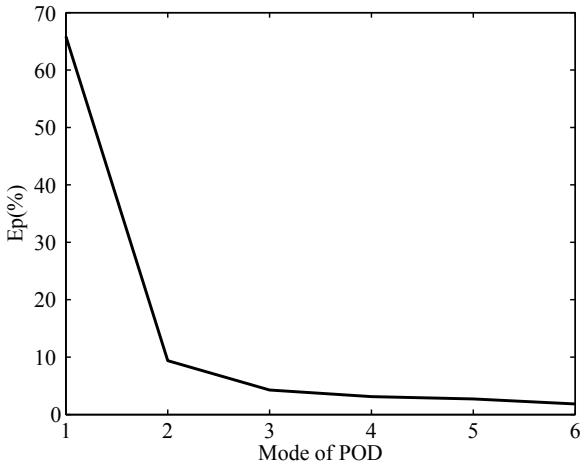

Fig. 5.5 Energy proportion Ep

5.3.1.2 Identification results

A heterogeneous plate with the same statistical factors as those used to construct the basis vectors is generated, as shown in Fig. 5.6(a), to represent a specimen at micro-scale. The homogeneous macro elastics parameters are to be identified. The measurement field $\widetilde{\boldsymbol{U}}$ is synthetic data created by the FEM. The FE mesh of the heterogeneous plate is shown in Fig. 5.6(b). The measurement grids are 50×50 covering the whole plate, and a Gaussian white noise is added to simulate measurement uncertainty. The standard deviation of the noise is 15% with respect to the average displacement value. The reference values, homogeneous effective parameters, are obtained by applying homogenization scheme to the FE mesh in Fig. 5.6(b). During the identification process, the heterogeneous properties are not taken into account which induces model uncertainty. In other words, the homogeneous FE mesh in Fig. 5.6(c) is used to establish prediction model $\boldsymbol{U}(\boldsymbol{\theta})$.

We have illustrated two methods to establish contour functions. The one we proposed is based on Eq. (4.31), where an integrated likelihood function is applied, and we note it as the contour function pl_A. The other one serves as a comparison; it is based on Eq. (4.29), where a standard likelihood function is used not taking into account the

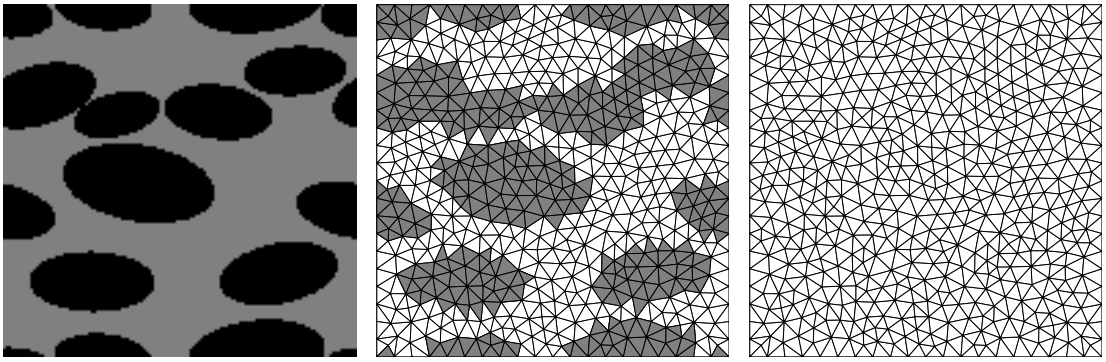

(a) Heterogeneous material (b) Heterogeneous mesh (c) Homogeneous mesh

Fig. 5.6 Specimen to be tested and identified

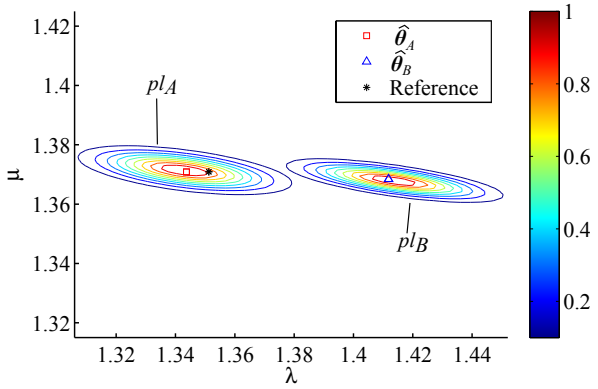

Fig. 5.7 Contour functions pl_A and pl_B

model error. We note it as the contour function pl_B. Both of them are calculated based on one measurement and plotted in Fig. 5.7. Then we estimate the parameters via maximising the contour functions pl_A and pl_B:

$$\widehat{\boldsymbol{\theta}}_A = \arg\max_{\boldsymbol{\theta}} pl_A, \tag{5.41}$$

$$\widehat{\boldsymbol{\theta}}_B = \arg\max_{\boldsymbol{\theta}} pl_B. \tag{5.42}$$

The estimators are also shown in Fig. 5.7. We can see that the estimators $\widehat{\boldsymbol{\theta}}_A$ (red square) are closer to the reference values (black star) than $\widehat{\boldsymbol{\theta}}_B$ (blue triangle). It should also be noticed that the contour function pl_A is a bit less convergent than the contour

function pl_B, because the pl_A takes more uncertainty (model uncertainty) into account than does the pl_B. A less convergent distribution is more likely to cover the reference values.

In the belief functions framework, the ω-level cut defined in Eq. (5.43) is a tool to discretize contour functions:

$$\Gamma(\omega) = \{\boldsymbol{\theta} \in \boldsymbol{\Theta} | pl(\boldsymbol{\theta}) \leq \omega\}, \quad 0 \leq \omega \leq 1. \tag{5.43}$$

It can provide set-valued results for identification problems given ω ($0 \leq \omega \leq 1$). The ω can explained as the degree of concentration of the set-valued results. It is clear that with ω increasing, the size of obtained subset decreases. When $\omega = 1$, the subset is concentrated to a single value (peak point). The contour lines in Fig. 5.7 can be seen as the cuts to the pl_A or the pl_B corresponding to various ω-levels. The scale on the left of the figure shows the ω values.

When we apply Eq. (5.22) to calculate integrated likelihood functions, there are two parts in this formulation that modify the results corresponding to pl_B: the $\mathrm{d}\overline{\boldsymbol{U}}$ and the integration. In order to illustrate the effects of the two parts, we construct two contour functions as follows:

$$pl_{\mathrm{d}\overline{\boldsymbol{U}}}(\boldsymbol{\theta}; \widetilde{\boldsymbol{U}}) = \frac{L'_{\mathrm{d}\overline{\boldsymbol{U}}}(\boldsymbol{\theta}; \widetilde{\boldsymbol{U}})}{\sup_{\boldsymbol{\theta}} L'_{\mathrm{d}\overline{\boldsymbol{U}}}(\boldsymbol{\theta}; \widetilde{\boldsymbol{U}})}, \tag{5.44}$$

and

$$pl_{int}(\boldsymbol{\theta}; \widetilde{\boldsymbol{U}}) = \frac{L'_{int}(\boldsymbol{\theta}; \widetilde{\boldsymbol{U}})}{\sup_{\boldsymbol{\theta}} L'_{int}(\boldsymbol{\theta}; \widetilde{\boldsymbol{U}})}, \tag{5.45}$$

where

$$L'_{\mathrm{d}\overline{\boldsymbol{U}}}(\boldsymbol{\theta}; \widetilde{\boldsymbol{U}}) = f_e(\widetilde{\boldsymbol{U}} - \boldsymbol{U}(\boldsymbol{\theta}) - \mathrm{d}\overline{\boldsymbol{U}}), \tag{5.46}$$

and

$$L'_{int}(\boldsymbol{\theta}; \widetilde{\boldsymbol{U}}) = \int_{[\boldsymbol{\eta}]} f_e(\widetilde{\boldsymbol{U}} - \boldsymbol{U}(\boldsymbol{\theta}) - \boldsymbol{\Phi}\boldsymbol{\eta}) \mathrm{d}\boldsymbol{\eta}. \tag{5.47}$$

Eq. (5.44) isolates the effect of $\mathrm{d}\overline{\boldsymbol{U}}$, and Eq. (5.45) isolates the effect of integration. Then we calculate and plot the contour function $pl_{\mathrm{d}\overline{\boldsymbol{U}}}$ in Fig. 5.8(a) and pl_{int} in Fig. 5.8(b). The estimators $\widehat{\boldsymbol{\theta}}_{\mathrm{d}\overline{\boldsymbol{U}}}$ and $\widehat{\boldsymbol{\theta}}_{int}$ via maximising $pl_{\mathrm{d}\overline{\boldsymbol{U}}}$ and pl_{int} are respectively defined as follows:

$$\widehat{\boldsymbol{\theta}}_{\mathrm{d}\overline{\boldsymbol{U}}} = \arg\max_{\boldsymbol{\theta}} pl_{\mathrm{d}\overline{\boldsymbol{U}}}, \tag{5.48}$$

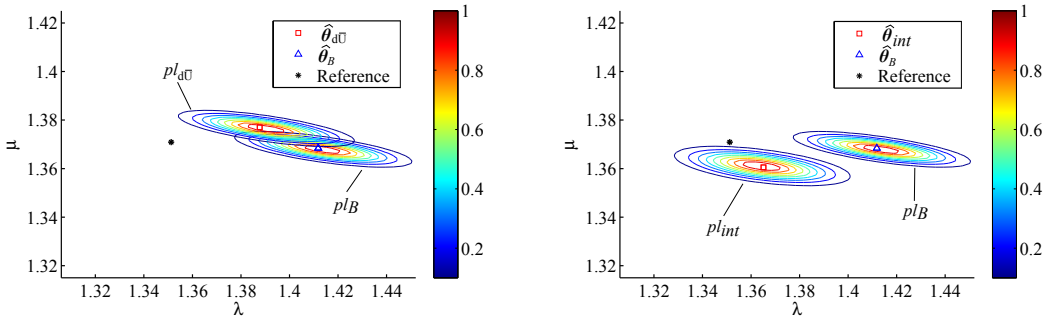

(a) Contour functions $pl_{\mathrm{d}\overline{\boldsymbol{U}}}$ and pl_B (b) Contour functions pl_{int} and pl_B

Fig. 5.8 Contour functions $pl_{\mathrm{d}\overline{\boldsymbol{U}}}$, pl_{int} and pl_B

and

$$\widehat{\boldsymbol{\theta}}_{int} = \arg\max_{\boldsymbol{\theta}} pl_{int}. \tag{5.49}$$

The contour function $pl_{\mathrm{d}\overline{\boldsymbol{U}}}$ moves a bit toward the reference values compared to the pl_B, and the shape of $pl_{\mathrm{d}\overline{\boldsymbol{U}}}$ is similar to that of pl_B. The contour function pl_{int} moves toward the reference values, meanwhile it is fatter than the pl_B. We can say that the part $\mathrm{d}\overline{\boldsymbol{U}}$ only influences positions of contour functions, and the integration influences both position and shape.

We sum up the results via maximising the contour functions pl_A, $pl_{\mathrm{d}\overline{\boldsymbol{U}}}$, pl_{int}, and pl_B in Table 5.1. The ratio r_{Hes} in Table 5.1 is the ratio between two eigenvalues of the

Table 5.1 Results via maximising contour functions

	$\boldsymbol{\theta}_{ref}$	pl_A	$pl_{\mathrm{d}\overline{\boldsymbol{U}}}$	pl_{int}	pl_B
$\widehat{\lambda}$	1.3512	1.3428	1.4118	1.3651	1.4136
$\widehat{\mu}$	1.3709	1.3714	1.3684	1.3605	1.3679
r_{Hes}	$\emptyset$	27.88	48.39	28.84	49.94
$\mathrm{d}\boldsymbol{\theta}$	$\emptyset$	0.0084	0.0393	0.0164	0.0624

Hessian matrix at maximum points defined as follows:

$$r_{Hes} = \frac{\gamma_1}{\gamma_2}, \tag{5.50}$$

where γ_1 the eigenvalue with maximum magnitude, and γ_1 the eigenvalue with minimum magnitude of the Hessian matrix at maximum points. The value $\mathrm{d}\boldsymbol{\theta}$ is the distance

between estimators and the reference values, defined as follows:

$$\mathrm{d}\boldsymbol{\theta} = \sqrt{(\widehat{\lambda} - \lambda_{\mathrm{ref}})^2 + (\widehat{\mu} - \mu_{\mathrm{ref}})^2}. \tag{5.51}$$

The values in Table 5.1 are compatible with Figs 5.7 and 5.8. The ratios r_{Hes} reflect the shapes of the contour functions at maximum points. The ratios r_{Hes} of pl_B and $pl_{\mathrm{d}\overline{\boldsymbol{U}}}$ are similar, and the ratios of pl_A and pl_{int} are similar. This finding implies that the integration influences the shapes of the contour functions. The maximum points of pl_A, $pl_{\mathrm{d}\overline{\boldsymbol{U}}}$, pl_{int} are closer to the reference values than that of pl_B, and the maximum points of pl_A are the closest to the reference values. This can be explained by the fact that both $\mathrm{d}\overline{\boldsymbol{U}}$ and integration make pl_A move to reference values.

5.3.1.3 Robustness with respect to measurement uncertainty

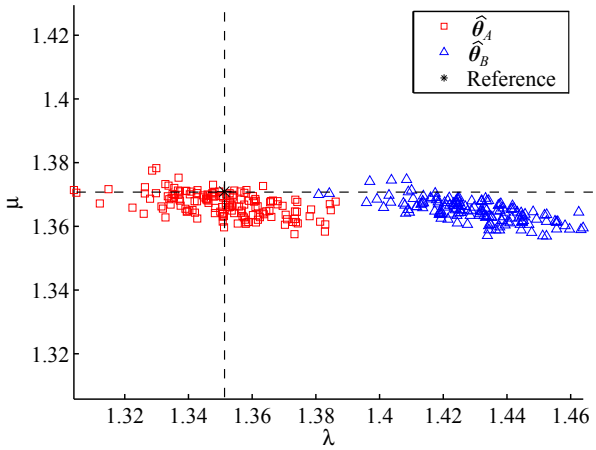

Fig. 5.9 Estimators from different experimental measurements to one specimen

The discussion above only illustrates one realisation of measurement. In order to show the robustness with respect to measurement uncertainty, 150 realisations of Gaussian noise with same standard deviation as that in Section 5.3.1.2 are generated and we add them to the displacement field to synthesise 150 measurements. This set-up simulates the situations of 150 experiments for one specimen. Then we respectively estimate the parameters, $\widehat{\boldsymbol{\theta}}_A$ and $\widehat{\boldsymbol{\theta}}_B$ via maximizing the contour functions pl_A and pl_B. The estimators are shown in Fig. 5.9. We can see that the $\widehat{\boldsymbol{\theta}}_A$ (red squares) are closer to the reference values located at the cross of the two dashed lines.

In order to clearly show the distance between estimators and the reference values, we calculate the distance $\mathrm{d}\boldsymbol{\theta}$ defined in Eq. (5.51) and plot their histograms in Fig. 5.10. Let us note that $\mathrm{d}\boldsymbol{\theta}_{\mathrm{A}}$ is associated with the contour functions pl_A, and $\mathrm{d}\boldsymbol{\theta}_{\mathrm{B}}$ is associated with pl_B. It is clear that the $\mathrm{d}\boldsymbol{\theta}_{\mathrm{A}}$ are smaller than the $\mathrm{d}\boldsymbol{\theta}_{\mathrm{B}}$. This corresponds to the fact that the $\widehat{\boldsymbol{\theta}}_A$ are closer to the reference values.

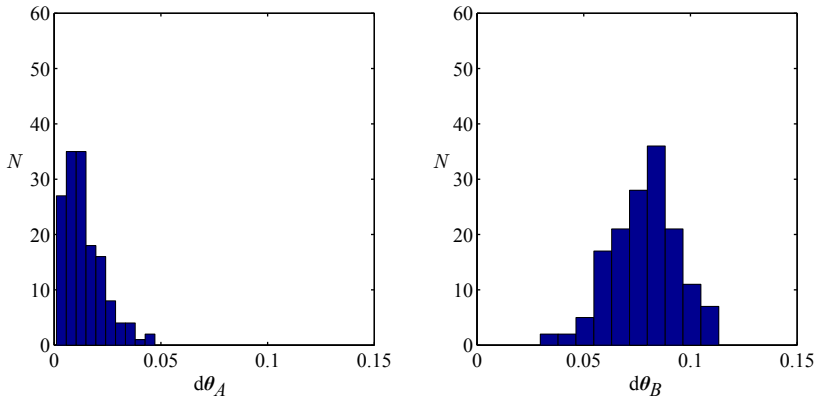

Fig. 5.10 Distance between estimators and reference values

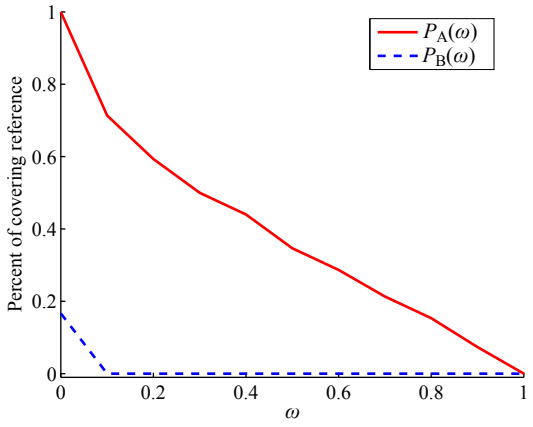

Fig. 5.11 Probability of covering reference values at different ω-level cuts

We note that $\Gamma_A(\omega)$ and $\Gamma_B(\omega)$ are cuts of, respectively, the contour functions pl_A and pl_B at ω-levels. For a group of measurement realisations, the probability of $\Gamma(\omega)$ covering the reference values is

$$P(\omega) = P(\boldsymbol{\theta}_{ref} \in \Gamma(\omega)). \tag{5.52}$$

Fig. 5.11 shows the covering probability $P_A(\omega)$ and $P_B(\omega)$ of the cuts respectively to the pl_A and the pl_B at different ω levels. We can see that with ω decreasing, the $P_A(\omega)$ increases quickly. When ω is close to 0, it is almost certain that the $\Gamma_A(\omega)$ will cover the reference values. On contrast, the $P_B(\omega)$ is almost stable to 0, which can be explained by the fact that the $\Gamma_B(\omega)$ do not cover the reference values. There are two reasons of the different performances between the two methods. Firstly the positions of the subsets from the contour functions pl_A are closer to the reference values, and secondly, the subsets are larger.

5.3.1.4 Robustness with respect to material variability with reliable statistical factors

The discussion above concerns the scenario corresponding to multiple measurements to one specimen. Here, we verify the robustness with respect to material variability with the same statistical factors. 150 specimens are generated under the same statistical parameters as the one used to construct the basis vectors, and their displacement fields are measured. This simulation is extracted from a case where the material statistical factors are known and reliable, and the macro elastic properties are to be identified.

In order to isolate the effect of material variability, measurement noise is not added to measurement fields. The estimators $\widehat{\boldsymbol{\theta}}_A$ and $\widehat{\boldsymbol{\theta}}_B$ via maximising the contour functions pl_A and pl_B are shown in Fig. 5.12. The black stars are reference values corresponding to different specimens. It is clear that both the red squares and blue triangles distribution are larger than those in Fig. 5.9. The estimators $\widehat{\boldsymbol{\theta}}_A$ (red squares) are closer to the reference values (black stars) than the $\widehat{\boldsymbol{\theta}}_B$ (blue triangles).

Then, we calculate the distance d$\boldsymbol{\theta}$, between the estimators and their corresponding reference values. The histograms of the d$\boldsymbol{\theta}$ are shown in Fig. 5.13, which clearly shows that the $\widehat{\boldsymbol{\theta}}_A$ are closer to $\boldsymbol{\theta}_{ref}$ than $\widehat{\boldsymbol{\theta}}_B$. This means that the point estimators computed by maximising the contour functions pl_A are better than those obtained from pl_B.

We still plot the covering probability $P_A(\omega)$ and $P_B(\omega)$ of the cuts respectively to pl_A and pl_B at different ω-levels, as shown in Fig. 5.14. It is clear that the cuts from the contour functions pl_A are more likely to cover the reference values for any cutting levels. The reason is that contour functions pl_A are closer to reference values and the cuts of the contour functions pl_A are larger.

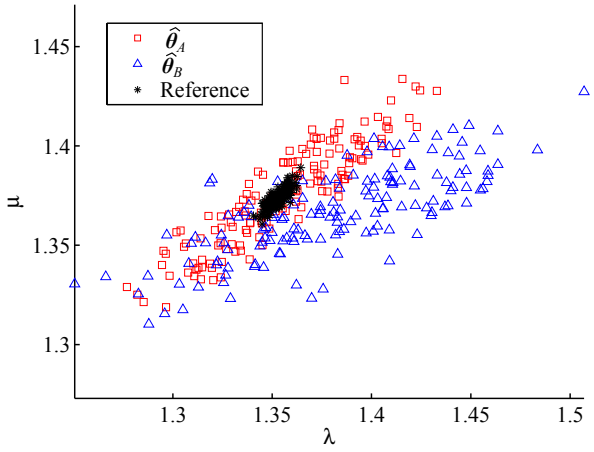

Fig. 5.12 Estimators from experimental measurements to different specimens

5.3.1.5 Robustness with respect to material variability with unreliable statistical factors

As the statistical factors come from experimental observations or prior information, they are uncertain. Especially for some new materials, their statistical factors come from empirical knowledge. Therefore, the robustness with respect to unreliable statistical factors should be studied. Considering a group of materials, we only have some unreliable knowledge about their statistical factors. Then, we can make use of the unreliable statistical factors to construct basis vectors and intervals to represent model uncertainty and to perform identification from measurement.

Table 5.2 Specimens with unreliable statistical factors

$A_r = 2.1, D_a \sim \mathcal{N}(0°, (10°)^2)$		$A_f = 0.45, D_a \sim \mathcal{N}(0°, (10°)^2)$		$A_f = 0.45, A_r = 2.1$
$A_f = 0.40$	$A_f = 0.50$	$A_r = 1.5$	$A_r = 2.5$	$D_a \sim \mathcal{N}(0°, (20°)^2)$
				 

As introduced in Section 4.1.3, three statistical factors are used to generate the heterogeneous materials: area fraction A_f, axis ratio A_r and degree of axis orientation D_a. The values $A_f = 0.45$, $A_r = 2.1$ and $D_a \sim \mathcal{N}(0°, (10°)^2)$ are used to construct basis vectors. Thus, we consider three scenarios in which the three factors are unreliable:

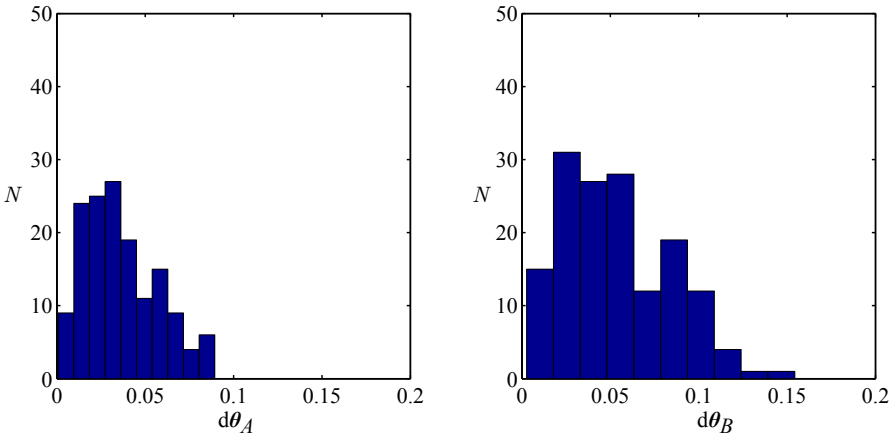

Fig. 5.13 Distance between estimators and reference values

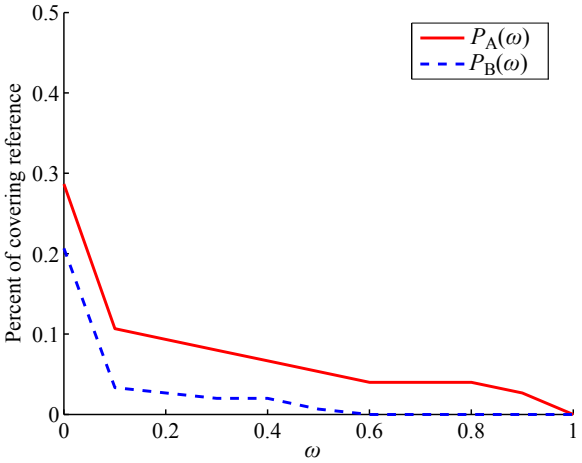

Fig. 5.14 Probability of covering the reference values at different ω-level cuts

- the area fraction $A_f = 0.45$ is unreliable; it is uniformly sampled from the interval $[0.40, 0.50]$;
- the particle axis ratio $A_r = 2.1$ is unreliable; it is uniformly sampled from the interval $[1.5, 2.5]$;
- the particle axis orientation degree $D_a \sim \mathcal{N}(0°, (10°)^2)$ is unreliable; it actually follows a Gaussian distribution with more randomness $\mathcal{N}(0°, (20°)^2)$;

Hence, perturbation between statistical factors constructing basis vectors and those generating measured specimens are induced. In Table 5.2, the first and second column

are specimens with perturbed A_f; the third and fourth column are specimens with perturbed A_r; the fifth and sixth column are specimens with more random D_a.

For each scenario, we generate 150 specimens and create the displacement measurements from reference the FEM calculations. Measurement noise is not added to the measurement fields to isolate the effect of unreliable statistical factors. The

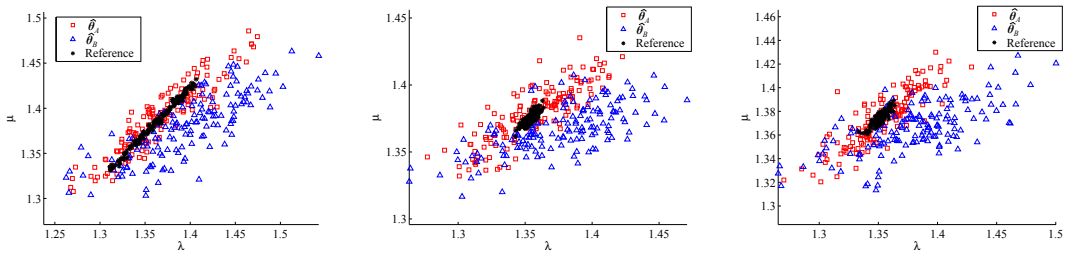

(a) Unreliable A_f (b) Unreliable A_r (c) Unreliable D_a

Fig. 5.15 Estimators under unreliable statistical factors

estimators via maximising the contour functions pl_A and pl_B are shown in Fig. 5.15. The black stars correspond to the reference values; the red squares are the estimators via maximizing the contour functions pl_A; the blue triangles are the estimators via maximizing the contour functions pl_B. Compared with the other two statistical factors, the unreliable A_f makes the reference values more scattered. In other words, the effective elastic properties are more sensitive to A_f. In all the three scenarios, the red squares are closer to the reference values than the blue triangles.

Then, we calculate the d$\boldsymbol{\theta}$ for each specimen; the histograms of d$\boldsymbol{\theta}$ are shown in Fig. 5.16. It clearly shows that the distances from the contour functions pl_A are smaller than those from the contour functions pl_B in all three scenarios.

Next, we plot the covering probability $P_A(\omega)$ and $P_B(\omega)$ of the cuts to the contour functions pl_A and pl_B at different ω-levels, as shown in Fig. 5.17. It is clear that, for all three scenarios, the cuts to the pl_A are more likely to cover the reference values at any ω-levels.

Based on the discussion above, we can conclude that with unreliable statistical factors, the estimators via maximising the contour functions pl_A are closer to the reference values than those obtained from the contour functions pl_B. The subsets from cutting the pl_A have higher probability of covering the reference values, because the subsets from cutting the pl_A are mostly larger than those obtained from the pl_B. Moreover, the robustness on unreliable statistical is very important for effective elastic

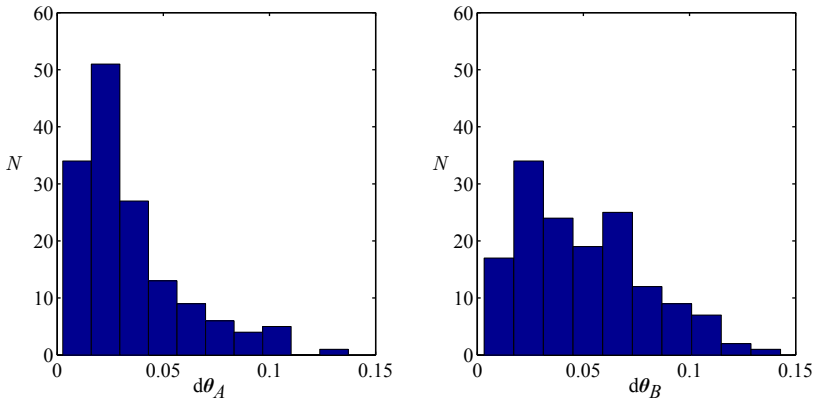

(a) Unreliable A_f

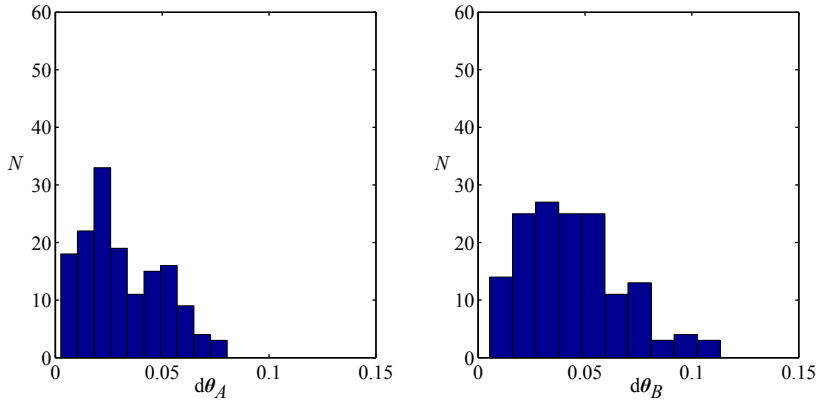

(b) Unreliable A_r

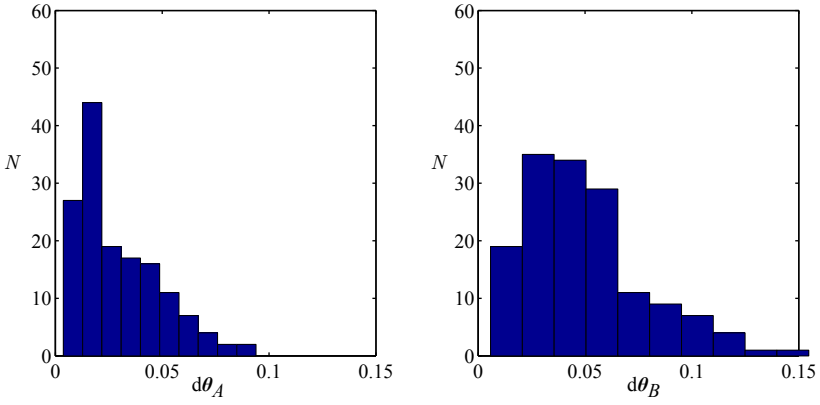

(c) Unreliable D_a

Fig. 5.16 Distance between estimators and reference values

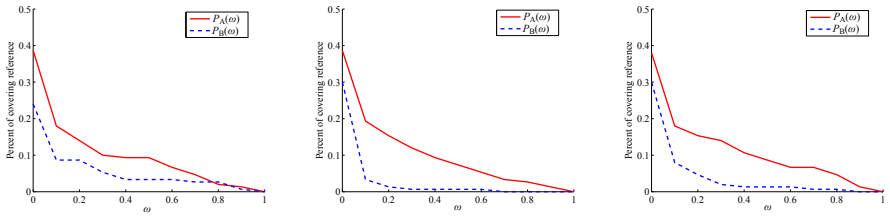

(a) Unreliable A_f (b) Unreliable A_r (c) Unreliable D_a

Fig. 5.17 Probability of covering the reference values at different ω-level cuts

parameter identification. When some statistical factors are missing, this advantage allows us to assume some factors to construct the basis vectors and intervals and then establish the contour functions.

5.3.2 Identifying micro-scale properties by macro-scale tests

5.3.2.1 Measurement and basis vectors

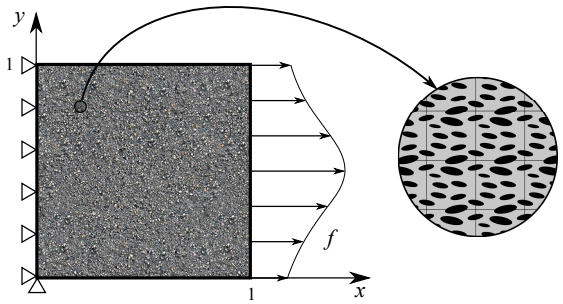

Fig. 5.18 Physical model of tests at macro-scale

In this section, we focus on the identification of the micro elastic properties from macro displacement measurement fields. Considering a 2D multi-structural plate as shown in Fig. 5.18. The left part of this figure is the macro-structure; it is considered as an homogeneous plate. Its elastic properties are obtained from the homogenization of the micro RVE structures (the right part of this figure) presented in Section 4.1.3. In this example, the RVEs are dual phase: the matrix phase (grey region) is denoted as material 1 and the reinforce phase (black region) is denoted as material 2. The RVEs are described by known statistical factors: $A_f = 45\%$; $A_r = 1.92$, and orientation degree D_a following $\mathcal{N}(0°, (10°)^2)$. We assume both material 1 and 2 are isotropic, linear elastic, undergoing small deformation. The relative reference values of elastic parameters are

the two Young modules $\boldsymbol{\theta}^{ref} = \{E_1^{ref}, E_2^{ref}\} = \{1, 2\}$, and the Poisson's ratio $\nu = 0.3$ is known. The plate is loaded on the right by a traction $\boldsymbol{f}$ whose horizontal projection is $\boldsymbol{f}_x = f_0 y(1-y)$ and vertical projection is null. The displacement measurement fields are created by FE^{2}M calculations as shown in Fig. 5.2.

In order to construct basis vectors $\boldsymbol{\Phi}$ and interval vectors $[\boldsymbol{\eta}]$ for interval displacement fields, $N = 50$ micro-structures are generated. Then effective elastic tensors ${}^h\boldsymbol{C}_j$, $j = 1, \cdots, N$, are calculated using the homogenization method. After performing a POD to ${}^h\boldsymbol{C}_j$, we can obtain the basis vectors $\boldsymbol{\chi}$ and their corresponding singular values $\boldsymbol{V} = \{\varrho_1, \cdots, \varrho_N\}$. To determine the number of basis vectors n_b, we still make use of the quantity $Ep_i = \varrho_i / \sum \varrho_i$. The quantities Ep of the first six basis vectors are shown in Fig. 5.19. We can see that the first three singular values correspond to the majority of the energy (89.84%). Fig. 5.19 implies that $n_b = 3$ is enough to reconstruct the interval fields.

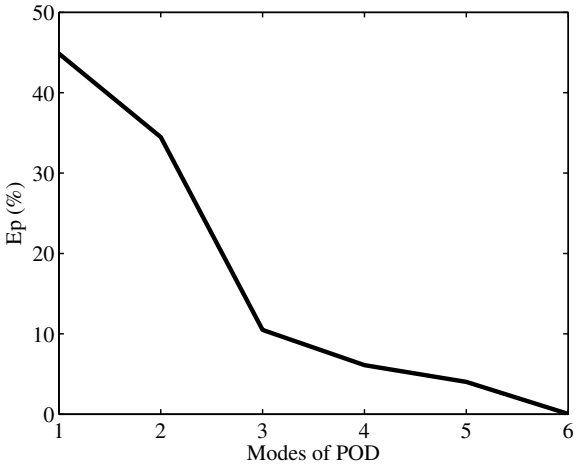

Fig. 5.19 Energy proportion Ep

Then, we plot the component distributions of both original and reconstructed elastic tensors as shown in Fig. 5.20 for the 50 initial micro-structures. In this figure, only the most important components C_{11} Vs C_{12}, C_{11} Vs C_{22} and C_{11} Vs C_{33} are illustrated. The other components are close to zero. We set the truncation number $n_b = 3$ to reconstruct the elastic tensors. We can see that the shapes of point distributions of the reconstructed tensors are similar to those of the corresponding original elastic tensors. This means that the dependence among the tensor components can be represented by the first three POD modes. Therefore, $n_b = 3$ is suitable to describe the interval elastics tensors.

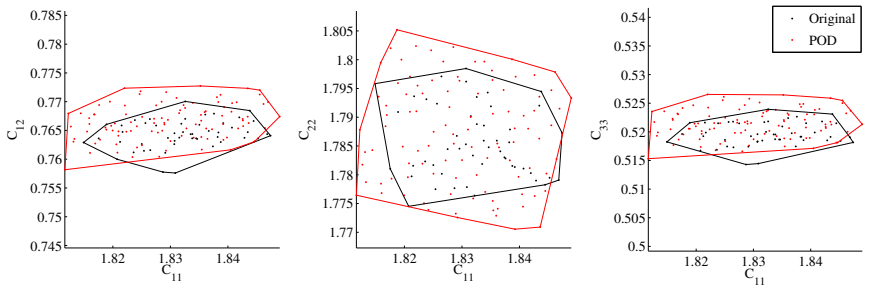

Fig. 5.20 Component distributions of original and reconstructed tensors

5.3.2.2 Identification results

An RVE with same statistical factors as those to construct the basis vectors is generated, as shown in Fig. 5.21, to be used as a reference micro-structure to create measurement fields. The measurement grids are 50×50 covering the whole plate, and a Gaussian white noise, whose standard deviation is 10% with respect to the average displacement value, is added to displacement fields to simulate measurement uncertainty. In order to simulate the extreme situation, the RVE structure is the same for all the calculation elements of the macro-structure during implementation. Thus, the reference micro-structure is unknown during identification, which will induce serious model uncertainty.

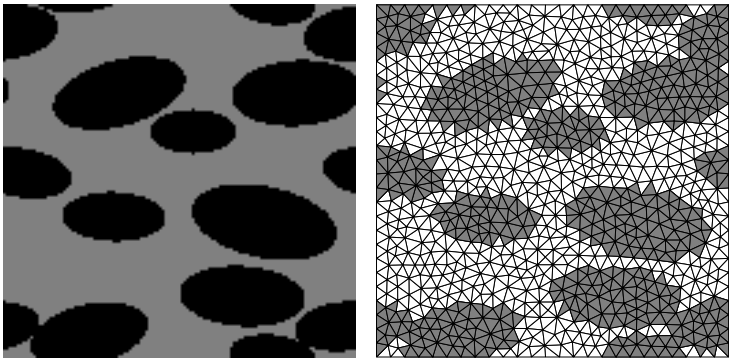

(a) Micro-structure material (b) Micro-structure mesh

Fig. 5.21 Micro-structure of the reference specimen

Similar to the example in Section 5.3.1, we note the proposed contour function from Eq. (4.31), based on an integrated likelihood function, as the contour function pl_A. The contour function pl_B serves as a comparison, and it is constructed by Eq. (4.29), based on a standard likelihood distribution. It should be noticed that a pre-set micro-structure should be proposed to establish the contour function pl_B. In this

example, the pre-set micro-structure used for the pl_B is shown in Fig. 5.22. We can see that this pre-set micro-structure is different from the reference micro-structure, even though they have been obtained with the same micro statistical factors.

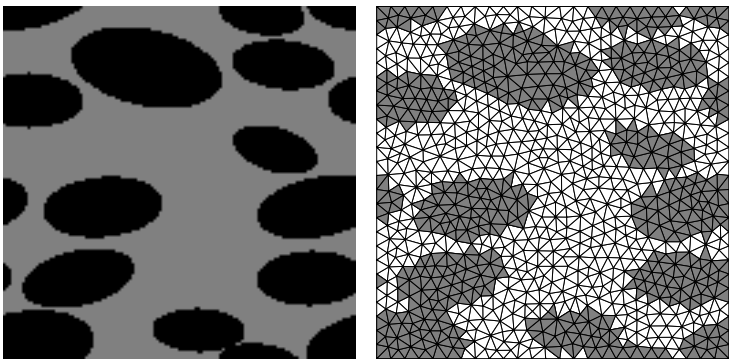

(a) Micro-structure material (b) Micro-structure mesh

Fig. 5.22 Pre-set Micro-structure for the contour function pl_B

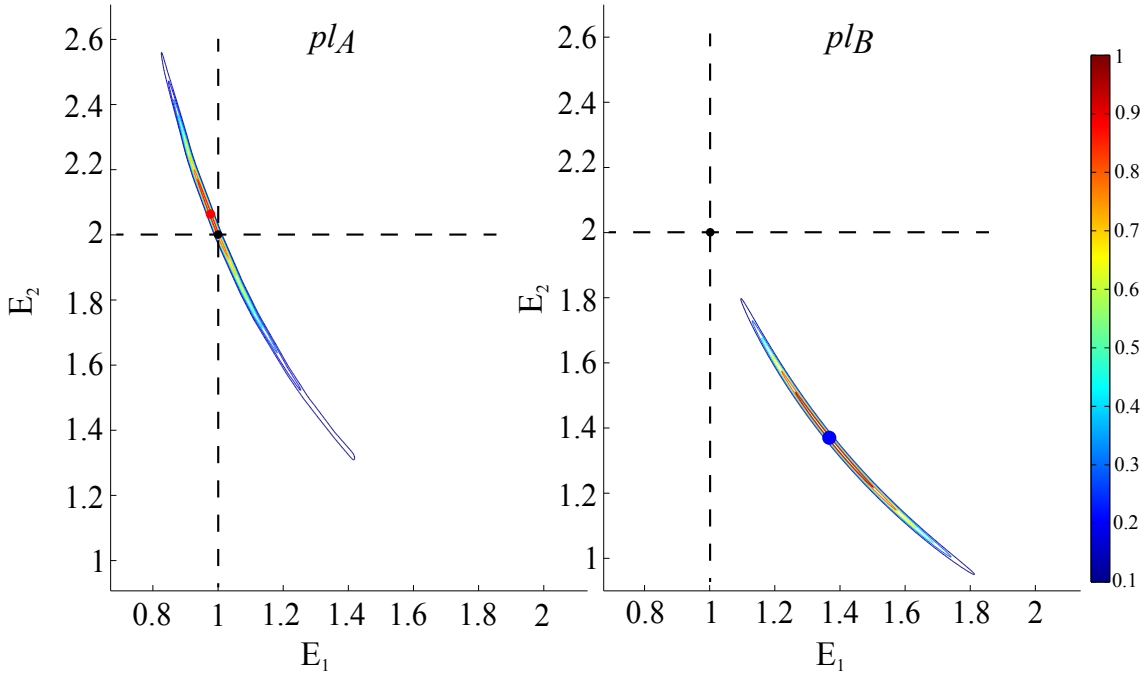

Fig. 5.23 Contour functions pl_A and pl_B based on the same measurement

Both contour functions pl_A and pl_B for one measurement are shown in Fig. 5.23. The cross points of the two dashed lines illustrate the reference values. We can see that the estimators $\widehat{\boldsymbol{\theta}}_A$ (red point) via maximising the contour function pl_A are closer

to the reference values than the $\widehat{\boldsymbol{\theta}}_B$ (blue point) via maximising the contour function pl_B. The ratios r_{Hes} defined in Eq. (5.50) are respectively 2.3×10^3 (contour function pl_A) and 3.5×10^3 (contour function pl_B) at the maximum points. This phenomenon can be explained by the fact that the contour function pl_A is less convergent than the contour function pl_B. The reason of different convergences is that the contour function pl_A takes more uncertainty (model uncertainty) into account than pl_B. The contour lines in Fig. 5.23 can be seen as the cuts to pl_A and pl_B at various ω-levels. Compared with the example in the section 5.3.1, the contour functions in this example are narrow and elongated in the parameter space. It is because the two micro-material elastic properties compensate each other on the macro response. The inverse problem is therefore not very well-posed.

5.3.2.3 Robustness with respect to measurement uncertainty

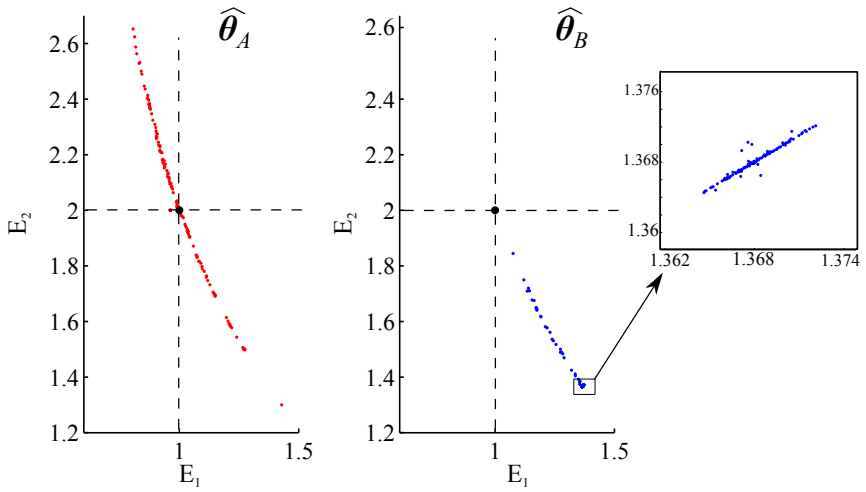

Fig. 5.24 Estimators from different measurements to one specimen

To study the robustness with respect to measurement uncertainty, 150 realisations of Gaussian noise with the same standard deviation as in Section 5.3.2.2 are generated, and they are added to the synthetic displacement field. This set-up corresponds to the situations of 150 experimental measurements with one simple specimen. Then, we estimate parameters $\widehat{\boldsymbol{\theta}}_A$ and $\widehat{\boldsymbol{\theta}}_B$ via maximising the contour functions pl_A and pl_B, respectively. The estimators are shown in Fig. 5.24. We can see that the $\widehat{\boldsymbol{\theta}}_A$ (red points) are more scattered than the $\widehat{\boldsymbol{\theta}}_B$ (blue points). The reason for the relatively small perturbation of blue points is that the measurement noise has smaller influence

on the estimators compared to the model uncertainty when the contour function pl_B is used for identification. On the other side, the red points are more scattered around the reference values located at the intersection of the two dashed lines. This property gives a potential of improving performance with multiple measurements. In order to clearly quantify the distance between the estimators and the reference values, we use the quantity $\mathrm{d}\boldsymbol{\theta}$ defined as follow:

$$\mathrm{d}\boldsymbol{\theta} = \sqrt{(\widehat{\mathrm{E}}_1 - \mathrm{E}_1^{\mathrm{ref}})^2 + (\widehat{\mathrm{E}}_2 - \mathrm{E}_2^{\mathrm{ref}})^2}, \tag{5.53}$$

to illustrate the distance between estimators and reference values. Fig. 5.25 gives the histograms of $\mathrm{d}\boldsymbol{\theta}_{\mathrm{A}}$ associated with the contour function pl_A and $\mathrm{d}\boldsymbol{\theta}_{\mathrm{B}}$ associated with the contour function pl_B. It is clear that the $\mathrm{d}\boldsymbol{\theta}_{\mathrm{A}}$ values are smaller than $\mathrm{d}\boldsymbol{\theta}_{\mathrm{B}}$. In this figure there are a lot of values of $\widehat{\boldsymbol{\theta}}_B$ located in the interval $[0.67, 0.73]$. These values coincide with the blue points concentrated in the small box in Fig. 5.24. Fig.

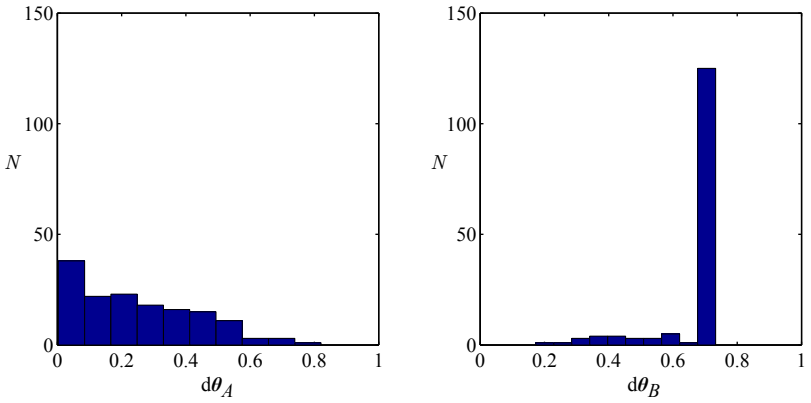

Fig. 5.25 Distance between estimators and reference values

5.26 shows the covering probabilities defined in Eq. (5.52). The quantities $P_A(\omega)$ and $P_B(\omega)$ are respectively the covering probabilities of the cuts to pl_A and pl_B at various ω-levels. We can see that with decreasing ω, the probability $P_A(\omega)$ increases quickly. When ω is close to 0, it is almost certain that the $\Gamma_A(\omega)$ will cover the reference values. On the contrary, $P_B(\omega)$ is close to 0 for most ω-levels. This means that $\Gamma_B(\omega)$ is not able to cover the reference values at corresponding ω-levels. Closer positions to the reference values and larger shapes are the two main reasons of the better performance of the contour functions pl_A.

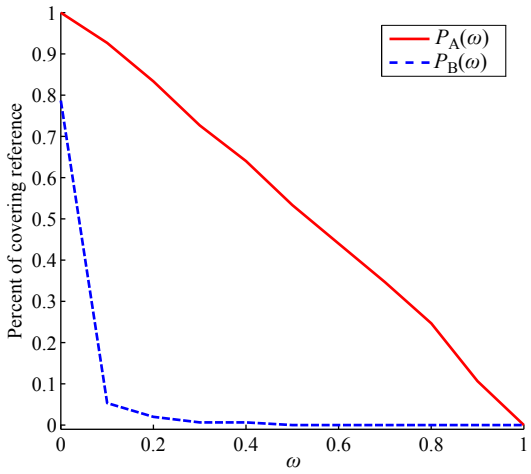

Fig. 5.26 Probability of covering the reference values at different ω-level cuts

5.3.2.4 Robustness with respect to material variability with reliable statistical factors

In this section, we will verify the robustness with respect to material variability under the same statistical factors. 150 specimens are generated with the same statistical parameters as constructing the basic vectors, and their displacement fields are measured. This simulation is extracted from a case in which the material statistical factors are known and the micro-scale elastic properties are identified.

In order to isolate the effect of material variability, measurement noise is not added to the measurement fields. The estimators $\widehat{\boldsymbol{\theta}}_A$ and $\widehat{\boldsymbol{\theta}}_B$ via maximising the contour functions pl_A and pl_B are shown in Fig. 5.27. The black points located at the cross of the two dashed lines are the reference values of the specimens. Compared with the perturbation caused by measurement error, the perturbation caused by material variability is more serious. It is clear that both $\widehat{\boldsymbol{\theta}}_A$ (red points) and $\widehat{\boldsymbol{\theta}}_B$ (blue points) have wider distributions than those in Fig. 5.24. However, the red points are still closer to the black points than the blue points.

In order to illustrate the distances between $\widehat{\boldsymbol{\theta}}_A$, $\widehat{\boldsymbol{\theta}}_B$ and $\boldsymbol{\theta}^{ref}$, we again calculate the quantity $\mathrm{d}\boldsymbol{\theta}$. The histograms of $\mathrm{d}\boldsymbol{\theta}_\mathrm{A}$ and $\mathrm{d}\boldsymbol{\theta}_\mathrm{B}$ are shown in Fig. 5.28. It is clear that $\widehat{\boldsymbol{\theta}}_A$ are closer to $\boldsymbol{\theta}^{ref}$ than $\widehat{\boldsymbol{\theta}}_B$. It can be explained by the fact that the point estimators via maximising the contour functions pl_A are better than those via maximising the pl_B.

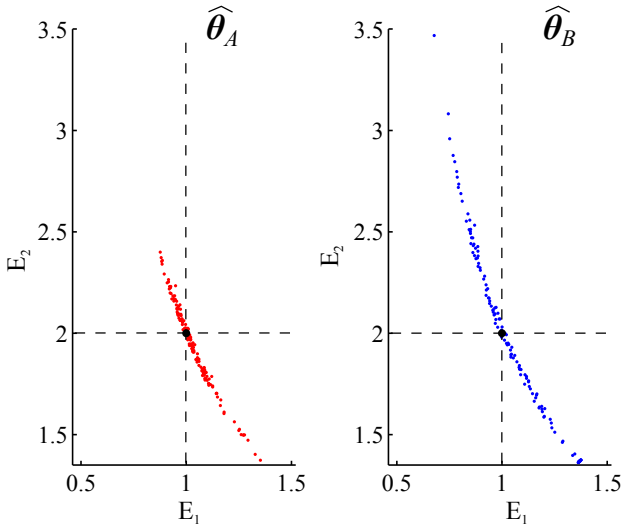

Fig. 5.27 Estimators from experimental measurements to different specimens

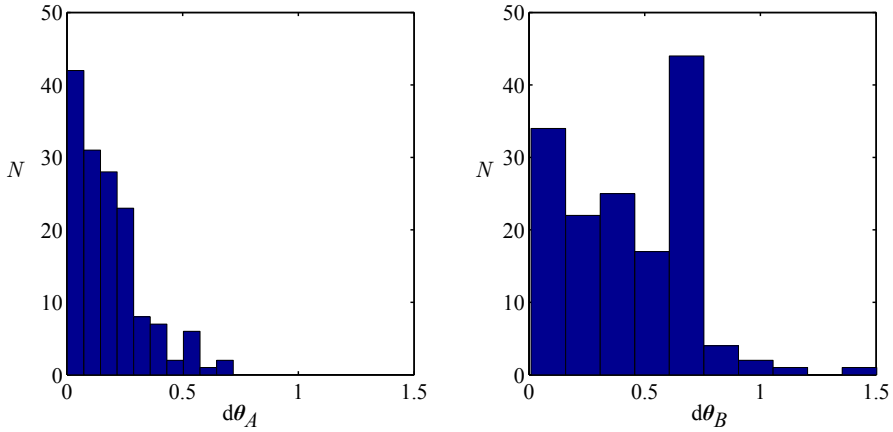

Fig. 5.28 Distance between estimators and reference values

We finally plot the covering probability $P_A(\omega)$ and $P_B(\omega)$ of the cuts to pl_A and pl_B at various ω-levels, as shown in Fig. 5.29. It is clear that the cuts of the contour function pl_A are more likely to cover the reference values for any cutting levels than those obtained from pl_B.

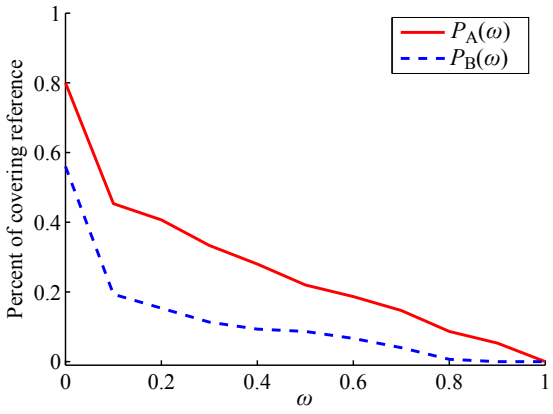

Fig. 5.29 Probability of covering the reference at different ω-level cuts

5.3.2.5 Robustness with respect to material variability with unreliable statistical factors

Similar to the example in Section 5.3.1.5, three scenarios in which the three factors (A_f, A_r, D_a) are unreliable are studied in this section. For each scenario, we generate 150 specimens and their loadings are simulated to create the measurements. The estimators $\widehat{\boldsymbol{\theta}}_A$ and $\widehat{\boldsymbol{\theta}}_B$ via maximising the contour functions pl_A and pl_B are shown in Fig. 5.30. The black points located at the cross of the two dashed lines are the reference values. We can see from Fig. 5.30 that $\boldsymbol{\theta}_B$ (blue points) are more spread than $\boldsymbol{\theta}_A$ (red points) in the case of unreliable statistical factors. The red points are closer to the reference values in all three scenarios.

Then we calculate the distance d$\boldsymbol{\theta}$ between the estimators and the reference values for each specimen. The histograms of d$\boldsymbol{\theta}_{\mathrm{A}}$ and d$\boldsymbol{\theta}_{\mathrm{B}}$ from the contour functions pl_A and pl_B are shown in Fig. 5.31. It clearly shows that the d$\boldsymbol{\theta}_{\mathrm{A}}$ are smaller than the d$\boldsymbol{\theta}_{\mathrm{B}}$ in all three scenarios.

Then we plot the covering probability $P_A(\omega)$ and $P_B(\omega)$ of the cuts of pl_A and pl_B at different ω-levels in Fig. 5.32. It is clear that for all three scenarios the cuts of the contour functions pl_A are more likely to cover the reference values at any cutting levels.

Based on the discussion above, we can summarise the robustness of our method in this application with unreliable statistical factors. The estimators via maximising the contour functions pl_A are closer to the reference values than those obtained from pl_B. The subsets from cutting the contour functions pl_A hold more possibility to cover the reference values. Overall, the improvement of pl_A is obvious as compared to pl_B.

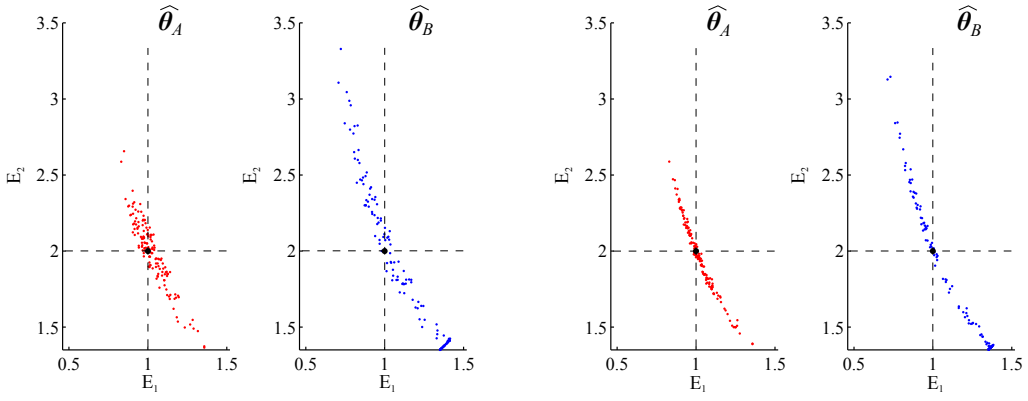

(a) Unreliable A_f

(b) Unreliable A_r

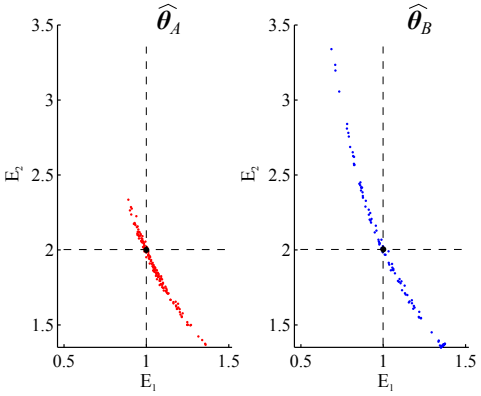

(c) Unreliable D_a

Fig. 5.30 Estimators under unreliable statistical factors

5.3.3 Conclusion

In this section, we took both measurement and model uncertainties into account in an identification problem. The measurement uncertainty was represented by probability distributions and the model uncertainty was represented by interval fields. We presented a POD-based approach for constructing basis vectors and interval vectors to model the model error. Both the measurement uncertainty and the model uncertainty were quantified by likelihood-based belief functions, in which contour functions were constructed based on integrated likelihood functions. Point estimators were proposed based on maximising the contour functions. The ω-level cuts to the contour functions were used to provide set-valued results.

It was shown that a few basis vectors were enough to construct the interval fields. The conservation of independent interval vectors was largely reduced. Meanwhile,

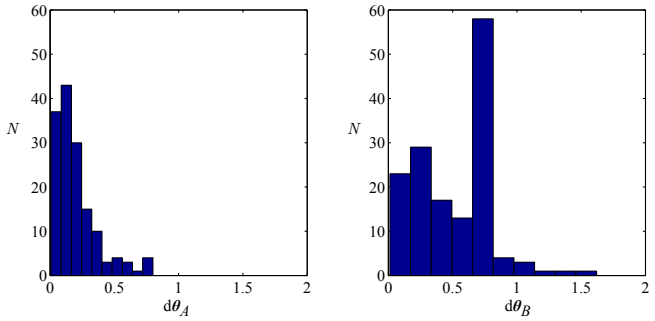

(a) Unreliable A_f

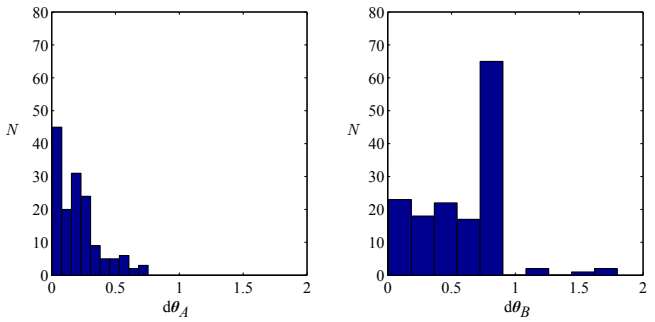

(b) Unreliable A_r

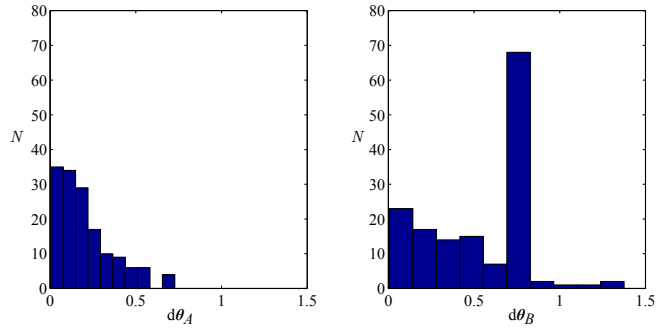

(c) Unreliable D_a

Fig. 5.31 Distance between estimators and reference values

the computational time for constructing the contour functions was reduced as well. Owing to accounting for the model uncertainty, the contour distributions were more spread than those constructed without considering the model uncertainty. Hence, the set-valued results obtained by cutting the contour functions at ω-levels were larger after taking the model uncertainty into account.

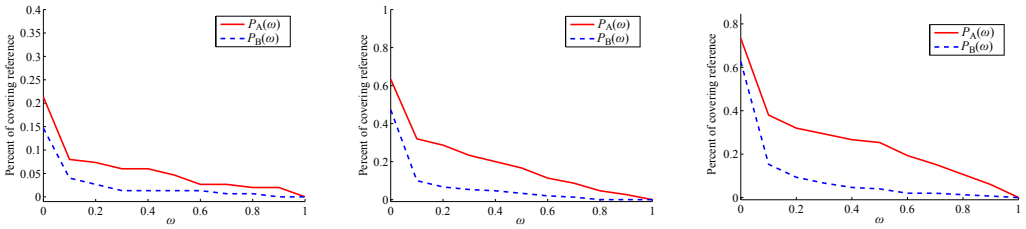

(a) Unreliable A_f (b) Unreliable A_r (c) Unreliable D_a

Fig. 5.32 Probability of covering the reference values at different ω-level cuts

For both numerical examples, the results have shown that the estimators via maximising contour functions with the model uncertainty were closer to the reference values. This advantage results in greater robustness even when the statistical factors are unreliable. Meanwhile, the ω-levels cuts to the contour functions with the model uncertainty were larger. As a result, they have a higher coverage probability. This advantage also contributes to the robustness of the method.

We can also see that the contour functions were elongated and narrow in the identification of micro-scale elastic parameters from macro-scale displacement fields related to the ill-posedness of the inverse problem. The ω-level cuts to the contour functions had a large span. In order to improve the performance of identification, we can take available prior information into consideration. The next chapter will focus on a methodology to take advantage of available prior information and simultaneously quantify its uncertainty.

Chapter 6

Identification taking prior information into consideration

6.1 Background and motivation

In Chapter 5, we have proposed a way to handle measurement and model uncertainties. Identification problems are mostly ill-posed, and uncertainty exacerbates the problems related to these issues (non-existence, non-uniqueness, and non-continuity). To overcome these issues, especially the non-uniqueness and non-continuity, it is beneficial to formulate and exploit available prior information. Nevertheless, the uncertainty of prior information is complex and heterogeneous due to its multiple sources. Hence, both the probabilistic approaches and the non-probabilistic approaches presented in Chapter 3, should be considered to encode the prior information uncertainty in different cases. Considering various prior information uncertainties and representation methods, it is necessary to develop a new strategy to exploit and merge all available information and quantify their uncertainty within a unified framework.

In this chapter, we face two challenges:

- taking the prior information into consideration;
- quantifying the heterogeneous uncertainties and propagating them.

The theory of belief functions constitutes an excellent framework to encode and quantify both epistemic uncertainty and aleatory uncertainty. Moreover, it has a comprehensive information fusion mechanism to perform combination and conditioning. Thus, we explore the possibility of using belief functions to take prior information into consideration for identification purposes.

6.2 Identification strategy

In our framework, the purpose of identification is to find the parameters $\boldsymbol{\theta} \in \boldsymbol{\Theta}$ that are the most compatible with all available information, taking into account uncertainty. As discussed in Chapter 1, the available information can be split into theoretical, experimental and empirical information. We have discussed how to handle the theoretical information and the experimental information using likelihood-based belief functions in Chapter 5. With the help of Eq. (5.1), the contour functions can be established using normalised and integrated likelihood function, denoted as $pl_L(\boldsymbol{\theta})$ in this chapter. The information uncertainty is quantified by the contour function $pl_L(\boldsymbol{\theta})$, which is equivalent to a possibility distributions and corresponds to a consonant random set. The contour function encodes the knowledge on $\boldsymbol{\theta}$ coming from the theoretical and experimental information. In this section, we will deal with the empirical information which is also called prior information.

6.2.1 Prior information

Prior information can be considered as background knowledge on the parameters $\boldsymbol{\theta}$ to be identified. It is often incomplete. Thus, the uncertainty on prior information is epistemic, and it can be represented by random sets. The random sets can be defined directly from subjective opinions or induced indirectly from other non-probabilistic approaches, e.g., possibility distributions or p-boxes as presented in Section 3.3.8.

In the belief functions framework, discounting operations allow us to express our degree of confidence in a source of information. Let us assume that, for instance, an expert uses the possibility distribution shown in Fig. 6.1 to represent their opinion on a parameter θ and we have a degree of confidence $m_{\boldsymbol{\Theta}} \in [0, 1]$ in this opinion. We can then assign the value $m_{\boldsymbol{\Theta}}$ to the whole set $\boldsymbol{\Theta}$, i.e.:

$$P(\{\omega \in \Omega | \Gamma(\omega) = \boldsymbol{\Theta}\}) = m_{\boldsymbol{\Theta}}, \tag{6.1}$$

where the mapping Γ is the ω-level cut and $0 \leq m_{\boldsymbol{\Theta}} \leq 1$. When $m_{\boldsymbol{\Theta}} = 0$, we fully trust the expert opinion; when $m_{\boldsymbol{\Theta}} = 1$, we totally doubt it. The discounted possibility distribution is shown in Fig. 6.2. We have finally a very versatile framework to describe prior information.

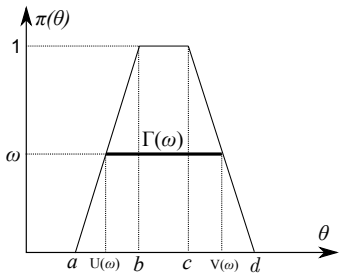

Fig. 6.1 Original possibility distribution

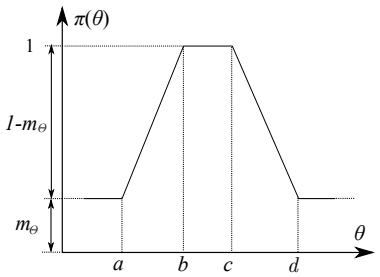

Fig. 6.2 Discounted possibility distribution

6.2.2 Information merging and posterior random set

Once all available pieces of information is defined, we have to merge them in order to construct posterior information. The product rule of possibility theory provides a combination mechanism by multiplying the possibility distributions and renormalising:

$$\pi_{1\oplus 2}(\boldsymbol{\theta}) = \frac{\pi_1(\boldsymbol{\theta})\pi_2(\boldsymbol{\theta})}{\sup_{\boldsymbol{\theta}} \pi_1(\boldsymbol{\theta})\pi_2(\boldsymbol{\theta})}. \tag{6.2}$$

However, this rule can only be used with possibility distributions (consonant belief functions), and it does not allow us to combine more general belief functions. Consequently, we should think about other methods to overcome this limitation. Three commonly used information merging methods have been presented in Section 3.3.7.2. Considering the purpose of identification, we can choose Dempster's rule to combine information. Because Dempster's rule concentrates information, it is suitable for searching the optimum values. In section 3.3.7.2, this rule was defined for finite sets. Here, we reformulate it in the infinite setting. Let us consider two random sets $(\Omega_k, \sigma_{\Omega_k}, P_k, \Gamma_k)$, $k = 1, 2$. Let $\Omega = \Omega_1 \times \Omega_2$ be the product space, $P = P_1 \otimes P_2$ the product measure on $\sigma_\Omega = \sigma_{\Omega_1} \otimes \sigma_{\Omega_2}$, and Γ_p the multi-valued mapping defined by: $\forall(\omega_1, \omega_2) \in \Omega_p$, $\Gamma_p(\omega_1, \omega_2) = \Gamma_1(\omega_1) \cap \Gamma_2(\omega_2)$. The combined random set is $(\Omega, \sigma_\Omega, P, \Gamma_p)$. We can call it the posterior random set. It induces the following belief and plausibility functions: for any $\boldsymbol{A} \subset \boldsymbol{\Theta}$,

$$Bel(\boldsymbol{A}) = \frac{P(\{(\omega_1, \omega_2) \in \Omega | \Gamma_p(\omega_1, \omega_2) \subseteq \boldsymbol{A}, \Gamma_p(\omega_1, \omega_2) \neq \emptyset\})}{P(\{(\omega_1, \omega_2) \in \Omega | \Gamma_p(\omega_1, \omega_2) \neq \emptyset\})}, \tag{6.3}$$

$$Pl(\boldsymbol{A}) = \frac{P(\{(\omega_1, \omega_2) \in \Omega | \Gamma_p(\omega_1, \omega_2) \cap \boldsymbol{A} \neq \emptyset\})}{P(\{(\omega_1, \omega_2) \in \Omega | \Gamma_p(\omega_1, \omega_2) \neq \emptyset\})}. \tag{6.4}$$

The degree of conflict is defined as:

$$k = P(\{(\omega_1, \omega_2) \in \Omega | \Gamma_p(\omega_1, \omega_2) = \emptyset\}). \tag{6.5}$$

It is a measure of the compatibility between the two sources of information. The product rule of possibility theory and Dempster's rule of belief functions framework are two different combination mechanisms. The product rule can be easily implemented but it has a limited scope, whereas Dempster's rule is more complex but more general. In this work we choose Dempster's rule to combine prior information with theoretical and experimental information.

We have presented the identification framework to take all available information into account and aggregate the information to construct posterior random sets. In order to implement this identification framework, attention should be paid to:

- the description approaches for multi-dimensional random sets;
- the numerical tools to implement Dempster's rule;
- the exploitation of posterior random sets.

6.3 Numerical implementation

In order to implement the proposed identification strategy, a Monte Carlo approach is considered, where the random sets are described through samples. We firstly have to choose a way to describe multi-dimensional random sets with arbitrary shapes, then implement Dempster's rule-based inference and explore the samples of posterior random sets.

6.3.1 Description of multi-dimensional random sets

Let us consider a 2D case to introduce the problem of description of multi-dimensional random sets. As shown in Fig. 3.1, an ω-level cut of a non-interactive joint possibility distribution of two variables can be expressed by a rectangle in $\mathbb{R}^2$. However, when the joint possibility distribution is interactive, the subsets from the ω-level cut may not be a rectangle as shown in Fig. 6.3. The shape of the subset is related to the dependence between the two variables. With increasing dimension, the interval representation will become more conservative. Moreover, the joint possibility distributions which come from likelihood-based belief functions are likely to be interactive. So we should find a strategy to describe domains with arbitrary shapes.

The methods to describe the multi-dimensional random sets should meet the following requirements:

- capability to describe arbitrary shapes;

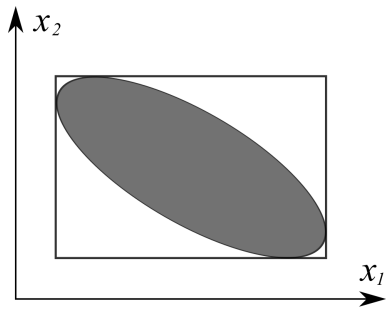

Fig. 6.3 Domain to be described

- easy and accessible construction;
- computational efficiency within belief function inference.

There are two main classes of approaches to describe a geometric domain. The first class of methods makes use of functions to parametrize a domain, e.g., regular shape functions (triangle, square, ellipsoid, etc.) and the level set method. The second class is based on discretization methods, which discretize a domain of interest into small subdivisions and define a geometric domain by assigning a value (1, -1 or 0) to a subdivision. Point clouds, belonging to the second class, are sets of data points in coordinate systems, which allow us to make detailed scans of complex objects [Mitra et al., 2004].

The parametrized function methods lead to difficult implementation of the Boolean operations, which are necessary for the implementation. There are three reasons for choosing point clouds to describe the domains. Firstly, the point clouds can be used to describe any domains in arbitrary dimensions with the help of indicator functions. Considering a domain $\boldsymbol{A} \subseteq \boldsymbol{\Omega}$, for any point $\boldsymbol{x}_i \in \boldsymbol{\Omega}$,

$$v_i = \begin{cases} 1 & \text{if } \boldsymbol{x}_i \in \boldsymbol{A}, \\ 0 & \text{if } \boldsymbol{x}_i \notin \boldsymbol{A}, \end{cases} \tag{6.6}$$

where $i = 1, 2, 3, \cdots$. Secondly, there are many methods and techniques to generate point clouds, including grid sequences, random sequences and quasi-random sequences. Thirdly, the intrinsic elements of point clouds are points which allow easily and fast Boolean operations. Boolean operations are necessary and inevitable to implement the inference based on belief functions (see Section 6.3.2).

Then, there are various techniques to generate point clouds. Regular grids have been applied historically on discretized general domains [Thompson et al., 1998]. The finer the grid is, the more accurate the discretization will be, but the higher the

computational and storage cost will be as well. Furthermore, for high-dimensional parameters spaces, the number of nodes of grid mesh tends to be unacceptable, due to the curse of dimensionality.

Random sequences from random sampling are another way to generate point clouds. It also requires computational effort in high-dimensional spaces. Latin hypercube sampling (LHS) [McKay et al., 1979] [Saliby and Pacheco, 2002] is a variance reduction technique, in which the selection of sample values is highly controlled, although still allowing them to vary. There is only one sample value in each segment of each dimension.

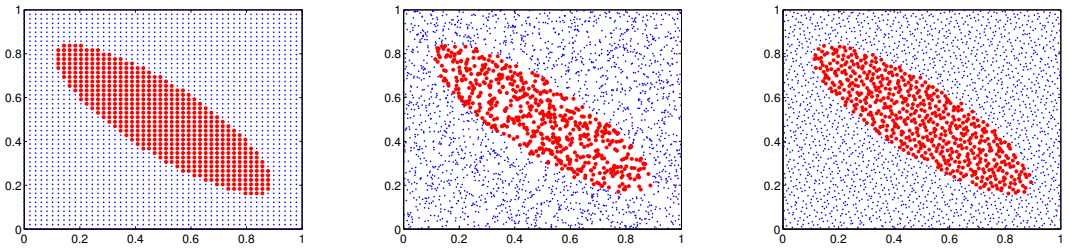

(a) Regular grid (b) Latin hypercube sampling (c) Halton sequence

Fig. 6.4 Ellipsoid described by point clouds

Quasi-random sequence methods [Caflisch, 1998] [Niederreiter, 2010] make use of deterministic low-discrepancy sequences to generate sampling points. The low-discrepancy sequences are usually more uniform than random ones. The use of low-discrepancy sequences makes quasi-random sequences perform better than the classic random sequences. Halton sequences [Halton, 1960] are particular low-discrepancy sequences and will be used in this work.

After generating point clouds, the domains are described by their discretized indicator functions defined by Eq. (6.6). Figure 6.4 presents a 2D ellipsoid described by point clouds generated by a regular grid, LHS, and a Halton sequence. We use the estimator of volume (surface) error to assess the point cloud performance:

$$\epsilon = \frac{|N_{in}/N_{total} - \mathcal{V}|}{\mathcal{V}}, \tag{6.7}$$

where N_{in} is the number of points inside the domain and N_{total} is the total number of points of the point cloud. The value $\mathcal{V}$ is the relative volume (surface) of the domain to be described with respect to the total volume described by the point cloud. One hundred ellipsoids (hyper-ellipsoids) with different sizes and orientations in 2D, 3D,

and 4D are described respectively by the point clouds generated by regular grids, LHS, and standard Halton sequences. The relations between the number of points and the error estimators are presented in Figs. 6.5, 6.6, and 6.7 for 2D, 3D and 4D cases respectively. We can see that the Halton sequences have the best performance in all three cases. Therefore, in this chapter, we will use point clouds generated using Halton sequences to describe random sets.

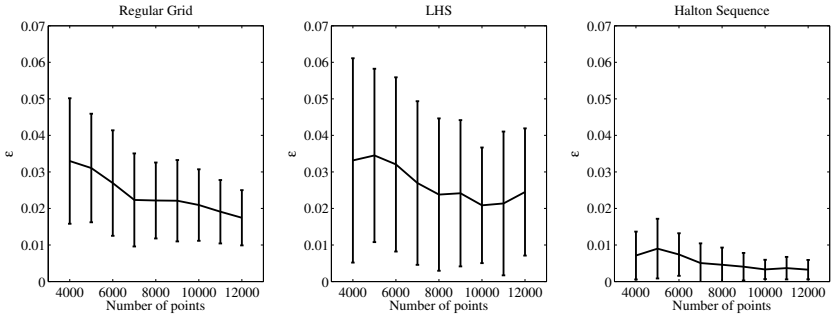

Fig. 6.5 Error Vs Point number: 2D

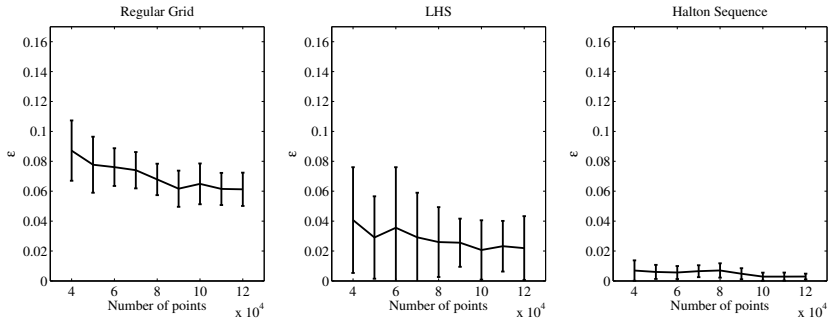

Fig. 6.6 Error Vs Point number: 3D

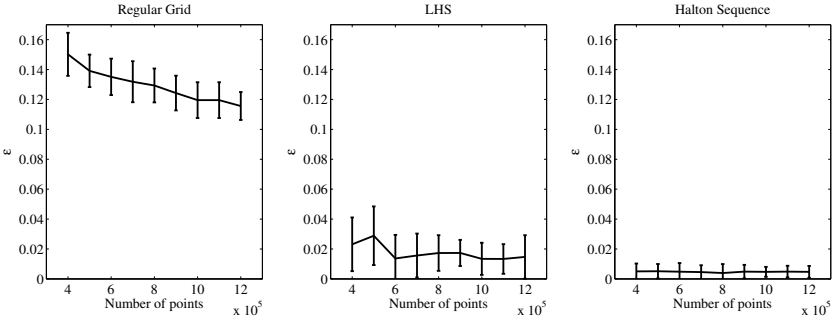

Fig. 6.7 Error Vs Point number: 4D

Point clouds are easy to manipulate. The coordinates of points can be stored in an $N \times D$ matrix $\boldsymbol{X}$, where N is the number of points, and D is the number of dimensions.

The values of the discretized indicator functions at each point of a domain can be stored in an $N \times 1$ vector $\boldsymbol{V}$. The Boolean operators between two domains can be implemented by performing Boolean operations on the components of their vectors.

6.3.2 Monte Carlo simulation of Dempster's rule

Dempster's rule can be implemented from samples based on Monte Carlo simulation and ω-level cuts. Here, we make use of two random sets induced from possibility distributions as an example to introduce the implementation of Dempster's rule. This method can be extended to random sets induced from other representation methods such as p-boxes. Considering two random variables $\omega_1 \in [0,1]$, $\omega_2 \in [0,1]$ and two possibility distributions $\pi_1(\boldsymbol{\theta})$ and $\pi_2(\boldsymbol{\theta})$ as shown in Fig. 6.8, the steps of the discrete inference are listed as follows:

- sample $\omega_1^1, \cdots, \omega_1^{N_s}$ from $[0,1]$ and sample $\omega_2^1, \cdots, \omega_2^{N_s}$ from $[0,1]$;
- cut $\pi_1(\boldsymbol{\theta})$ at ω_1^i level to obtain $\Gamma_1(\omega_1^i)$, and cut $\pi_2(\boldsymbol{\theta})$ at ω_2^i level to obtain $\Gamma_2(\omega_2^i)$ discretized using the point cloud, $i = 1, \cdots, N_s$;
- collect the non-empty posterior subsets $\Gamma_p(\omega_1^i, \omega_2^i) = \Gamma_1(\omega_1^i) \cap \Gamma_2(\omega_2^i) \neq \emptyset$, $i = 1, \cdots, N_s$.

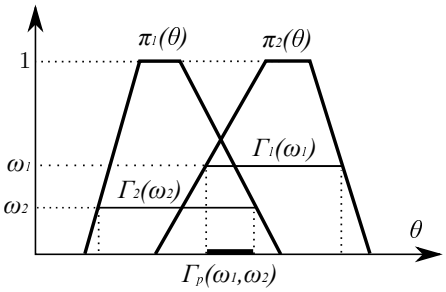

Fig. 6.8 Combine information by Dempster's rule

One question to address is to determine how many samples are sufficient to implement this Monte Carlo simulation. This problem is studied on the reconstruction of the posterior contour function on a scalar example. Consider two possibility distributions $\pi_1(\theta)$ and $\pi_2(\theta)$ as shown in Fig. 6.9. If both ω_1 and ω_2 follow a uniform distribution $\mathcal{U}([0,1])$, we have the following relation:

$$pl(\boldsymbol{\theta}) = \frac{\pi_1(\boldsymbol{\theta})\pi_2(\boldsymbol{\theta})}{p_0}, \tag{6.8}$$

where $pl(\boldsymbol{\theta}) = Pl(\{\boldsymbol{\theta}\})$ is the posterior plausibility of singleton $\boldsymbol{\theta}$ that can be expressed as follows:

$$pl(\boldsymbol{\theta}) = P\big(\big\{\omega_1 \times \omega_2 \in \Omega_p \big| \big[\Gamma_1(\omega_1) \cap \Gamma_2(\omega_2)\big] \cap \{\boldsymbol{\theta}\} \neq \emptyset\big\}\big), \tag{6.9}$$

and $p_0 = P(\{\omega_1 \times \omega_2 \in \Omega_1 \times \Omega_2 | [\Gamma_1(\omega_1) \cap \Gamma_2(\omega_2)] \neq \emptyset\})$ is a constant. We can make

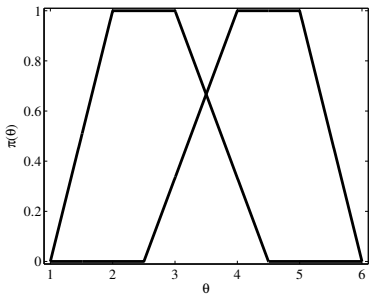

Fig. 6.9 Possibility distribution to be combined

use of Eq. (6.8) to evaluate the numerical error in the application of Monte Carlo simulation. The value p_0 and $pl(\theta)$ can be estimated as:

$$\widehat{pl}(\theta) = \frac{\#\{1 \leq i \leq N_s | \theta \in \Gamma_p^i\}}{N_{s-\emptyset}}, \quad \widehat{p_0} = \frac{N_{s-\emptyset}}{N_s}, \tag{6.10}$$

where Γ_p^i is the i-th subset, $N_{s-\emptyset}$ is the number of non-empty subsets. The relative numerical error can be written as:

$$\epsilon_{MC} = \frac{\int |\widehat{p_0}\widehat{pl}(\theta) - \pi_1(\theta)\pi_2(\theta)| \mathrm{d}\theta}{\max \pi_1(\theta)\pi_2(\theta)}. \tag{6.11}$$

Eq. (6.11) can be calculated by numerical integration using the rectangle rule. Samples of each size are drawn 10 times. The errors as functions of sampling sizes are shown in Fig. 6.10. The curve corresponds to the mean values of the errors; the vertical intervals represent the standard deviations. As seen in this figure, the error is small when the sampling number is larger than 5000. The accuracy will not improve significantly once the sampling size is above 1×10^4.

6.3.3 Exploring posterior random sets

We apply Monte Carlo simulation to implement Dempster's rule to combine information yielding set samples according to the posterior random set. After that, the

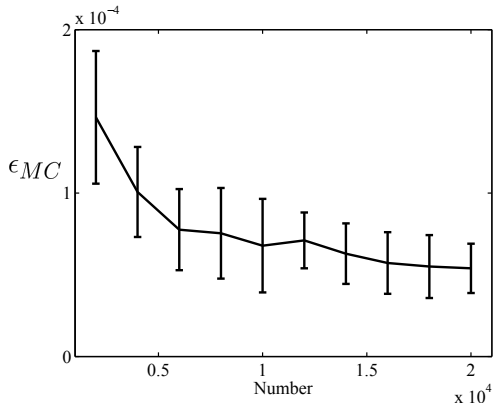

Fig. 6.10 Numerical error of Monte Carlo Sampling

posterior random set needs to be exploited. There are several ways to take advantage of the posterior random set:

- construct the posterior contour functions denoted as $pl_P(\boldsymbol{\theta})$, where $\boldsymbol{\theta} \in \boldsymbol{\Theta}$ is the parameters to be identified;
- search for the maximum of $pl_P(\boldsymbol{\theta})$;
- search the minimum-size subset with large enough Bel and Pl values;
- marginalization of pl_P, Bel and Pl;
- calculation of Bel and Pl of any subsets $\boldsymbol{A} \subseteq \boldsymbol{\Theta}$.

In most identification cases, we focus on the first three problems. When the number of parameters is larger than 2, we also need to compute the marginals to visualise the results.

6.3.3.1 Posterior contour function

The construction of the posterior contour functions $pl_P(\boldsymbol{\theta})$ is an easy and direct way to explore the posterior information from the set samples. It is computed based on Eq. (6.10). Greater $pl_P(\boldsymbol{\theta})$ value corresponds to more possible $\boldsymbol{\theta}$. Consequently, the $\boldsymbol{\theta}$ at which $pl_P(\boldsymbol{\theta})$ is the greatest is the most possible value. Therefore, the equation:

$$\widehat{\boldsymbol{\theta}}_P = \arg\max_{\boldsymbol{\theta}\in\boldsymbol{\Theta}} pl_P(\boldsymbol{\theta}), \tag{6.12}$$

can serve as a deterministic identification method to search for optimal values.

6.3.3.2 Optimal subset with given Bl and Pl thresholds

To continue the exploitation of the posterior random set samples, we can find a subset minimal size $\boldsymbol{R} \subseteq \boldsymbol{\Theta}$ with $Pl(\boldsymbol{R})$ and $Bel(\boldsymbol{R})$ larger than pre-set threshold values δ_{Pl} and δ_{Bel}. This problem can be formalized as follows:

$$\widehat{\boldsymbol{R}} = \arg\min_{\boldsymbol{R}\subseteq\boldsymbol{\Theta}} \mathcal{V}(\boldsymbol{R}), \quad \mathcal{V}(\boldsymbol{R}) = \int_{\boldsymbol{R}} d\boldsymbol{\theta}, \tag{6.13}$$

subject to:

$$\begin{cases} Pl(\boldsymbol{R}) & \geq & \delta_{Pl}, \\ Bel(\boldsymbol{R}) & \geq & \delta_{Bel}, \end{cases}$$

where $\mathcal{V}(\boldsymbol{R})$ is the volume of $\boldsymbol{R}$. Because this is a constrained optimization problem, we can use a penalty method to transform it into an unconstrained one. The reformulation of the optimization problem can be written as:

$$\widehat{\boldsymbol{R}} = \arg\min_{\boldsymbol{R}\subseteq\boldsymbol{\Theta}} \mathcal{V}'(\boldsymbol{R}), \tag{6.14}$$

where

$$\mathcal{V}'(\boldsymbol{R}) = \mathcal{V}(\boldsymbol{R}) + \varrho_{Pl} * \varphi\big(\delta_{Pl} - Pl(\boldsymbol{R})\big) + \varrho_{Bel} * \varphi\big(\delta_{Bel} - Bel(\boldsymbol{R})\big).$$

The quantities ϱ_{Pl} and ϱ_{Bel} are the penalty coefficients which should be large numbers, i.e., 1×10^3 in this chapter. The function $\varphi(t)$ is a penalty function defined as:

$$\varphi(t) = \max(0, t). \tag{6.15}$$

In order to solve Eq. (6.14), the parametrization of $\boldsymbol{R}$ is a necessary step. There are two clear choices for the parametrization of $\boldsymbol{R}$: (1) by regular shape (ellipsoid, rectangle,...) and (2) by point clouds. The first choice needs increasing parameters with increasing dimensions, and the shapes of result domains must be regular. Parametrization of $\boldsymbol{R}$ using point clouds requires too many parameters. Beyond these two choices, we propose to reparametrize $\boldsymbol{R}$ based on the POD basis vectors from samples of the posterior random sets. This approach can give us domains with similar shapes as the samples of the posterior random sets. The number of parameters does not depend on dimension but on the number of basis vectors. The samples of the posterior random sets can be considered as a group of snapshots by storing their discrete indicator functions as vectors $\boldsymbol{v}_i$ of size N, the number of points for $i = 1, 2, 3, \cdots, M$, where M

is the number of samples from the posterior random sets. Then the $N \times M$ matrix of snapshots is written as follows:

$$\boldsymbol{V} = [\boldsymbol{v}_1 \ \cdots \ \boldsymbol{v}_M]. \tag{6.16}$$

Denoting by γ_i the eigenvalues of $(\boldsymbol{V} - \overline{\boldsymbol{v}})^T(\boldsymbol{V} - \overline{\boldsymbol{v}})$, with correspondingly eigenvectors $\boldsymbol{\phi}_i$, where

$$\overline{\boldsymbol{v}} = \frac{1}{M}\sum_{i=1}^{M} \boldsymbol{v}_i, \tag{6.17}$$

then $\boldsymbol{\varphi}_i = (\boldsymbol{V} - \overline{\boldsymbol{v}})\boldsymbol{\phi}_i$ is the i-th POD basis vector. The target subsets can be parametrized through their discrete indicator functions decomposed on the POD basis vectors:

$$\boldsymbol{v}^{POD} = \mathbf{1}_\delta\big(\overline{\boldsymbol{v}} + \sum_{k=1}^{n} \alpha_k \boldsymbol{\varphi}_k\big), \tag{6.18}$$

where $\mathbf{1}_\delta$ is a threshold function to ensure $\boldsymbol{v}^{POD}$ corresponds to an indicator function:

$$\mathbf{1}_\delta(v_i) = \begin{cases} 1 & \text{if } v_i \geq \delta, \\ 0 & \text{otherwise.} \end{cases} \tag{6.19}$$

The number n of basis vectors is determined based on the energy proportion of POD modes. Finally, Eq. (6.14) is transformed into a minimization with regard to $(\alpha_1, \cdots, \alpha_n)$:

$$(\widehat{\alpha}_1, \cdots, \widehat{\alpha}_n) = \arg \min_{(\alpha_1, \cdots, \alpha_n)} \mathcal{V}'\big(\boldsymbol{v}^{POD}(\alpha_1, \cdots, \alpha_n)\big). \tag{6.20}$$

6.4 Numerical Application

In this section, we present three numerical examples in which prior information is taken into consideration. The first example deals with the identification of elastic properties of a homogeneous 2D plate under loading. Classical Bayesian inference is used as a comparison. The second example is concerned with the identification of elastic properties of a heterogeneous 2D plate under loading. The third example addresses the identification of micro-scale elastic properties from a macro-scale test.

6.4.1 Identifying homogeneous material

The elastic properties of a 2D homogeneous plate as shown in Fig. 6.11(a) need to be identified. The mechanical behaviour of the plate is governed by Eqs. (4.1)-(4.3).

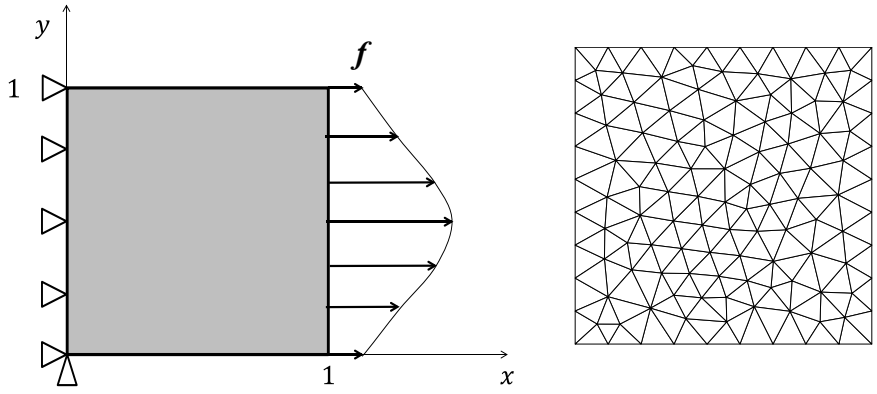

(a) Physical model (b) FE mesh

Fig. 6.11 Homogeneous plate

We particularize Eq. (4.3) for an isotropic material as:

$$\boldsymbol{\sigma} = \lambda tr(\boldsymbol{\varepsilon})\boldsymbol{I} + 2\mu\boldsymbol{\varepsilon} \quad \text{in all the domain,} \tag{6.21}$$

where $\boldsymbol{I}$ denotes the identity matrix and $tr(\boldsymbol{A})$ is the trace of matrix $\boldsymbol{A}$. The parameters $\boldsymbol{\theta} = \{\lambda, \mu\}$ are the two Lamé parameters determining the plate elastic properties. The plate is fixed on the left side and loaded on the right by a traction $\boldsymbol{f}$ whose horizontal projection is $\boldsymbol{f}_x = f_0 y(1-y)$ and vertical projection is null. The relative reference values are $\{\lambda_{ref}, \mu_{ref}\} = \{1, 1\}$.

6.4.1.1 Measurement and prior information

We use synthetic displacements from a reference finite element analysis, as shown in Fig. 6.11(b), as measurement values. The measurement grids are 10×10 covering the whole plate, and a Gaussian white noise is added to simulate measurement error. The standard deviation of noise is 5% with respect to the maximum displacement value. Based on Eq. (4.29), the uncertainty about $\boldsymbol{\theta}$ from the measurements is represented by a consonant likelihood-based belief function, whose contour function equals the normalized likelihood function.

The prior information, from expert opinions, is expressed by possibility distributions, denoted as π. In order to check the performance of this approach, two scenarios are considered. In the first scenario, the expert opinions are relatively correct, hence the possibility distributions are close to the reference values and plotted with solid lines in Fig. 6.12. In the second scenario, the expert opinions are wrong, the possibility

distributions do not cover the reference values, and are plotted with dashed lines in Fig. 6.12. Then, we take a degree of confidence (or belief, or trust) into account. Assume we have 80% confidence in the expert opinions for both scenarios. Based on the introduction in Section 6.2.1, the possibility distributions of both scenarios are transformed into the distributions shown in Fig. 6.13.

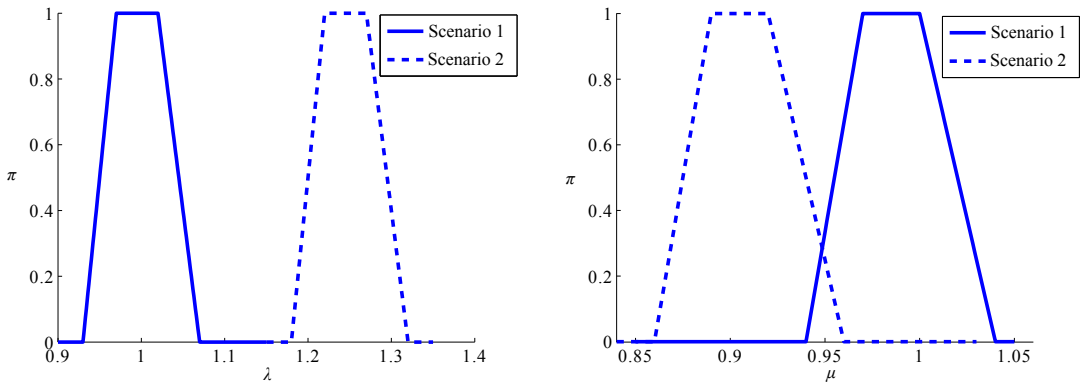

(a) Prior possibility distribution on λ (b) Prior possibility distribution on μ

Fig. 6.12 Prior information expressed using possibility distributions

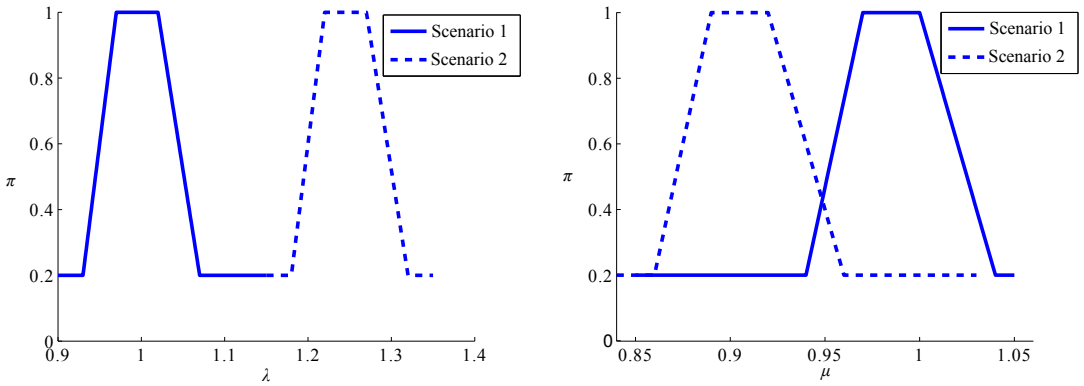

(a) Prior possibility distribution on λ (b) Prior possibility distribution on μ

Fig. 6.13 Discounted Possibility distributions

Because there is no other information, we can reasonably assume that the two parameters are non-interactive. Using Eq. (3.25), we can construct a joint possibility distribution about λ and μ shown as the square contour lines in Fig. 6.14 and 6.15. It is clear that the prior possibility distribution in the second scenario is far from the reference values and cannot provide any valuable correction. The ellipsoid contour

lines in Fig. 6.14 and 6.15 are contour functions pl_L, which represent the theoretical and measurement information.

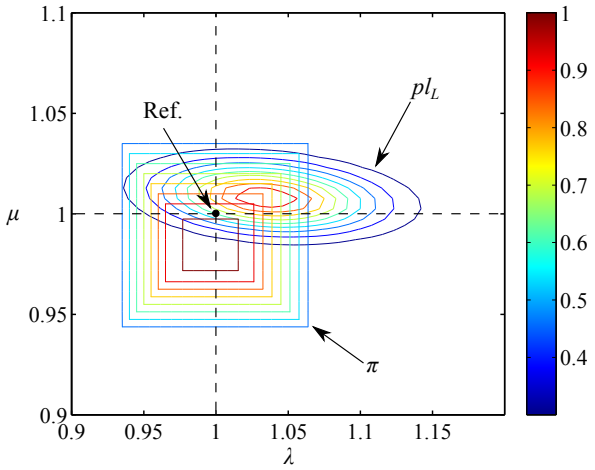

Fig. 6.14 Scenario 1: π and pl_L

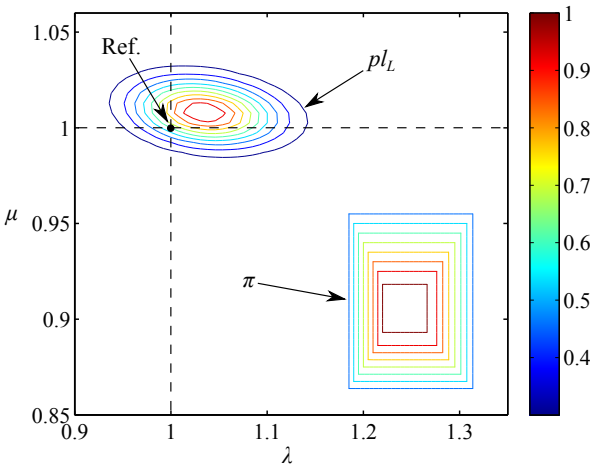

Fig. 6.15 Scenario 2: π and pl_L

6.4.1.2 Information merging

Dempster's rule detailed in Section 6.3.2 is chosen to combine the contour functions pl_L and the possibility distributions π. We uniformly take N_s samples from $[0,1]\times[0,1]$ to compute ω-level cuts to pl_L and π. After cutting the two distributions and intersecting

the two groups of subsets, we obtain $N_{S-\emptyset}$ non-empty the samples of posterior random set denoted as $\{\Gamma_p^i\}$, $i = 1, ..., N_{s-\emptyset}$. Then the degree of conflict of each scenario can be estimated by the following:

$$\widehat{k} = \frac{N_s - N_{s-\emptyset}}{N_s}. \tag{6.22}$$

The degree of conflict in scenario 1 is $\widehat{k}_1 = \dfrac{10000 - 9796}{10000} = 0.0204$; the one in scenario 2 is $\widehat{k}_2 = \dfrac{10000 - 2004}{10000} = 0.7996$. If the degree of conflict k is too large, it can indicate that at least one source of information is likely to provide wrong information. The value $\widehat{k}_2$ in scenario 2 is similar to the degree of confidence assigned to the prior information. It reflects the fact that measurement information only overlaps the total set that we add to express our disbelief in this expert opinions. In other words, there is no overlap between the pl_L and the original possibility distributions. Considering the big conflict in scenario 2, it is reasonable to consider there is at least one false information.

The value $\widehat{pl}_P$ in Eq. (6.23) is used as an estimator of the posterior contour functions:

$$\widehat{pl}_P(\boldsymbol{\theta}) = \frac{\#\{1 \le i \le N_{s-\emptyset} | \boldsymbol{\theta} \in \Gamma_p^i\}}{N_{s-\emptyset}}. \tag{6.23}$$

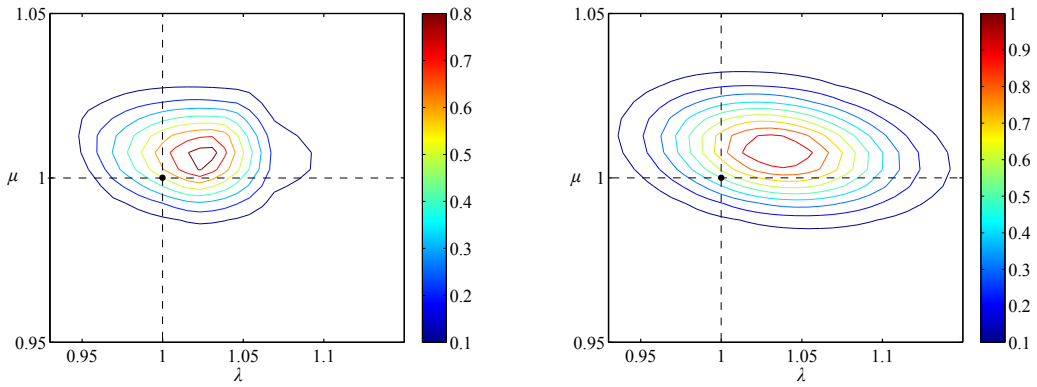

(a) pl_P in scenarios 1 (b) pl_P in scenarios 2

Fig. 6.16 Contour functions of posterior random sets

The posterior contour functions of the two scenarios are shown in Fig. 6.16. The value $\widehat{\boldsymbol{\theta}}_P$ at which pl_P is maximum can be used as a point estimator. In scenario 1, $\widehat{\boldsymbol{\theta}}_P = \{1.0275, 1.0063\}$; in scenario 2, $\widehat{\boldsymbol{\theta}}_P = \{1.0344, 1.0082\}$. We can see that, due to

the correct prior information in scenario 1, $\widehat{\boldsymbol{\theta}}_P$ in scenario 1 is closer to the reference values.

6.4.1.3 Comparison with Bayesian inference

In order to demonstrate the advantages of the inference based on the theory of belief functions, we use Bayesian inference to deal with the same information:

- prior information is expressed as a subjective probability density function (PDF) $p(\boldsymbol{\theta})$;
- measurement information is encoded by the likelihood function $L(\boldsymbol{\theta}; \widetilde{\boldsymbol{U}})$;
- information is merged by the Bayes' rule:

$$p(\boldsymbol{\theta}|\widetilde{\boldsymbol{U}}) = cp(\boldsymbol{\theta})L(\boldsymbol{\theta}; \widetilde{\boldsymbol{U}}), \tag{6.24}$$

where $p(\boldsymbol{\theta}|\widetilde{\boldsymbol{U}})$ is the posterior probability function, c is the normalising constant defined as:

$$\frac{1}{c} = \int_{\boldsymbol{\Theta}} p(\boldsymbol{\theta})L(\boldsymbol{\theta}; \widetilde{\boldsymbol{U}})\mathrm{d}\boldsymbol{\theta}. \tag{6.25}$$

In this example, the prior information was first proposed in terms of possibility distributions. In order to apply a Bayesian inference, they are transformed into Gaussian PDFs $p(\boldsymbol{\theta})$. The mean of $\boldsymbol{\theta}$ following $p(\boldsymbol{\theta})$ is the middle value of the core of the possibility distribution. In order to encode our degree of confidence in the prior information, the standard deviations of $p(\boldsymbol{\theta})$ should be such that $P(Supp) = 1 - m(\boldsymbol{\Theta})$, where $Supp$ is the support of the possibility distribution.

The marginal distributions of prior PDFs, posterior PDFs, and likelihood functions are shown in Fig. 6.17 (scenario 1) and Fig. 6.18 (scenario 2). The marginals of π, pl_L and pl_P are calculated based on Eq. (3.24) and shown in Fig. 6.19 (scenario 1) and Fig. 6.20 (scenario 2). We can see that, in scenario 1, both the posterior PDFs of Bayesian inference and the posterior contour functions of belief functions framework move towards the reference values. However, in scenario 2, the prior information is relatively wrong, and the two methods display different results. The posterior PDFs of Bayesian inference still averages the two informations. The wrong prior information (blue dashed-dotted curve in Fig. 6.18) affects the measurement information. As a consequence, the combined information $p(\boldsymbol{\theta}|\widetilde{\boldsymbol{U}})$ is worse than the likelihood $L(\boldsymbol{\theta}; \widetilde{\boldsymbol{U}})$. In contrast, a degree of confidence is added to prior information in the inference based on the theory of belief functions. Hence, the posterior contour function pl_P remains

stable. The contour function pl_P is at least not worse than the contour function pl_L. The reason why pl_P remains stable is that when we associate a degree of confidence with the prior information. We do no further assumption: we just associate a degree of confidence to the whole set $\boldsymbol{\Theta}$.

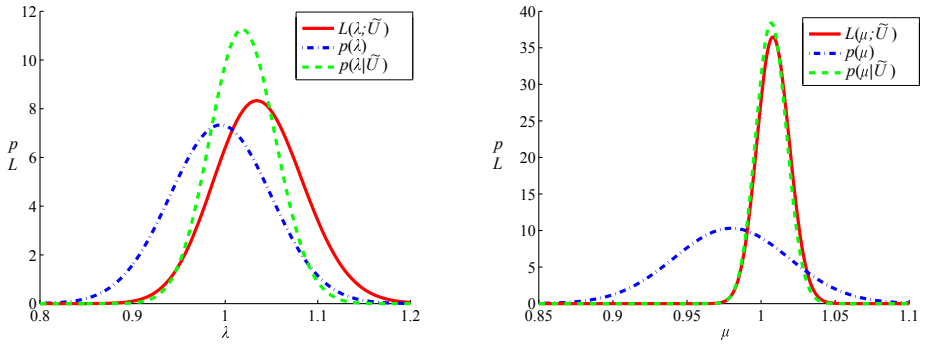

(a) Marginalisation on λ (b) Marginalisation on μ

Fig. 6.17 Marginal probability density distributions in scenario 1

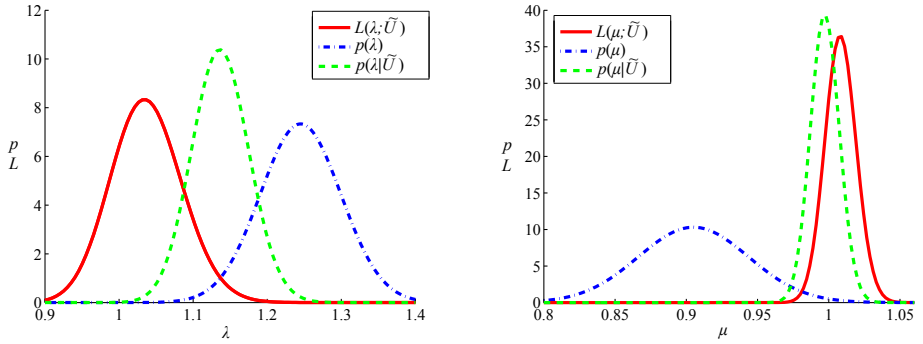

(a) Marginalisation on λ (b) Marginalisation on μ

Fig. 6.18 Marginal probability density distributions in scenario 2

6.4.1.4 Exploration of the posterior random sets

For further exploitation of the posterior random set, we focus on finding a minimum subset $\boldsymbol{R}$ described by its discrete indicator functions $\boldsymbol{v}^{POD}$ with $Pl(\boldsymbol{v}^{POD})$ and $Bel(\boldsymbol{v}^{POD})$ larger than given threshold values δ_{Bel} and δ_{Pl}. As explained in Section 6.3.3.2, we make use of the basis vectors of the POD for the samples of posterior random set to parametrize $\boldsymbol{v}^{POD}$. Then, we need to determine the truncation number

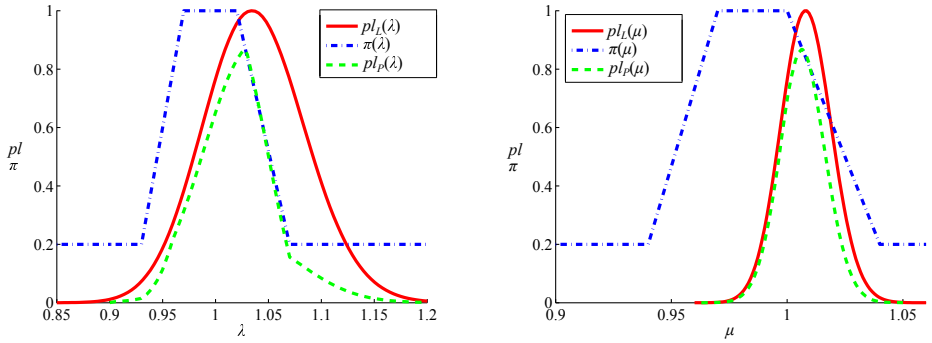

(a) Marginalisation on λ (b) Marginalisation on μ

Fig. 6.19 Marginal pl_L, π and pl_P in scenario 1

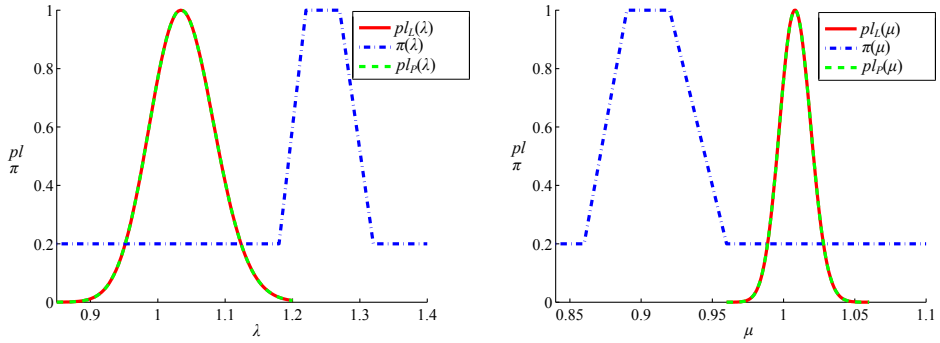

(a) Marginalisation on λ (b) Marginalisation on μ

Fig. 6.20 Marginal pl_L, π and pl_P in scenario 2

n in Eq. (6.18) and the threshold δ for the $\mathbf{1}_\delta$ in Eq. (6.19). In order to determine δ and n, we induce the approximation error of the POD:

$$\epsilon^{POD} = \frac{\mathcal{V}(\boldsymbol{v} - \boldsymbol{v}^{POD})}{\mathcal{V}(\boldsymbol{v})}, \tag{6.26}$$

where $\mathcal{V}(\boldsymbol{v} - \boldsymbol{v}^{POD})$ is the volume estimated using the point cloud of the difference between the original $\boldsymbol{v}$ and the approximated $\boldsymbol{v}^{POD}$, and $\mathcal{V}(\boldsymbol{v})$ is the volume of the domains associated with $\boldsymbol{v}$. Then the POD is performed on the samples of the posterior random set in scenario 1, and Fig. 6.21 shows the energy proportion of the first ten basis vectors. We can see that the first ten basis vectors corresponds to the majority of energy proportion. We can thus make use of the first several basis vectors to parametrize the target subsets.

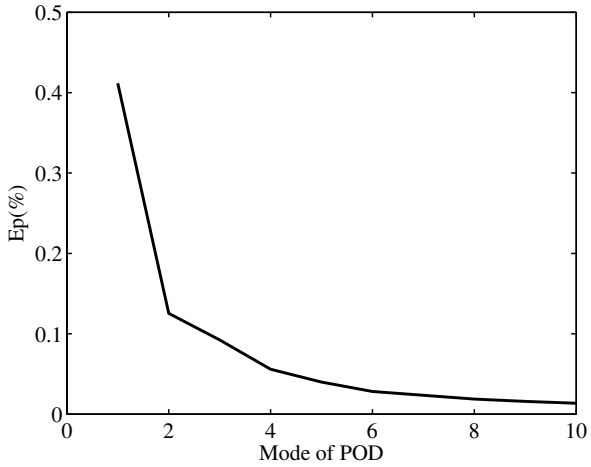

Fig. 6.21 Energy proportion Ep

Then, we preliminarily fix $\delta = 0.5$, and reconstruct 100 subsets using Eq. (6.18) with different truncation numbers. The approximation errors are shown in Fig. 6.22. In Fig. 6.21 and 6.22, we can see that the first 6 basis vectors represent more than 75% energy, and the approximation error does not decrease significantly when $n \geq 6$. Therefore, we choose $n = 6$. Next, we plot the approximation errors with different thresholds δ, in Fig. 6.23. We can see that when $\delta = 0.5$, the approximation error is minimum. Unless otherwise mentioned, the value of δ is fixed to 0.5 in this chapter.

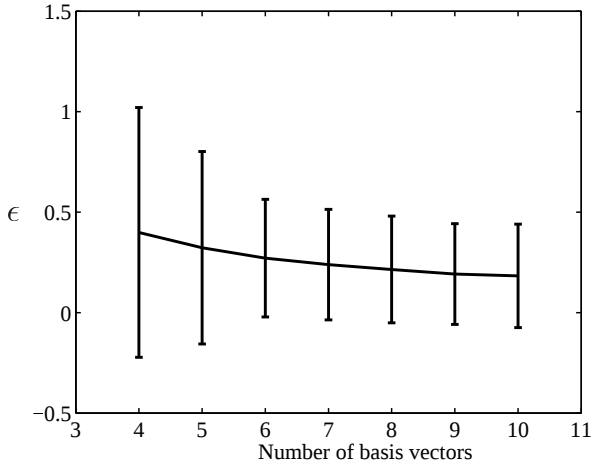

Fig. 6.22 Approximation error VS truncation number

When choosing the truncation number $n = 6$, there are six variables α_k, $k = 1, \cdots, 6$ in Eq. (6.20) to parametrize the target subsets. Then, we sample a number of α_k, regenerate the corresponding subsets, and calculate their Bel, Pl and $\mathcal{V}$ values. These

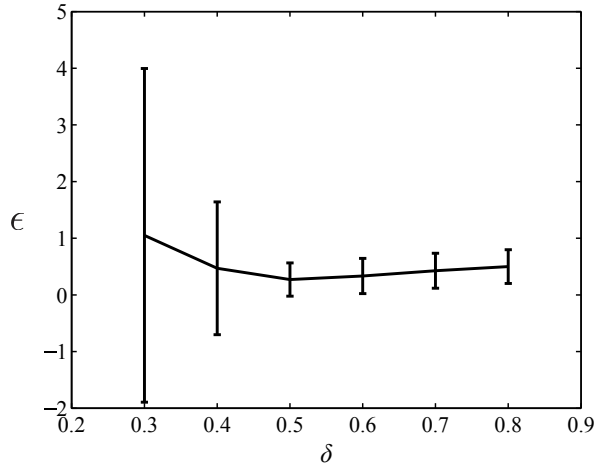

Fig. 6.23 Approximation error VS threshold δ

quantities corresponding to the two scenarios are shown in Fig. 6.24. The frontier of the cloud of points in Fig. 6.24 can be seen as an approximation of the Pareto frontier [Wilson et al., 2001]. The Pareto frontier [Wilson et al., 2001] is helpful to solve multi-objective optimization by yielding the potentially optimal solutions. This frontier reflects the relationship among the extreme values of Pl, Bel and $\mathcal{V}$. The points in Fig. 6.24(b) are all in the same plane ($Pl = 1$), because the posterior random set in scenario 2 is consonant. To enhance the precision of the Pareto frontier, [Deb et al., 2002] [Zitzler et al., 1998] [Knowles and Corne, 1999] offered some efficient tools for various applications. Here, we can make use of the Pareto frontier to get suitable initial values for finding the global minimum in Eq. (6.20). For example, we set (1) $\delta_{Bel} = 0.10$ and $\delta_{Pl} = 0.95$; (2) $\delta_{Bel} = 0.30$ and $\delta_{Pl} = 0.95$ (3) $\delta_{Bel} = 0.50$ and $\delta_{Pl} = 0.95$; the result subsets for the two scenarios are shown in Fig. 6.25. It is clear that the sizes of the minimum subsets increase as the threshold increases. The subsets in scenario 1 move toward the bottom left because of the influence of prior information compared with those in scenario 2. In scenario 2, the prior information does not affect the theoretical and measurement information, and the result subsets reflect the form of the likelihood function. For the third group of thresholds, the result subset covers the reference values in scenario 1. In this example, because the samples of posterior random set are mostly consonant, the δ_{Bel} is more important that δ_{Pl}. The reason is that the Pl reaches easily 1 for consonant random sets.

In order to illustrate the effect of prior information, we define the following estimator:

$$\widehat{\boldsymbol{\theta}}_L = \arg\max_{\boldsymbol{\theta}\in\boldsymbol{\Theta}} pl_L(\boldsymbol{\theta}). \tag{6.27}$$

The estimator $\widehat{\boldsymbol{\theta}}_L$ does not take into account the prior information. The estimator $\widehat{\boldsymbol{\theta}}_P$ defined in Eq (6.12), $\widehat{\boldsymbol{\theta}}_L$, and the reference values are shown in Fig. 6.25. It is clear that $\widehat{\boldsymbol{\theta}}_P$ moves toward the reference values in scenario 1 due to the regularization of prior information.

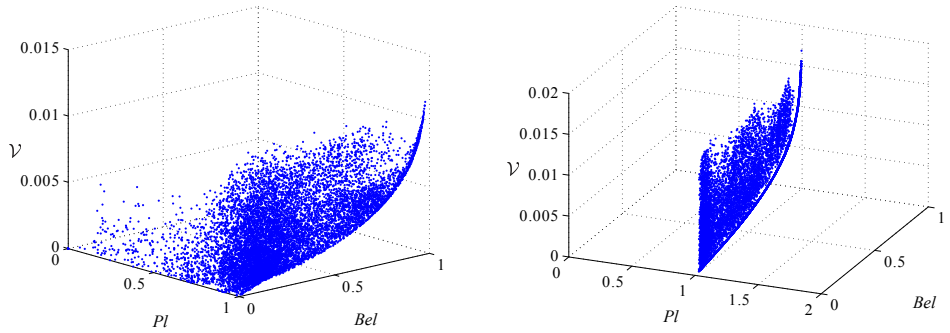

(a) Scenario 1 (b) Scenario 2

Fig. 6.24 Samples of Bel, Pl and $\mathcal{V}$

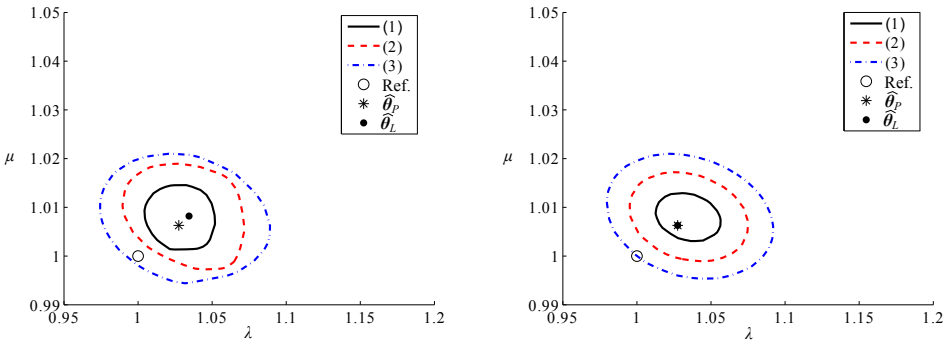

(a) Scenario 1 (b) Scenario 2

Fig. 6.25 Result subsets and estimators
(1) $\delta_{Bel} = 0.10$ and $\delta_{Pl} = 0.95$; (2) $\delta_{Bel} = 0.30$ and $\delta_{Pl} = 0.95$;
(3) $\delta_{Bel} = 0.50$ and $\delta_{Pl} = 0.95$

6.4.2 Identifying heterogeneous material

6.4.2.1 Measurement and prior information

In this application, we want to identify the elastic properties of a heterogeneous plate with an inclusion at its center as shown in Fig. 6.26. The matrix material is denoted

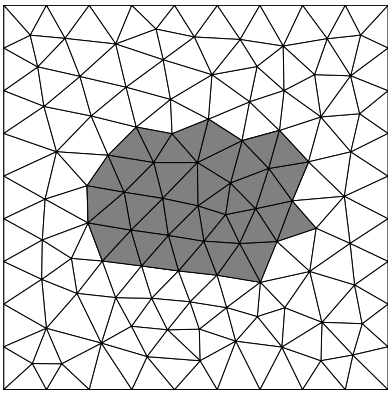

Fig. 6.26 Heterogeneous material

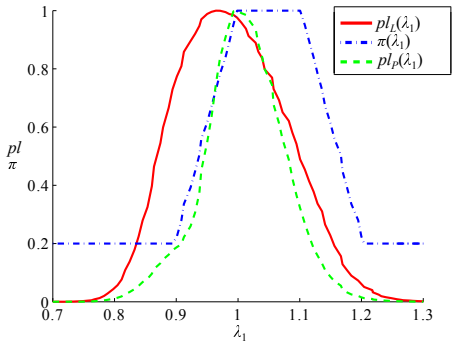

(a) Marginalisation on λ_1

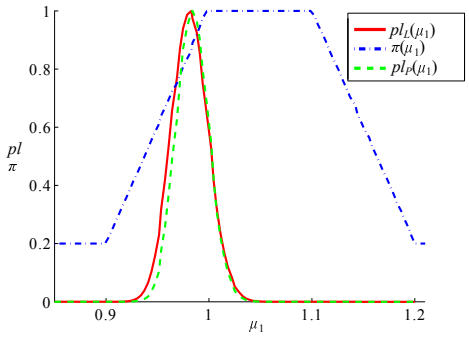

(b) Marginalisation on μ_1

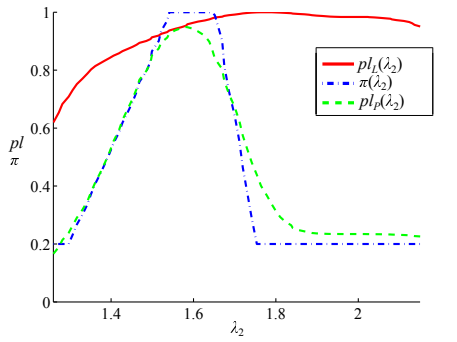

(c) Marginalisation on λ_2

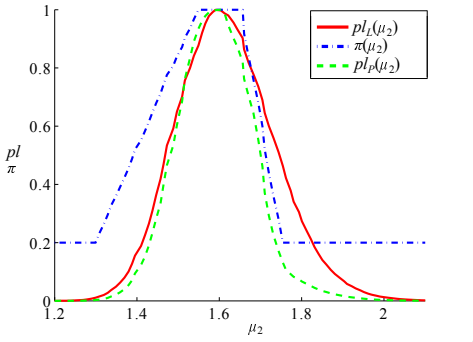

(d) Marginalisation on μ_2

Fig. 6.27 Marginal pl_L, π and pl_P

as material 1 (white area), and the inclusion material is denoted as material 2 (grey area). The plate is loaded on the right by a traction $\boldsymbol{f}$ whose horizontal projection is $\boldsymbol{f}_x = f_0 y(1-y)$ and vertical projection is null. The Lamé parameters $\boldsymbol{\theta} = \{\lambda_1, \mu_1, \lambda_2, \mu_2\}$ determine its elastic properties. The parameters λ_1 and μ_1 correspond to the matrix material; the parameters λ_2 and μ_2 correspond to the inclusion material. The relative

reference values are $\{\lambda_1^{ref}, \mu_1^{ref}, \lambda_2^{ref}, \mu_2^{ref}\} = \{1, 1, 1.5, 1.5\}$. The measurement error is a Gaussian white noise whose standard deviation is 5% with respect to the maximum displacement value.

The prior information comes from the expert opinions and is represented by the possibility distributions π shown in Fig. 6.27. Then a 80% degree of confidence is added to it. Using likelihood-based belief functions, the joint contour function pl_L on the theoretical and measurement information is constructed. In order to display pl_L clearly, Fig. 6.27 presents its marginal functions. The level of convergence of pl_L and π are similar in Fig. 6.27(a) and Fig. 6.27(d), indicating that the precision of measurement and prior information are similar. On the other hand, the levels of convergence of pl_L and π are clearly different in Fig. 6.27(b) and 6.27(c). The measurement information in Fig. 6.27(b) is more precise for parameter μ_1. The prior information in Fig. 6.27(c) provides more precise information on parameter λ_2.

6.4.2.2 Information merging

We use Dempster's rule to combine information. The marginal posterior contour functions pl_P are shown in Fig. 6.27. The pl_P are always more convergent than pl_L and π. Therefore, when measurement information is more precise, the prior information's influence is small. When measurement information does not allow precise inference, the prior information will induce regularization to measurement information.

6.4.2.3 Exploitation of the posterior random sets

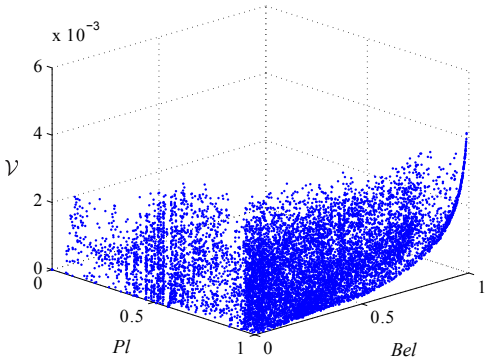

Fig. 6.28 Samples of Bel, Pl and $\mathcal{V}$

After constructing the POD from the samples of the posterior random set, as presented in Section 6.4.1.4, we choose the first six parameters to parametrize the target

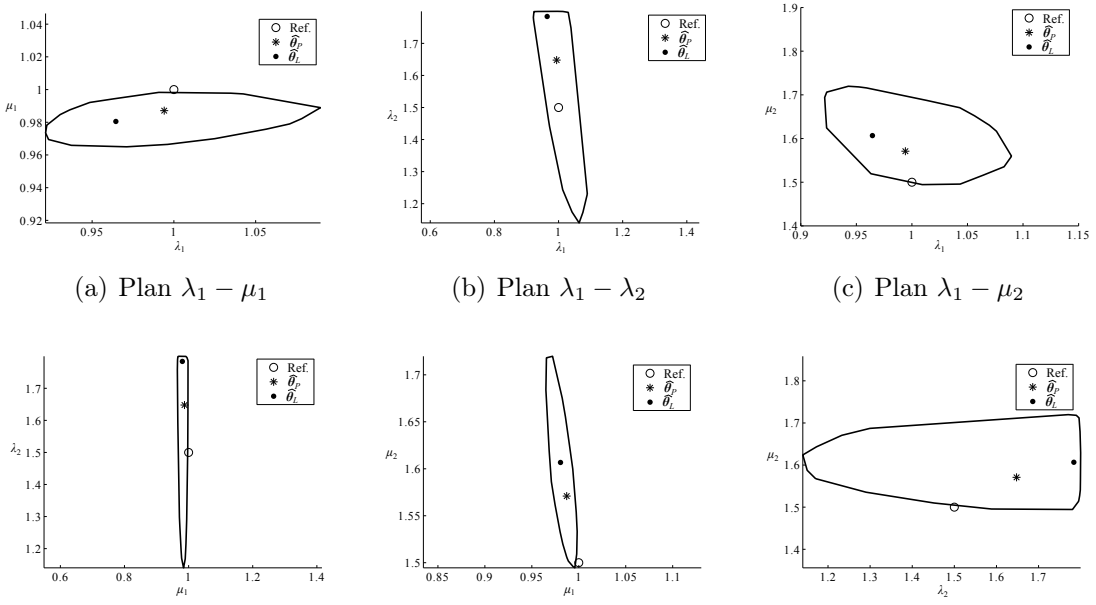

(a) Plan $\lambda_1 - \mu_1$ (b) Plan $\lambda_1 - \lambda_2$ (c) Plan $\lambda_1 - \mu_2$

(d) Plan $\mu_1 - \lambda_2$ (e) Plan $\mu_1 - \mu_2$ (f) Plan $\lambda_2 - \mu_2$

Fig. 6.29 Result subsets and estimators

subsets and fix δ to 0.5. Then, we sample a number of α_k, regenerate corresponding subsets, and calculate their Bel, Pl and $\mathcal{V}$ values. These quantities are shown in Fig. 6.28. Then we set $\delta_{Bel} = 0.30$ and $\delta_{Pl} = 0.95$; the minimum domains are shown in Fig. 6.29. The location of the maximum of pl_P is closer to the reference values than that of pl_L. The reason for this improvement is the regularization by the prior information. The shapes of the result subsets reflect the dependence between the parameters and while their sizes reflect the precision of input information. More precise information results in smaller subsets for the same threshold values. It should be noticed that the shapes of the result subsets are no more regular, which indicates that the use of regular shape functions as a parametrization of target subsets would not work here.

6.4.3 Identifying micro-scale properties by macro-scale tests

In this application, we continue to focus on the case introduced in Section 5.3.2 corresponding to the identification of micro-scale properties from a macro-scale test. The multi-structure material, loading case, displacement measurement remain the same as those in Section 5.3.2. We assume that all three statistical factors are reliable and known. The parameters to be identified are the two micro Young module $\boldsymbol{\theta} = \{E_1, E_2\}$ and the reference values are $\{1, 2\}$. Following the approach presented in Chapter

5, we take both measurement and model uncertainties into consideration. Both uncertainties are quantified by likelihood-based belief functions. Because of the shape of the contour function pl_L (pl_L was denoted as pl_A in Chapter 5), we cannot obtain precise identification results. The estimators via maximising the pl_L are sensitive to uncertainty. Therefore, we need to take advantage of the prior information.

The prior information, which comes from expert opinions, is expressed by possibility distributions as shown in Fig. 6.30. We also assume that we have 80% degree of confidence in the expert opinions. The joint contour function pl_L and the prior joint possibility distribution π are shown in Fig. 6.31. Then, we combine pl_L and π using Dempster's rule and obtain samples from the posterior random set. The posterior contour function pl_P is shown in Fig. 6.32. We can see that pl_P is more convergent than pl_L. We can also see this improvement from the marginal posterior contour functions in Fig. 6.33. It is clear that the prior information has concentrated the information due to regularization.

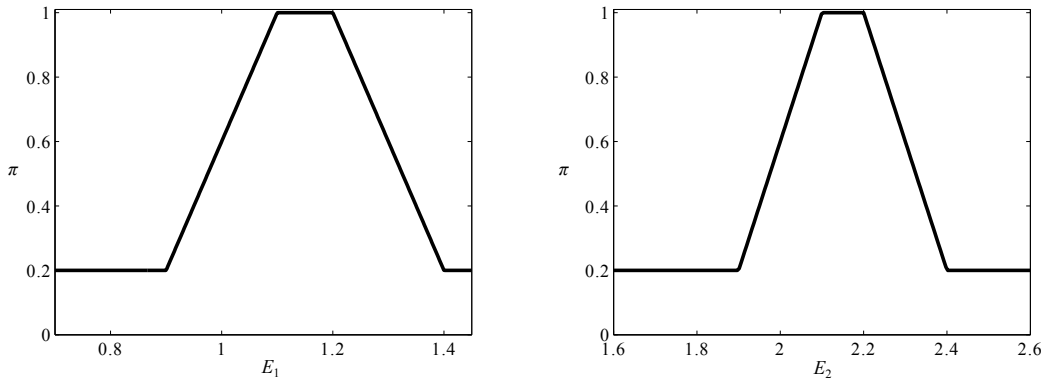

(a) Function on E_1 (b) Function on E_2

Fig. 6.30 Prior information

Then we perform a POD analysis on the samples of the posterior random set. Following the presentation in Section 6.4.1.4, we choose the first six parameters to parametrize the target subsets. Then, we sample a number of α_k, regenerate corresponding subsets, and calculate their Bel, Pl and $\mathcal{V}$ values. These quantities are shown in Fig. 6.34. The points are almost situated in the plane $Pl = 1$. The reason for this phenomenon is that most of the samples of the posterior random set are almost consonant. Then, we study three values of thresholds: (1) $\delta_{Bel} = 0.10$, $\delta_{Pl} = 0.95$; (2) $\delta_{Bel} = 0.25$, $\delta_{Pl} = 0.95$; (3) $\delta_{Bel} = 0.30$, $\delta_{Pl} = 0.95$. The result subsets for different thresholds are shown in Fig. 6.35. For the three result subsets, the Pl values are,

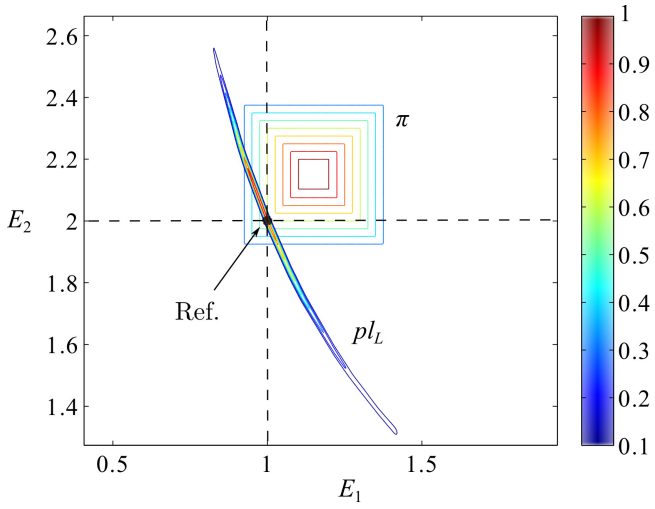

Fig. 6.31 π and pl_P

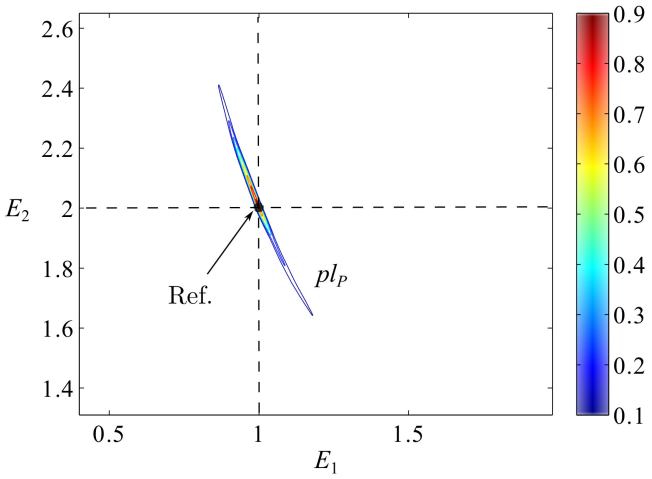

Fig. 6.32 Posterior contour function

respectively, 0.995, 0.987 and 0.977. Because the samples of posterior random set are almost consonant, the threshold δ_{Bel} is more important than δ_{Pl}.

6.5 Conclusion

In this chapter, we presented an identification strategy based on belief functions, making it possible to use prior information and quantify its uncertainty. Point clouds were used to describe multi-dimensional random sets. Dempster's rule was applied to combine prior information with theoretical and measurement information, and the

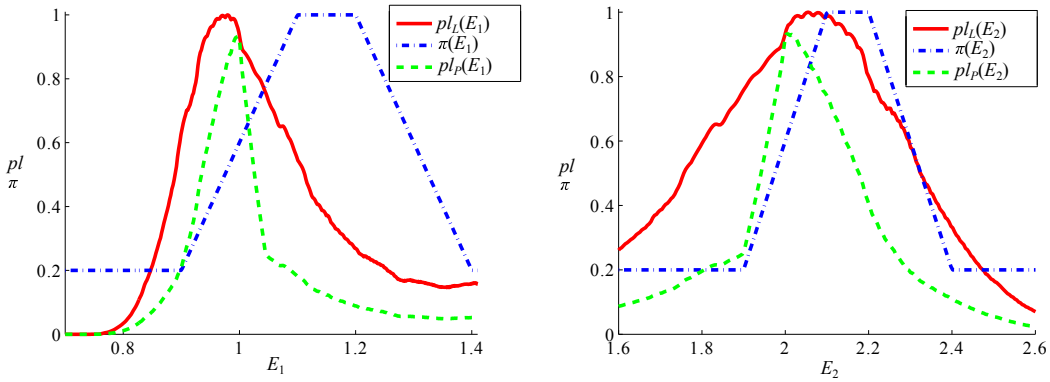

(a) Marginalisation on E_1 (b) Marginalisation on E_2

Fig. 6.33 Marginal pl_L, π and pl_P

posterior random set was sampled and exploited. This approach allows us to encode and propagate epistemic and aleatory uncertainty in a single framework. In this framework, a degree of confidence makes it possible to express subjective confidence in information sources. Due to the degree of confidence, when the prior information is wrong, it does not affect the theoretical and measurement information. This is an advantage of our approach as compared to Bayesian inference. Dempster's rule needs more computation time to combine information than the product rule, but, the posterior random set from Dempster's rule is more informative. The exploitation enables us to know the compatibility between information sources. Moreover, the two quantities Bel and Pl are available to quantify their uncertainty. Considering the various sources of prior information, these quantities provide a new view to uncertainty analysis.

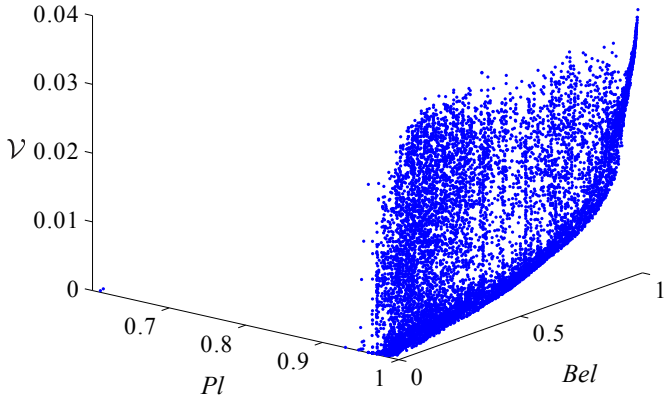

Fig. 6.34 Samples of Bel, Pl and $\mathcal{V}$

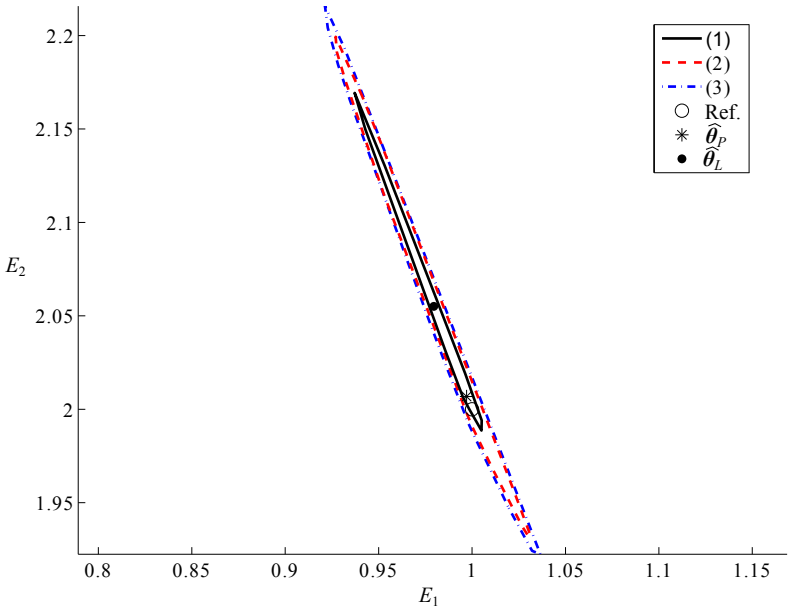

Fig. 6.35 Result subsets and estimators
(1) $\delta_{Bel} = 0.10$ and $\delta_{Pl} = 0.95$, (2) $\delta_{Bel} = 0.25$ and $\delta_{Pl} = 0.95$,
(3) $\delta_{Bel} = 0.30$ and $\delta_{Pl} = 0.95$

Chapter 7

Conclusion

In this thesis, an effective identification methodology has been developed, taking advantage of all available information including theoretical, experimental and empirical information. This methodology has proved effective for estimating material property parameters using full-field measurements from complex tests. During the identification processes, heterogeneous uncertainties arising from unreliable information have been studied for improving the performance of identification. The identification strategy proposed in this thesis makes it possible to manage the heterogeneous uncertainties with divergent natures and representation approaches in a unified framework based on the theory of belief functions. Meanwhile, a method with high computational efficiency has been developed to implement the strategy.

The uncertainty quantified in this thesis was classified into measurement uncertainty, model uncertainty and prior information uncertainty with respect to the information with which they were associated. Uncertainties were represented in different ways according to their different natures. Measurement uncertainty arising from limitations of measurement devices was considered as aleatory, and represented by probability distributions; model uncertainty originating from simplification and approximation of the real materials was considered as epistemic, and represented by intervals; prior information uncertainty caused by subjective imprecision was considered as epistemic as well and represented by random sets. In order to integrate all information and obtain more precise and reasonable results, the identification strategy consists of:

1. likelihood-based belief functions to summarise the experimental information and the theoretical information;

2. representation of the model uncertainty using interval fields to overcome the dependence and conservativeness problems of pure interval analysis;

3. proper orthogonal decomposition technique to construct basis vectors and interval factors for interval fields;
4. Dempster's rule to merge information and to account for prior information;
5. point clouds to describe multi-dimensional random sets;
6. deterministic and non-deterministic estimators to provide useful results for identification.

The following applications have been studied:

1. identification of the parameters of composite materials at macro-scale from the tests and measurement fields at micro-scale;
2. identification of the parameters of composite materials at micro-scale from the tests and measurement fields at macro-scale;
3. identification of the parameters of homogeneous and heterogeneous plates taking considering of prior information;
4. identification of the parameters of composite materials at micro-scale from the tests and measurement fields at macro-scale, accounting for prior information.

Applications 1 and 2 focused on modelling measurement and model uncertainties. Both applications demonstrated that the estimators via maximising contour functions in which the model uncertainty was considered were closer to the reference values than those via maximising standard likelihood functions. This proved robust even when the statistical factors of composite materials were unreliable. Meanwhile, the contour functions accounting for the model uncertainty were less convergent. As a result, they had greater coverage probability.

In applications 3 and 4, the prior information and its uncertainty were taken into consideration. During this process, a degree of confidence allowed us to express the subjective confidence in the sources of prior information. Due to the degree of confidence, when the prior information was wrong, it could not affect the theoretical and experimental information. This is an advantage of the inference based on the theory of belief functions as compared to Bayesian inference.

In summary, the development and implementation of the proposed identification strategy obviously improved the accuracy and robustness of parameter identification. The presented identification method could be continuously explored to deal with more

complex material models, such as non-linear ones. The computational complexity of algorithms should also be given more attention. For modelling model uncertainty, other methods for constructing interval fields should be investigated. Finally, the uncertainty arising from unreliable boundary conditions should be studied in the future.

References

Ackermann, F. (1984). Digital image correlation: performance and potential application in photogrammetry. *The Photogrammetric Record*, 11(64):429–439.

Akpan, U., Koko, T., Orisamolu, I., and Gallant, B. (2001). Practical fuzzy finite element analysis of structures. *Finite Elements in analysis and Design*, 38(2):93–111.

Allix, O., Feissel, P., and Thévenet, P. (2003). A delay damage mesomodel of laminates under dynamic loading: basic aspects and identification issues. *Computers & structures*, 81(12):1177–1191.

Andreassen, E. and Andreasen, C. S. (2014). How to determine composite material properties using numerical homogenization. *Computational Materials Science*, 83:488–495.

Andrews, L. C. (1997). *Special Functions of Mathematics for Engineers*. McGraw-Hill, Inc.

Anzengruber, S. W. (2011). *The discrepancy principle for Tikhonov regularization in Banach spaces*. PhD thesis, Johannes Kepler University in Linz.

Anzengruber, S. W., Hofmann, B., and Mathé, P. (2014). Regularization properties of the sequential discrepancy principle for tikhonov regularization in banach spaces. *Applicable Analysis*, 93(7):1382–1400.

Aprostolakis, G. (1990). The concept of probability in safety assessments of technological systems. *Science(Washington)*, 250(4986):1359–1364.

Archbold, E., Burch, J., and Ennos, A. (1970). Recording of in-plane surface displacement by double-exposure speckle photography. *Journal of Modern Optics*, 17(12):883–898.

Asundi, A., Cheung, M., and Lee, C. (1989). Moiré interferometry for simultaneous measurement of u, vw. *Experimental Mechanics*, 29(3):258–260.

Aven, T. (2011). Interpretations of alternative uncertainty representations in a reliability and risk analysis context. *Reliability Engineering & System Safety*, 96(3):353–360.

Avril, S., Bonnet, M., Bretelle, A.-S., Grediac, M., Hild, F., Ienny, P., Latourte, F., Lemosse, D., Pagano, S., Pagnacco, E., et al. (2008a). Overview of identification methods of mechanical parameters based on full-field measurements. *Experimental Mechanics*, 48(4):381–402.

Avril, S. and Pierron, F. (2007). General framework for the identification of constitutive parameters from full-field measurements in linear elasticity. *International Journal of Solids and Structures*, 44(14–15):4978 – 5002.

Avril, S., Pierron, F., Pannier, Y., and Rotinat, R. (2008b). Stress reconstruction and constitutive parameter identification in plane-stress elasto-plastic problems using surface measurements of deformation fields. *Experimental Mechanics*, 48(4):403–419.

Azzouna, M. B., Feissel, P., and Villon, P. (2013). Identification of elastic properties from full-field measurements: a numerical study of the effect of filtering on the identification results. *Measurement Science and Technology*, 24(5):055603.

Azzouna, M. B., Feissel, P., and Villon, P. (2015). Robust identification of elastic properties using the modified constitutive relation error. *Computer Methods in Applied Mechanics and Engineering*, 295:196–218.

Barthe, D., Ladeveze, P., Deraemaeker, A., and Loch, S. L. (2004). Validation and updating of industrial models based on the constitutive relation error. *AIAA journal*, 42(7):1427–1434.

Baudrit, C. and Dubois, D. (2006). Practical representations of incomplete probabilistic knowledge. *Computational statistics & data analysis*, 51(1):86–108.

Bay, B. K., Smith, T. S., Fyhrie, D. P., and Saad, M. (1999). Digital volume correlation: three-dimensional strain mapping using x-ray tomography. *Experimental mechanics*, 39(3):217–226.

Bellenfant, G., Guyonnet, D., Dubois, D., and Bouc, O. (2009). Uncertainty theories applied to the analysis of CO2 plume extension during geological storage. *Energy Procedia*, 1(1):2447–2454.

Ben Abdallah, N., Mouhous-Voyneau, N., and Denœux, T. (2014). Combining statistical and expert evidence using belief functions: Application to centennial sea level estimation taking into account climate change. *International Journal of Approximate Reasoning*, 55(1):341–354.

Berkooz, G., Holmes, P., and Lumley, J. L. (1993). The proper orthogonal decomposition in the analysis of turbulent flows. *Annual review of fluid mechanics*, 25(1):539–575.

Bilger, N., Auslender, F., Bornert, M., Michel, J.-C., Moulinec, H., Suquet, P., and Zaoui, A. (2005). Effect of a nonuniform distribution of voids on the plastic response of voided materials: a computational and statistical analysis. *International Journal of Solids and Structures*, 42(2):517–538.

Bonesky, T. (2008). Morozov's discrepancy principle and tikhonov-type functionals. *Inverse Problems*, 25(1):015015.

Bonnet, M. (2012). Introduction to identification methods. In Grédiac, M. and Hild, F., editors, *Full-field measurements and identification in solid mechanics*. John Wiley & Sons.

Bornert, M., Brémand, F., Doumalin, P., Dupré, J.-C., Fazzini, M., Grédiac, M., Hild, F., Mistou, S., Molimard, J., Orteu, J.-J., et al. (2009). Assessment of digital image correlation measurement errors: methodology and results. *Experimental mechanics*, 49(3):353–370.

Bouclier, R., Louf, F., and Chamoin, L. (2013). Real-time validation of mechanical models coupling pgd and constitutive relation error. *Computational Mechanics*, 52(4):861–883.

Bruck, H., McNeill, S., Sutton, M. A., and Peters Iii, W. (1989). Digital image correlation using newton-raphson method of partial differential correction. *Experimental mechanics*, 29(3):261–267.

Caflisch, R. E. (1998). Monte Carlo and quasi-Monte Carlo methods. *Acta numerica*, 7:1–49.

Calloch, S., Dureisseix, D., and Hild, F. (2002). Identification de modèles de comportement de matériaux solides: utilisation d'essais et de calculs. *Technologies et Formations*, 100:36–41.

Calvetti, D., Morigi, S., Reichel, L., and Sgallari, F. (2000). Tikhonov regularization and the l-curve for large discrete ill-posed problems. *Journal of computational and applied mathematics*, 123(1):423–446.

Chalal, H., Avril, S., Pierron, F., and Meraghni, F. (2006). Experimental identification of a nonlinear model for composites using the grid technique coupled to the virtual fields method. *Composites Part A: Applied Science and Manufacturing*, 37(2):315–325.

Chazot, J.-D., Zhang, E., and Antoni, J. (2012). Acoustical and mechanical characterization of poroelastic materials using a bayesian approach. *The Journal of the Acoustical Society of America*, 131(6):4584–4595.

Chen, D., Chiang, F.-P., Tan, Y., and Don, H. (1993). Digital speckle-displacement measurement using a complex spectrum method. *Applied optics*, 32(11):1839–1849.

Chen, L. and Rao, S. (1997). Fuzzy finite-element approach for the vibration analysis of imprecisely-defined systems. *Finite Elements in Analysis and Design*, 27(1):69–83.

Chen, S., Lian, H., and Yang, X. (2002). Interval static displacement analysis for structures with interval parameters. *International Journal for Numerical Methods in Engineering*, 53(2):393–407.

Chen, S.-H. and Yang, X.-W. (2000). Interval finite element method for beam structures. *Finite elements in analysis and design*, 34(1):75–88.

Cho, S., Chasiotis, I., Friedmann, T. A., and Sullivan, J. P. (2005). Young's modulus, poisson's ratio and failure properties of tetrahedral amorphous diamond-like carbon for mems devices. *Journal of Micromechanics and Microengineering*, 15(4):728.

Claire, D., Hild, F., and Roux, S. (2002). Identification of damage fields using kinematic measurements. *Comptes Rendus Mecanique*, 330(11):729–734.

Claire, D., Hild, F., and Roux, S. (2004). A finite element formulation to identify damage fields: the equilibrium gap method. *International Journal for Numerical Methods in Engineering*, 61(2):189–208.

Collins, J. D., Hart, G. C., Haselman, T., and Kennedy, B. (1974). Statistical identification of structures. *AIAA journal*, 12(2):185–190.

Constantinescu, A. (1995). On the identification of elastic moduli from displacement-force boundary measurements. *Inverse Problems in Engineering*, 1(4):293–313.

Couso, I. and Sánchez, L. (2011). Upper and lower probabilities induced by a fuzzy random variable. *Fuzzy Sets and Systems*, 165(1):1–23.

Crouzeix, L., Périé, J. N., Collombet, F., and Douchin, B. (2009). An orthotropic variant of the equilibrium gap method applied to the analysis of a biaxial test on a composite material. *Composites Part A: Applied Science and Manufacturing*, 40(11):1732 – 1740.

Deb, K., Anand, A., and Joshi, D. (2002). A computationally efficient evolutionary algorithm for real-parameter optimization. *Evolutionary computation*, 10(4):371–395.

Denœux, T. (2014). Likelihood-based belief function: Justification and some extensions to low-quality data. *International Journal of Approximate Reasoning*, 55(7):1535 – 1547.

Der Kiureghian, A. and Ke, J.-B. (1988). The stochastic finite element method in structural reliability. *Probabilistic Engineering Mechanics*, 3(2):83–91.

Deraemaeker, A., Ladevèze, P., and Leconte, P. (2002). Reduced bases for model updating in structural dynamics based on constitutive relation error. *Computer Methods in Applied Mechanics and Engineering*, 191(21–22):2427 – 2444.

Dubois, D., Kerre, E., Mesiar, R., and Prade, H. (2000). Fuzzy interval analysis. In *Fundamentals of fuzzy sets*, pages 483–581. Springer.

Dubois, D. and Prade, H. (1986). A set-theoretic view of belief functions: logical operations and approximations by fuzzy sets. *International Journal of General Systems*, 12(3):193–226.

Fang, S.-E., Perera, R., and Roeck, G. D. (2008). Damage identification of a reinforced concrete frame by finite element model updating using damage parameterization. *Journal of Sound and Vibration*, 313(3–5):544 – 559.

Farhat, C. and Hemez, F. M. (1993). Updating finite element dynamic models using an element-by-element sensitivity methodology. *AIAA journal*, 31(9):1702–1711.

Faverjon, B. and Sinou, J.-J. (2008). Robust damage assessment of multiple cracks based on the frequency response function and the constitutive relation error updating method. *Journal of Sound and Vibration*, 312(4–5):821 – 837.

Feissel, P. and Allix, O. (2007). Modified constitutive relation error identification strategy for transient dynamics with corrupted data: The elastic case. *Computer Methods in Applied Mechanics and Engineering*, 196(13):1968–1983.

Feissel, P., Schneider, J., Aboura, Z., and Villon, P. (2013). Use of diffuse approximation on DIC for early damage detection in 3d carbon/epoxy composites. *Composites Science and Technology*, 88:16–25.

Ferson, S. and Ginzburg, L. R. (1996). Different methods are needed to propagate ignorance and variability. *Reliability Engineering & System Safety*, 54(2):133–144.

Ferson, S., Kreinovich, V., Ginzburg, L., Myers, D. S., and Sentz, K. (2003). Constructing probability boxes and dempster-shafer structures. *Sandia National Laboratories*, pages 143–180.

Feyel, F. and Chaboche, J.-L. (2000). Fe 2 multiscale approach for modelling the elastoviscoplastic behaviour of long fibre sic/ti composite materials. *Computer methods in applied mechanics and engineering*, 183(3):309–330.

Florentin, E. and Lubineau, G. (2010). Identification of the parameters of an elastic material model using the constitutive equation gap method. *Computational Mechanics*, 46(4):521–531.

Fritzen, F. (2011). *Microstructural modeling and computational homogenization of the physically linear and nonlinear constitutive behavior of micro-heterogeneous materials*, volume 1. KIT Scientific Publishing.

Fullér, R. and Majlender, P. (2004). On interactive fuzzy numbers. *Fuzzy Sets and Systems*, 143(3):355–369.

Gao, W., Wu, D., Song, C., Tin-Loi, F., and Li, X. (2011). Hybrid probabilistic interval analysis of bar structures with uncertainty using a mixed perturbation monte-carlo method. *Finite Elements in Analysis and Design*, 47(7):643–652.

Gao, Z., Xu, X., Su, Y., and Zhang, Q. (2016). Experimental analysis of image noise and interpolation bias in digital image correlation. *Optics and Lasers in Engineering*, 81:46–53.

Ghanem, R. G. and Spanos, P. D. (1991). *Stochastic finite elements: a spectral approach*. Springer.

Giannini, O. and Hanss, M. (2008). An interdependency index for the outputs of uncertain systems. *Fuzzy sets and systems*, 159(11):1292–1308.

Giraudeau, A. and Pierron, F. (2003). Simultaneous identification of stiffness and damping properties of isotropic materials from forced vibrating plates. *Comptes Rendus Mécanique*, 331(4):259–264.

Giton, M. (2006). Hyperelastic behaviour identification by forward problem resolution: Application to a tear test of a silicone-rubber. *Strain*, 42(4):291–298.

Gogu, C., Haftka, R., Riche, R. L., Molimard, J., and Vautrin, A. (2010). Introduction to the bayesian approach applied to elastic constants identification. *AIAA journal*, 48(5):893–903.

Gogu, C., Yin, W., Haftka, R., Ifju, P., Molimard, J., Le Riche, R., and Vautrin, A. (2013). Bayesian identification of elastic constants in multi-directional laminate from moiré interferometry displacement fields. *Experimental Mechanics*, 53(4):635–648.

Graham, L. and Deodatis, G. (2001). Response and eigenvalue analysis of stochastic finite element systems with multiple correlated material and geometric properties. *Probabilistic Engineering Mechanics*, 16(1):11–29.

Grédiac, M. (1989). Principe des travaux virtuels et identification. *Comptes rendus de l'Académie des sciences. Série 2, Mécanique, Physique, Chimie, Sciences de l'univers, Sciences de la Terre*, 309(1):1–5.

Grédiac, M. and Pierron, F. (1998). At-shaped specimen for the direct characterization of orthotropic materials. *International Journal for Numerical Methods in Engineering*, 41(2):293–309.

Grédiac, M., Toussaint, E., and Pierron, F. (2002). Special virtual fields for the direct determination of material parameters with the virtual fields method. 2—-application to in-plane properties. *International Journal of Solids and Structures*, 39(10):2707–2730.

Grédiac, M. (2004). The use of full-field measurement methods in composite material characterization: interest and limitations. *Composites Part A: Applied Science and Manufacturing*, 35(7–8):751 – 761.

Guery, A., Hild, F., Latourte, F., and Roux, S. (2016). Identification of crystal plasticity parameters using DIC measurements and weighted FEMU. *Mechanics of Materials*, 100:55 – 71.

Haag, T. and Hanss, M. (2012). Comprehensive modeling of uncertain systems using fuzzy set theory. In *Nondeterministic Mechanics*, pages 193–226. Springer.

Hadamard, J. (1902). Sur les problèmes aux dérivées partielles et leur signification physique. *Princeton university bulletin*, 13(49-52):28.

Halton, J. H. (1960). On the efficiency of certain quasi-random sequences of points in evaluating multi-dimensional integrals. *Numerische Mathematik*, 2(1):84–90.

Hanss, M. (1999). On the implementation of fuzzy arithmetical operations for engineering problems. In *Fuzzy Information Processing Society, 1999. NAFIPS. 18th International Conference of the North American*, pages 462–466. IEEE.

Hanss, M. (2002). The transformation method for the simulation and analysis of systems with uncertain parameters. *Fuzzy Sets and Systems*, 130(3):277–289.

Hanss, M. (2003a). An approach to inverse fuzzy arithmetic. In *Fuzzy Information Processing Society, 2003. NAFIPS 2003. 22nd International Conference of the North American*, pages 474–479. IEEE.

Hanss, M. (2003b). The extended transformation method for the simulation and analysis of fuzzy-parameterized models. *International Journal of Uncertainty, Fuzziness and Knowledge-Based Systems*, 11(06):711–727.

Hashin, Z. (1983). Analysis of composite materials—a survey. *Journal of Applied Mechanics*, 50(3):481–505.

Hassan, G. M., MacNish, C., Dyskin, A., and Shufrin, I. (2016). Digital image correlation with dynamic subset selection. *Optics and Lasers in Engineering*, 84:1–9.

He, T., Liu, L., Makeev, A., and Shonkwiler, B. (2016). Characterization of stress–strain behavior of composites using digital image correlation and finite element analysis. *Composite Structures*, 140:84 – 93.

Helm, J., Sutton, M., and Boone, M. (2001). Characterizing crack growth in thin aluminum panels under tension-torsion loading using three-dimensional digital image correlation. In *Nontraditional Methods of Sensing Stress, Strain, and Damage in Materials and Structures*. ASTM International.

Helton, J. C. and Oberkampf, W. (2004). Alternative representations of epistemic uncertainty. *Reliability Engineering & System Safety*, 85(1):1–10.

Hill, R. (1963). Elastic properties of reinforced solids: some theoretical principles. *Journal of the Mechanics and Physics of Solids*, 11(5):357–372.

Hoc, T., Crépin, J., Gélébart, L., and Zaoui, A. (2003). A procedure for identifying the plastic behavior of single crystals from the local response of polycrystals. *Acta Materialia*, 51(18):5477–5488.

Hollister, S. J. and Kikuchi, N. (1992). A comparison of homogenization and standard mechanics analyses for periodic porous composites. *Computational Mechanics*, 10(2):73–95.

Holmes, C. and Adams, N. (2002). A probabilistic nearest neighbour method for statistical pattern recognition. *Journal of the Royal Statistical Society: Series B (Statistical Methodology)*, 64(2):295–306.

Huang, S., Feissel, P., and Villon, P. (2016). Modified constitutive relation error: An identification framework dealing with the reliability of information. *Computer Methods in Applied Mechanics and Engineering*, 311:1 – 17.

Jin, H., Lu, W., and Korellis, J. (2008). Micro-scale deformation measurement using the digital image correlation technique and scanning electron microscope imaging. *The Journal of Strain Analysis for Engineering Design*, 43(8):719–728.

Jolliffe, I. (2002). *Principal component analysis*. Wiley Online Library.

Jones, R. and Wykes, C. (1989). *Holographic and speckle interferometry*, volume 6. Cambridge university press.

Kajberg, J. and Lindkvist, G. (2004). Characterisation of materials subjected to large strains by inverse modelling based on in-plane displacement fields. *International Journal of Solids and Structures*, 41(13):3439 – 3459.

Kanouté, P., Boso, D., Chaboche, J., and Schrefler, B. (2009). Multiscale methods for composites: a review. *Archives of Computational Methods in Engineering*, 16(1):31–75.

Kavanagh, K. T. and Clough, R. W. (1971). Finite element applications in the characterization of elastic solids. *International Journal of Solids and Structures*, 7(1):11–23.

Kerschen, G., Golinval, J.-c., Vakakis, A. F., and Bergman, L. A. (2005). The method of proper orthogonal decomposition for dynamical characterization and order reduction of mechanical systems: an overview. *Nonlinear dynamics*, 41(1-3):147–169.

Kirugulige, M. S., Tippur, H. V., and Denney, T. S. (2007). Measurement of transient deformations using digital image correlation method and high-speed photography: application to dynamic fracture. *Applied optics*, 46(22):5083–5096.

Klir, G. J. (1989). Is there more to uncertainty than some probability theorists might have us believe? *International Journal of General System*, 15(4):347–378.

Knowles, J. and Corne, D. (1999). The Pareto archived evolution strategy: A new baseline algorithm for Pareto multiobjective optimisation. In *Evolutionary Computation, 1999. CEC 99. Proceedings of the 1999 Congress on*, volume 1. IEEE.

Kumar, S. and Kurtz, S. K. (1995). Monte-carlo study of angular and edge length distributions in a three-dimensional poisson-voronoi tesselation. *Materials characterization*, 34(1):15–27.

Ladeveze, P. (1993). Error on the constitutive relation in dynamics: theory and application to model updating in structural dynamics. Technical report, Internal Report 150, LMT-Cachan, in French.

Ladeveze, P. and Leguillon, D. (1983). Error estimate procedure in the finite element method and applications. *SIAM Journal on Numerical Analysis*, 20(3):485–509.

Ladevèze, P., Moës, N., and Douchin, B. (1999). Constitutive relation error estimators for (visco) plastic finite element analysis with softening. *Computer Methods in Applied Mechanics and Engineering*, 176(1):247–264.

Ladeveze, P., Puel, G., Deraemaeker, A., and Romeuf, T. (2006a). Validation of structural dynamics models containing uncertainties. *Computer methods in applied mechanics and engineering*, 195(4):373–393.

Ladeveze, P., Puel, G., and Romeuf, T. (2006b). Lack of knowledge in structural model validation. *Computer methods in applied mechanics and engineering*, 195(37):4697–4710.

Ladevèze, P. and Nouy, A. (2003). On a multiscale computational strategy with time and space homogenization for structural mechanics. *Computer Methods in Applied Mechanics and Engineering*, 192(28–30):3061 – 3087. Multiscale Computational Mechanics for Materials and Structures.

Ladevèze, P., Rougeot, P., Blanchard, P., and Moreau, J. (1999). Local error estimators for finite element linear analysis. *Computer Methods in Applied Mechanics and Engineering*, 176(1):231 – 246.

Latourte, F., Chrysochoos, A., Pagano, S., and Wattrisse, B. (2008). Elastoplastic behavior identification for heterogeneous loadings and materials. *Experimental Mechanics*, 48(4):435–449.

Leclerc, H., Périé, J.-N., Roux, S., and Hild, F. (2009). Integrated digital image correlation for the identification of mechanical properties. In *International Conference on Computer Vision/Computer Graphics Collaboration Techniques and Applications*, pages 161–171. Springer.

Li, C.-C. and Der Kiureghian, A. (1993). Optimal discretization of random fields. *Journal of engineering mechanics*, 119(6):1136–1154.

Liang, Y., Lee, H., Lim, S., Lin, W., Lee, K., and Wu, C. (2002). Proper orthogonal decomposition and its applications—part i: Theory. *Journal of Sound and vibration*, 252(3):527–544.

Liu, W. K., Belytschko, T., and Mani, A. (1986). Probabilistic finite elements for nonlinear structural dynamics. *Computer Methods in Applied Mechanics and Engineering*, 56(1):61–81.

Loeve, M. (1978). Probability theory, vol. ii. *Graduate texts in mathematics*, 46:0–387.

Louf, F., Enjalbert, P., Ladevèze, P., and Romeuf, T. (2010). On lack-of-knowledge theory in structural mechanics. *Comptes Rendus Mécanique*, 338(7):424–433.

Luu, L., Wang, Z., Vo, M., Hoang, T., and Ma, J. (2011). Accuracy enhancement of digital image correlation with b-spline interpolation. *Optics letters*, 36(16):3070–3072.

McKay, M. D., Beckman, R. J., and Conover, W. J. (1979). Comparison of three methods for selecting values of input variables in the analysis of output from a computer code. *Technometrics*, 21(2):239–245.

McWilliam, S. (2001). Anti-optimisation of uncertain structures using interval analysis. *Computers & Structures*, 79(4):421–430.

Michel, B., François, H., Jean-José, O., and Stéphane, R. (2012). Digital image correlation. In Grédiac, M. and Hild, F., editors, *Full-field measurements and identification in solid mechanics*. John Wiley & Sons.

Michel, J., Moulinec, H., and Suquet, P. (1999). Effective properties of composite materials with periodic microstructure: a computational approach. *Computer methods in applied mechanics and engineering*, 172(1):109–143.

Mitra, N. J., Nguyen, A., and Guibas, L. (2004). Estimating surface normals in noisy point cloud data. *International Journal of Computational Geometry & Applications*, 14(04n05):261–276.

Moens, D., De Munck, M., Desmet, W., and Vandepitte, D. (2011). Numerical dynamic analysis of uncertain mechanical structures based on interval fields. In *IUTAM Symposium on the Vibration Analysis of Structures with Uncertainties*, pages 71–83. Springer.

Moens, D. and Hanss, M. (2011). Non-probabilistic finite element analysis for parametric uncertainty treatment in applied mechanics: Recent advances. *Finite Elements in Analysis and Design*, 47(1):4–16.

Muhanna, R. L. and Mullen, R. L. (2001). Uncertainty in mechanics problems-interval-based approach. *Journal of Engineering Mechanics*, 127(6):557–566.

Nasekhian, A. and Schweiger, H. F. (2011). Random set finite element method application to tunnelling. *International Journal of Reliability and Safety*, 5(3-4):299–319.

Newman, A. J. (1996). Model reduction via the karhunen-loeve expansion part i: An exposition.

Nguyen, H. T. (1978). On random sets and belief functions. *Journal of Mathematical Analysis and Applications*, 65(3):531–542.

Nguyen, H. T. (2006). *An introduction to random sets*. CRC press.

Nguyen, M.-T., Allain, J.-M., Gharbi, H., Desceliers, C., and Soize, C. (2016). Experimental multiscale measurements for the mechanical identification of a cortical bone by digital image correlation. *Journal of the Mechanical Behavior of Biomedical Materials*, 63:125–133.

Niederreiter, H. (2010). *Quasi-Monte Carlo Methods*. Wiley Online Library.

Oberkampf, W. L., Helton, J. C., Joslyn, C. A., Wojtkiewicz, S. F., and Ferson, S. (2004). Challenge problems: uncertainty in system response given uncertain parameters. *Reliability Engineering & System Safety*, 85(1):11–19.

Ohser, J. and Mücklich, F. (2000). *Statistical analysis of microstructures in materials science*. Wiley.

Pagnacco, E., Moreau, A., and Lemosse, D. (2007). Inverse strategies for the identification of elastic and viscoelastic material parameters using full-field measurements. *Materials Science and Engineering: A*, 452:737–745.

Pan, B. (2013). Bias error reduction of digital image correlation using gaussian pre-filtering. *Optics and Lasers in Engineering*, 51(10):1161 – 1167.

Papadrakakis, M. and Papadopoulos, V. (1996). Robust and efficient methods for stochastic finite element analysis using monte carlo simulation. *Computer Methods in Applied Mechanics and Engineering*, 134(3):325 – 340.

Parks, V. J. (1982). Strain measurement using grids. *Optical Engineering*, 21(4):214633–214633.

Parry, G. and Winter, P. (1981). Characterization and evaluation of uncertainty in probabilistic risk analysis. *Nucl. Saf.;(United States)*, 22(1).

Périé, J. N., Leclerc, H., Roux, S., and Hild, F. (2009). Digital image correlation and biaxial test on composite material for anisotropic damage law identification. *International Journal of Solids and Structures*, 46(11):2388–2396.

Peters, W. and Ranson, W. (1982). Digital imaging techniques in experimental stress analysis. *Optical engineering*, 21(3):213427–213427.

Pierron, F., Zhavoronok, S., and Grédiac, M. (2000). Identification of the through-thickness properties of thick laminated tubes using the virtual fields method. *International Journal of Solids and Structures*, 37(32):4437–4453.

Pinsky, M. and Karlin, S. (2010). *An introduction to stochastic modeling*. Academic press.

Puel, G. (2004). *Sur une théorie des méconnaissances en dynamique des structures*. PhD thesis, Cachan, Ecole normale supérieure.

Qiu, Z., Xia, Y., and Yang, J. (2007). The static displacement and the stress analysis of structures with bounded uncertainties using the vertex solution theorem. *Computer Methods in Applied Mechanics and Engineering*, 196(49):4965–4984.

Réthoré, J., Hild, F., and Roux, S. (2008). Extended digital image correlation with crack shape optimization. *International Journal for Numerical Methods in Engineering*, 73(2):248–272.

Réthoré, J., Roux, S., and Hild, F. (2009). An extended and integrated digital image correlation technique applied to the analysis of fractured samples: The equilibrium gap method as a mechanical filter. *European Journal of Computational Mechanics/Revue Européenne de Mécanique Numérique*, 18(3-4):285–306.

Saliby, E. and Pacheco, F. (2002). An empirical evaluation of sampling methods in risk analysis simulation: quasi-monte carlo, descriptive sampling, and latin hypercube sampling. In *Simulation Conference, 2002. Proceedings of the Winter*, volume 2, pages 1606–1610. IEEE.

Schmidt, U., Mergheim, J., and Steinmann, P. (2015). Identification of elastoplastic microscopic material parameters within a homogenization scheme. *International Journal for Numerical Methods in Engineering*, 104(6):391–407.

Shafer, G. (1976). *A mathematical theory of evidence*, volume 1. Princeton university press Princeton.

Sigmund, O. (1994). Materials with prescribed constitutive parameters: an inverse homogenization problem. *International Journal of Solids and Structures*, 31(17):2313–2329.

Sudret, B. and Der Kiureghian, A. (2000). *Stochastic finite element methods and reliability: a state-of-the-art report*. Department of Civil and Environmental Engineering, University of California Berkeley, CA.

Sun, K., Zhao, Y., and Hu, H. (2015). Identification of temperature-dependent thermal–structural properties via finite element model updating and selection. *Mechanical Systems and Signal Processing*, 52–53:147 – 161.

Sutton, M. A., Li, N., Garcia, D., Cornille, N., Orteu, J. J., McNeill, S. R., Schreier, H. W., and Li, X. (2006). Metrology in a scanning electron microscope: theoretical developments and experimental validation. *Measurement Science and Technology*, 17(10):2613.

Tarantola, A. (2005). *Inverse problem theory and methods for model parameter estimation*. Society for Industrial and Applied Mathematics.

Thompson, J. F., Soni, B. K., and Weatherill, N. P. (1998). *Handbook of grid generation*. CRC press.

Tikhonov, A. and Arsenin, V. (1977). *Solutions of ill-posed problems*. Scripta series in mathematics. Winston.

Tikhonov, A. N. (1995). *Numerical methods for the solution of ill-posed problems*, volume 328. Springer.

Tonon, F. (2004). Using random set theory to propagate epistemic uncertainty through a mechanical system. *Reliability Engineering & System Safety*, 85(1):169–181.

Tonon, F., Bae, H.-R., Grandhi, R. V., and Pettit, C. L. (2006). Using random set theory to calculate reliability bounds for a wing structure. *Structures and Infrastructure Engineering*, 2(3-4):191–200.

Tonon, F., Bernardini, A., and Elishakoff, I. (1999). Concept of random sets as applied to the design of structures and analysis of expert opinions for aircraft crash. *Chaos, Solitons & Fractals*, 10(11):1855–1868.

Torquato, S. (2013). *Random heterogeneous materials: microstructure and macroscopic properties*, volume 16. Springer Science & Business Media.

Toussaint, E., Grédiac, M., and Pierron, F. (2006). The virtual fields method with piecewise virtual fields. *International Journal of Mechanical Sciences*, 48(3):256–264.

Tschopp, M., Wilks, G., and Spowart, J. (2008). Multi-scale characterization of orthotropic microstructures. *Modelling and Simulation in Materials Science and Engineering*, 16(6):065009.

Vanmarcke, E. and Grigoriu, M. (1983). Stochastic finite element analysis of simple beams. *Journal of Engineering Mechanics*, 109(5):1203–1214.

Verhaeghe, W., Desmet, W., Vandepitte, D., and Moens, D. (2013). Interval fields to represent uncertainty on the output side of a static fe analysis. *Computer Methods in Applied Mechanics and Engineering*, 260:50–62.

Verhulp, E., van Rietbergen, B., and Huiskes, R. (2004). A three-dimensional digital image correlation technique for strain measurements in microstructures. *Journal of biomechanics*, 37(9):1313–1320.

Wehrle, E., Wedekind, M., and Baier, H. (2011). Fuzzy modeling of imprecise material parameters in the analysis of metal matrix composite structures. In *ASME 2011 International Mechanical Engineering Congress and Exposition*, pages 849–859. American Society of Mechanical Engineers.

Wilson, B., Cappelleri, D., Simpson, T. W., and Frecker, M. (2001). Efficient Pareto frontier exploration using surrogate approximations. *Optimization and Engineering*, 2(1):31–50.

Xia, B., Yu, D., and Liu, J. (2013). Hybrid uncertain analysis of acoustic field with interval random parameters. *Computer Methods in Applied Mechanics and Engineering*, 256:56–69.

Xia, L. and Breitkopf, P. (2015). Design of materials using topology optimization and energy-based homogenization approach in matlab. *Structural and Multidisciplinary Optimization*, 52(6):1229–1241.

Xia, Z., Zhang, Y., and Ellyin, F. (2003). A unified periodical boundary conditions for representative volume elements of composites and applications. *International Journal of Solids and Structures*, 40(8):1907–1921.

Xu, Z.-H., Li, X., Sutton, M. A., and Li, N. (2008). Drift and spatial distortion elimination in atomic force microscopy images by the digital image correlation technique. *The Journal of Strain Analysis for Engineering Design*, 43(8):729–743.

Zadeh, L. A. (1965). Fuzzy sets. *Information and control*, 8(3):338–353.

Zhang, E. (2010). *Etude de problèmes inverses en dynamique des structures par inférence bayésienne: recalage de modèle et reconstruction des efforts*. PhD thesis, Université de Technologie de Compiègne.

Zhang, E., Chazot, J., and Antoni, J. (2012). Identification parametric identification of elastic modulus of polymeric material in laminated glasses. *IFAC Proceedings Volumes*, 45(16):422 – 427.

Zhang, H. (2005). *Nondeterministic linear static finite element analysis: an interval approach*. PhD thesis, Georgia Institute of Technology.

Zhang, H. (2012). Interval importance sampling method for finite element-based structural reliability assessment under parameter uncertainties. *Structural Safety*, 38:1–10.

Zhang, H., Mullen, R. L., and Muhanna, R. L. (2010). Interval monte carlo methods for structural reliability. *Structural Safety*, 32(3):183–190.

Zhang, J. and Ellingwood, B. (1994). Orthogonal series expansions of random fields in reliability analysis. *Journal of Engineering Mechanics*, 120(12):2660–2677.

Zio, E. and Pedroni, N. (2013). *Literature review of methods for representing uncertainty*. FonCSI.

Zitzler, E., Thiele, L., Zitzler, E., Zitzler, E., Thiele, L., and Thiele, L. (1998). An evolutionary algorithm for multiobjective optimization: The strength Pareto approach. Technical report, Swiss Federal Institute of Technology, Computer Engineering and Communication Networks Lab, Zurich, Switzerland.